Study of Magnetic Fields in Nearby Spiral Galaxies

A thesis submitted to the

Tata Institute of Fundamental Research, Mumbai

for the degree of Doctor of Philosophy

(in Physics)

by

Aritra Basu

National Centre for Radio Astrophysics
Tata Institute of Fundamental Research
Pune University Campus
Pune – 411 007
India

e-mail: *aritra@ncra.tifr.res.in*

November, 2013

I would like to dedicate this thesis to my loving parents and wife ...

Contents

Acknowledgements

This thesis has been a great learning experience for me in terms of understanding the physical properties of normal galaxies and data analysis techniques. There has been enormous contributions of many people in helping me complete the thesis. I would like to acknowledge my thesis supervisor Subhashis Roy for his time and energy in introducing me to the subject of normal galaxies and interferometric data analysis using the Astronomical Image Processing Software (AIPS). I would also like to thank Dipanjan Mitra whose enthusiasm and excitement towards normal galaxies, himself being an expert pulsar astronomer, is exemplary. Countless scientific discussions on propagation of cosmic rays and magnetic fields in galaxies motivated a major portion of this thesis. His contribution towards the initial progress of this work specifically on thermal–nonthermal separation techniques and radio–FIR correlation was instrumental. This thesis would have remained incomplete without the extensive help received from Yogesh Wadadekar who introduced me to Python programming language. I would like to thank Prof. George Helou and Eric J. Murphy for extensive discussions on evolution of cosmic ray spectrum and their diffusion. I gained immensely from the discussion sessions with Prof. Kandaswamy Subramanian and Luke Chamandy regarding dynamo action in galaxies. I thank Rahul Basu for stimulating discussions regarding radio data analysis and other scientific techniques. I would take this opportunity to thank the GMRT time allocation committee (GTAC) for granting me over 100 hours of time to observe these fascinating galaxies studied in this thesis.

I would like to thank my friends at NCRA – Vishweshwar Ram Marthi, Vishal Gajjar, Arun Kumar Naidu Kalishetty, Ujjwal Kumar, Yogesh Chandola, Prasun Dutta, Narendranath Patra, Sambit Roychowdhury, Sagar Godambe, Atish Vyas, Saravanan Sengottuvel, Mayuresh Surnis, Rohit Sharma and Prakash Gaikwad who made the six long years eventful and

enjoyable. Late night discussions with Nirupam Roy has been extremely enjoyable and informative in understanding the ISM of galaxies. I would also like to thank Chandreyee Sengupta, Sanhita Joshi and Breezy Ocaña Flaquer for the late night tea/coffee and snacks. The homely food cooked by Raghunath Ghara and Kanan Dutta are culinary marvels.

This thesis extensively uses archival ∼1.4 GHz data observed with the Very Large Array (VLA). The VLA is operated by National Radio Astronomy Observatory (NRAO) which is a facility of the National Science Foundation operated under cooperative agreement by Associated Universities, Inc. We have made use of the Westerbork Synthesis Radio Telescope (WSRT) on the Web Archive. The WSRT is operated by the Netherlands Institute for Radio Astronomy ASTRON, with support of NWO. This thesis extensively used the services of NASA/IPAC Extragalactic Database (NED) for the multi-frequency ancillary data. NED is operated by the Jet Propulsion Laboratory, California Institute of Technology, under contract with the National Aeronautics and Space Administration. A considerable amount of far-infrared maps were used from publicly available database provided by the *Spitzer Space Telescope* which is operated by the Jet Propulsion Laboratory, California Institute of Technology under a contract with NASA. I thank Adam Leroy for providing the CO(J2→1) moment-0 maps of the galaxies NGC 4736, NGC 5055 and NGC 6946 observed as a part of HERACLES. I would like to thank the staff of GMRT particularly the telescope operators Rupsingh, Santaji, Nilesh, Sachin, Navnath, Shilpa, Deepak and Manisha who made the 0.33 GHz observations possible. Help from Jitendra Kodilkar and Sanjay Kudale during observations were of immense help in assuring good data quality. GMRT is run by National Centre for Radio Astrophysics of the Tata Institute of Fundamental Research.

I would thank my childhood friends in Pune – Pia Dasgupta and Anirban Bannerjee, Sangita and Debdeep Bagchi, and Sudipto Shankar Basu for their moral support and weekend escapades. Above all I would like to thank my dear wife Rimi Chatterjee for her constant motivation and moral support during tough times. I thank my parents and younger brother for their support throughout.

Declaration

This thesis is a presentation of my original research work. Wherever contributions of others are involved, every effort is made to indicate this clearly, with due reference to the literature, and acknowledgement of collaborative research and discussions.

The work was done under the guidance of Dr. Subhashis Roy, at the National Centre for Radio Astrophysics, Tata Institute of Fundamental Research, Pune.

Aritra Basu

In my capacity as supervisor of the cadidate's thesis titled: "Study of Magnetic Fields in Nearby Spiral Galaxies", I certify that the above statements are true to the best of my knowledge.

Dr. Subhashis Roy
(Thesis Supervisor)

Pune,
Date: November 29, 2013

Synopsis

The role of magnetic field and cosmic rays in determining interstellar medium (ISM) physics are amongst the least understood issues in normal star forming galaxies. Here observations lag theoretical developments. However, with the advent of high sensitivity, high resolution telescopes, like the GMRT and VLA in the radio, *Spitzer* space telescope in infrared, IRAM 30-m and BIMA, recently ALMA in millimeter and KPNO and CTIO and recently Keck and VLT in the optical, observations of normal star forming galaxies have thrown meaningful insights into understanding the galactic ISM physics.

In this thesis we investigate the variation of total magnetic field strength and its importance in determining the energetics of the ISM of normal galaxies. The magnetic field strength can be determined from synchrotron emission (also referred to as nonthermal emission) assuming energy equipartition between cosmic ray particles and magnetic field. Under this assumption, the magnetic field depends on the nonthermal spectral index[1], $\alpha_{\rm nt}$. It is therefore necessary to study the local properties of synchrotron emission through spectral index studies and effects of generation and propagation of cosmic ray electrons (CRe) giving rise to this emission. As a part of the thesis we studied the properties of synchrotron emission from normal galaxies (Basu et al., 2012). We did spatially resolved study of the radio–far infrared (FIR) correlation to validate the equipartition assumption for our sample of galaxies and understand the effects of CRe propagation (Basu, Roy & Mitra, 2012).

It is believed that the CRe giving rise to the nonthermal emission in the radio frequencies are produced in the supernova shock fronts by diffusive shock acceleration. At the acceleration sites $\alpha_{\rm nt}$ is expected to be in the range $\sim$ 0.5 to 0.7 and has been confirmed by observations of supernova

[1]Spectral index is defined as: $S_\nu \propto \nu^{-\alpha_{\rm nt}}$. Here, S_ν is the flux density at a frequency ν.

remnants. This injection spectrum of CRe is modified due to various energy loss mechanisms as they propagate away from their sources. From our study of nonthermal emission from normal galaxies, namely NGC 1097, NGC 4254, NGC 4736, NGC 5055, NGC 5236 and NGC 6946 (Basu et al., 2012), we find that in regions of high thermal fraction (regions of high star formation activity in the arms), the nonthermal spectral index has a narrow distribution peaking at $\sim$ 0.79 with a spread of 0.15, putting stringent constraints on the physical conditions for generation, diffusion and energy losses of cosmic ray electrons at scales of $\sim$ 1 kpc. $\alpha_{\rm nt}$ is generally steeper in regions with low thermal fraction (regions of low star formation activity in the interarms) and/or located in the outer parts of the galaxy and can be caused by dominant energy loss mechanisms like synchrotron and/or inverse-Compton cooling.

From our study on spatially resolved radio–FIR correlation in the normal galaxies, it is found that the slope of the radio–FIR correlation changes between arm and interarm regions at λ90 cm while remains similar at λ20 cm. In the arms the slope at λ90 cm and λ20 cm is found to be similar and is $\sim$ 0.8. In the interarms the slope is significantly flatter at λ90 cm and remains the same as in the arms at λ20 cm. In Basu, Roy & Mitra (2012), the slope of the radio–FIR correlation was used to determine the coupling between equipartition magnetic field ($B_{\rm eq}$) and gas density ($\rho_{\rm gas}$) as $B_{\rm eq} \propto \rho_{\rm gas}^{0.51\pm0.12}$. This implies equipartition of energy between magnetic field and kinetic energy of gas due to turbulent motions. Further, the change in the slope of the correlation in the interarms at λ90 cm is caused due to propagation of low energy ($\sim$ 1.5 GeV) and long lived ($\sim 10^8$ yr) CRe to farther distances from sites of production.

We studied the 'equipartition' magnetic field strength ($B_{\rm eq}$) in normal galaxies using the 'revised' equipartition formula given by Beck & Krause (2005) in Basu & Roy (2013). The mean field strength was found to be $\sim$ 11 μG. The field strength falls from the center to the edge by 40–50 percent. We argue that the estimated $B_{\rm eq}$ is close to the actual magnetic field B, through dispersion seen in the radio–FIR correlation. The energy density in the magnetic field was found to be similar to that of the total energy density (thermal + turbulent) of gas (ionized + neutral) within a

factor of $\lesssim$2 at sub-kpc scales in the arms, and thus magnetic field plays an important role in pressure balance of the interstellar medium. The energy density of magnetic field is seen to dominate over the energy density of gas in the interarm regions and outer parts of the galaxies which helps in maintaining the large scale ordered fields seen in those regions.

Organization of the thesis

In Chapter 1 we introduce the subject on normal galaxies and discuss on the major emission processes at various wavebands. We emphasize the role played by star formation activity in connecting the emission at different wavebands, like the radio–FIR correlation. We discuss several methods of estimating magnetic field in galaxies. Observationally, the magnetic field (B) can be traced by polarization studies at various wavebands, e.g., Faraday rotation and synchrotron radiation polarization in radio, polarization of starlight in optical and polarized dust emission in infrared. Zeeman splitting of spectral lines can be used to estimate the local magnetic field. Intensity of the synchrotron emission at radio wavelengths can provide estimates of B though assumptions of 'equipartition' of energy between cosmic ray particles and magnetic field. Synchrotron emission is seen from large fraction of a galaxy and under the condition of 'equipartition', it provides a measure of total magnetic field strength. At low frequencies (0.33 GHz), more than 95 percent of the emission is synchrotron in origin (Basu et al., 2012) therefore low radio frequency total intensity images can be used to determine B in galaxies. We review the previous results in the literature on probing magnetic field in normal galaxies with various techniques.

In Chapter 2 we discuss the two methods of estimating magnetic field: 1) 'classical' formula by Miley (1980) and 2) 'revised' formula by Beck & Krause (2005) and compare the magnetic field determined by both the methods. It is seen that the magnetic field determined by the 'classical' formula overestimates the field strength by factor of ~ 2 in regions of steep $\alpha_{\rm nt}$ ($\alpha_{\rm nt} > 1.2$) and underestimates in regions of flat $\alpha_{\rm nt}$ ($\alpha_{\rm nt} \lesssim 0.7$). This is caused due to fixed limits of integration of cosmic ray particles energy spectrum for determining their energy.

In this chapter we also discuss the various models proposed to explain the radio–FIR correlation. The basic model that connects these two regimes of emission is via star formation (Harwit & Pacini, 1975). Though the cause of the correlation is well understood, the tightness over several orders of magnitude still remains puzzling. Many models explaining the correlation require close coupling between the magnetic field (B) and the gas density ($\rho_{\rm gas}$) of the form, $B \propto \rho_{\rm gas}^{\kappa}$ (see e.g., Helou & Bicay, 1993; Niklas & Beck, 1997; Thompson et al., 2006). Such a coupling can be established by magnetohydrodynamic (MHD) turbulence of the ISM (see Chandrasekhar & Fermi, 1953; Cho, Lazarian & Vishniac, 2003; Cho & Vishniac, 2000; Groves et al., 2003). Numerical simulations by Cho & Vishniac (2000) revealed that $\kappa = 0.5$ is a manifestation of the equipartition condition, i.e., in steady MHD turbulence the magnetic field energy density and the energy density of the gas are about the same. The slope of the radio–FIR correlation can be used to determine κ and thereby can validate equipartition assumptions (Niklas & Beck, 1997).

The sample of galaxies observed in this thesis by the Giant Meterwave Radio Telescope (GMRT) at 0.33 GHz and data analysis procedures are discussed in Chapter 3. The galaxies observed are NGC 1097, NGC 3034, NGC 4254, NGC 4736, NGC 5055, NGC 5236 and NGC 6946. We demonstrate that these observations are sensitive to all the angular scales of interest, since the resolution of the shortest baseline in GMRT is greater than the angular size of the galaxies. Thus these observation do not suffer from missing flux density and our flux density measurements are in good agreement with the interpolated flux densities from higher and lower radio frequency observations reported in earlier studies

Radio continuum emission in galaxies originates from two main processes: thermal free–free emission from HII regions, predominantly seen in recent star formation sites and the nonthermal synchrotron emission due to acceleration of CRe in the ambient galactic magnetic field. It is thus imperative to separate the thermal emission from the total radio emission. A thorough separation of thermal emission from the total radio emission was done using the technique developed by Tabatabaei et al. (2007b). In this method, dust extinction corrected Hα emission is used as a tracer of thermal free–

free emission. We found the mean thermal fraction at 0.33 GHz to be less than 5 percent. Using archival data at about 1 GHz, we estimate the mean thermal fraction to be about 10 percent at that frequency. However, this method provides nonthermal maps at a poorer resolution determined by the resolution of *Spitzer* λ160 μm maps used to correct the Hα emission for dust absorption. The angular resolution is 40 arcsec corresponding to 1–2 kpc at the distance of the galaxies.

Alternatively, higher resolution thermal emission can be estimated from dust emission at λ24 μm (Murphy et al., 2006, 2008). All our galaxies were observed at λ24 μm using the *Spitzer* space telescope as part of *Spitzer Infrared Nearby Galaxy Survey* (SINGS; Kennicutt et al., 2003) with a resolution of 6 arcsec, better than the resolution of the radio maps. However, we note that λ24 μm emission from dust is not a direct tracer of thermal emission and is scaled to the Paschen-α (Paα) emission which is a direct tracer. The scaling of λ24-μm to obtain Paα emission is not universal and can vary between galaxies. This could give rise to systematic offsets in estimated thermal fraction determined using Hα- and λ24μm-method.. The λ24-μm emission arises not only from dust grains heated by ultra violet (UV) photons, but also from heating of diffuse cirrus clouds by the interstellar radiation field and also from old stars, mostly from the central regions. This could lead to overestimation of thermal emission in such regions. To avoid this shortcoming, and to ensure that both the methods give identical results at the resolution of the absorption corrected Hα emission (40 arcsec), we corrected the thermal fraction determined from λ24 μm to the thermal fraction from Hα. This method gives significantly better results than the use of only λ24 μm as the tracer. In this case the resolution is limited by the resolution of the radio maps, and thus allows us to probe nonthermal emission at sub-kpc scales.

We discuss in detail the techniques of separation of thermal emission in Chapter 4. We present the results on estimated $\alpha_{\rm nt}$ for each galaxy.

In Chapter 5 we discuss the results obtained on spatially resolved study of the radio–FIR correlation. We discuss our analysis to quantify the radio–FIR correlation through the parameter 'q', defined as the logarithm of the ratio of intensities at λ70μm and at radio wavelengths, i.e., q =

$\log_{10}(I_{70\mu m}/I_{\rm radio})$. We determined q within regions of $\sim$ 1 kpc for each of the galaxies. For all the galaxies combined, q at λ90 cm is seen to change by $\sim$30 percent between arm and interarm, while at λ20 cm the change is only $\sim$ 10 percent. The slope of the radio–FIR was seen to be similar for radio emission at λ90 cm and at λ20 cm in the arms of the galaxy indicating quick replenishment of CRe before they lose energy and thereby validating equipartition of energy between magnetic field and gas. Conversely, we argue that if 'equipartition' conditions are indeed valid in galaxies (as suggested by the value of κ) and the nonthermal spectral index is constrained (as seen in Basu et al., 2012), it could be presaged that the slope of the radio–FIR correlation must be independent of the radio frequency (Basu et al. 2013 under preparation). This is is in fact seen for NGC 6946 over a wide range of radio frequencies, *viz.* 0.33 GHz, 1.4 GHz and 5 GHz.

Magnetic field strength plays an important role in determining the dynamics and energetics in a galaxy. It is believed that the magnetic pressure plays a role in determining the scale height of the galactic ISM. Also, the magnetic field plays an important role in collapse of a gas cloud to help the star formation activity (Crutcher, 1999; Elmegreen, 1981). The density and distribution of cosmic rays depend on magnetic fields. It is therefore important to study the magnetic field in galaxies at local scales. In Chapter 6 we determine the equipartition magnetic field strength for normal galaxies using the 'revised' formula of Beck & Krause (2005). Here we present maps of total magnetic field using 'equipartition' assumptions for five nearby normal galaxies at sub-kpc spatial resolution. The mean magnetic field is found to be $\sim$ 11 μG. The field is strongest near the central regions where mean values are $\sim$ 20 $-$ 25 μG and falls to $\sim$ 15 μG in disk and $\sim$ 10 μG in the outer parts. There is little variation in the field strength between arm and interarm regions, such that, in the interarms, the field is $\lesssim$20 percent weaker than in the arms. There is no indication of variation in magnetic field as one moves along arm or interarm after correcting for the radial variation of magnetic field.

We study the radial scale length of various components of the ISM, like magnetic field, nonthermal emission and neutral gas. It was seen for 3 galaxies, the difference in radial scale length between λ90 cm and λ20 cm is

larger than what is expected from simple diffusion models, but consistent with streaming instability flow with Alfv́en velocity.

In Chapter 6 we argue that the estimated $B_{\rm eq}$ is close to the actual magnetic field, B. This is because at λ20 cm, the dispersion in the quantity $I_{70\mu{\rm m}}/I_{\rm nt,20cm}$ is similar to the dispersion in $B_{\rm eq}^{1+\alpha_{\rm nt}}$ for both arms and interarm regions determined at spatial scales of ~ 1 kpc. Thus at scales of ~ 1 kpc, the variations in $I_{70\mu{\rm m}}/I_{\rm nt,20cm}$, i.e., dispersion seen in the quantity 'q' of the radio–FIR correlation is caused due to variations in the magnetic field, where the magnetic field is represented by $B_{\rm eq}$. Thus, $B_{\rm eq}$ (or a constant multiple of it) is a good representative of the actual magnetic field, B.

We also studied the energy densities in gaseous and ionized phases of the interstellar medium and compared to the energy density in the magnetic field. The ratio of magnetic field energy density and total energy density (thermal + turbulent) of gas (neutral + ionized) is found to remain roughly constant as a function of galactocentric distance. They are within a factor of 2 of each other suggesting magnetic field plays an important role in determining the energy/pressure balance in the ISM. Magnetic field energy density is seen to dominate over the kinetic energy density of gas in the interarm regions and outer parts of the galaxies and thereby helps in maintaining the large scale ordered fields seen in those regions.

We summarize our results in Chapter 7.

List of Publications

1) Basu, Aritra; Mitra, Dipanjan; Wadadekar, Yogesh; Ishwara-Chandra, C. H.; 2012, MNRAS, 419, 1136
"GMRT 333 MHz observations of 6 nearby normal galaxies"

2) Basu, Aritra; Roy, Subhashis; Mitra, Dipanjan; 2012, ApJ, 756, 141
"Low Frequency Radio–FIR Correlation in Normal Galaxies at $\sim$1 kpc Scales"

3) Basu, Aritra; Roy, Subhashis; 2013, MNRAS, 433, 1675
"Magnetic fields in nearby normal galaxies: energy equipartition"

Under preparation

1) Srivastava, Shweta; Kantharia, Nimisha; Basu, Aritra; Srivastava, D. C.; Ananthakrishnan, S. A.; MNRAS, 2013
"Low radio frequency study of Wolf Rayet galaxies I: NGC 4214 and NGC 4449"

2) Basu, Aritra; Helou, George; Murphy, Eric J.; 2013, ApJ, "Smearing length scale of infrared emission"

3) Basu, Aritra; Roy, Subhashsis; 2013, MNRAS, "Multi wavelength radio–FIR correlation"

4) Basu, Aritra; "Star formation efficiency and energy equipartition"

5) Basu, Aritra; Mitra, Dipanjan; Dewangan, Gulab; 2013, MNRAS
"Grand spectrum of M51: radio to X-rays"

List of Figures

List of Tables

Chapter 1

Introduction

Magnetic field can influence motions of charged particles giving rise to scattering, radiation and self generation. Since bulk of the universe is ionized, magnetic fields play an important role in most of the astrophysical systems. It is crucial in physics of production and distribution of cosmic ray particles. It plays an important role in transferring angular momentum in protostars and thereby affects star formation activity both in terms of rate and initial mass function. Magnetic field lines carry pressure in them and are closely coupled to gas density and their dynamics that determine the scaleheight of the galactic ISM. To understand any physical process in the ISM realistically, basic information about magnetic field is necessary and are provided by observations. In majority of the studies regarding ISM in galaxies, magnetic field has been ignored for simplicity. In this thesis we investigate the variation of total magnetic field strength and its importance in determining the energetics of the ISM of normal galaxies. The magnetic field strength can be determined from synchrotron emission (also referred to as nonthermal emission) assuming energy equipartition between cosmic ray particles and magnetic field. Under this assumption, the magnetic field depends on the flux density of the nonthermal emission and its spectral index[1], $\alpha_{\rm nt}$. It is therefore necessary to study the local properties of synchrotron emission and effects of generation and propagation of cosmic ray electrons (CRes) on spectral index. As a part of the thesis, we studied the properties of synchrotron emission from normal galaxies. We did spatially resolved study of the radio–far infrared (FIR) correlation to validate the equipartition assumption for our sample of galaxies and to understand CRe propagation.

Understanding the magnetic field structure and its strength in normal galaxies has

[1]Spectral index is defined as: $S_\nu \propto \nu^{-\alpha_{\rm nt}}$. Here, S_ν is the flux density at a frequency ν.

been a topic of discussion for several decades. Magnetic fields are observed to be coherent at scales of few tens of parsec to tens of kpc and total field strength varying between few μG in interarm and outer parts of galaxies to mG in dense molecular clouds harbouring star formation. Currently it is believed that the magnetic field in galaxies originated from very weak ($\sim 10^{-20}$ G) seed field present in the inter galactic medium (IGM) perhaps generated by Biermann battery action (see e.g. Rees, 2005; Subramanian, 2008). The seed field is then amplified up to few μG due to compression and shearing during collapse to form galaxies. However, it is difficult to preserve the field over galaxy's lifetime. Large-scale dynamo action are thought to amplify the mean regular magnetic field ($B_{\rm reg}$) within galaxies and can produce large scale ($\sim$1–10 kpc) coherent field structures in $\sim 10^{8-9}$ yr (Brandenburg, 2009; Brandenburg & Dobler, 2001; Brandenburg, Sokoloff & Subramanian, 2012; Chamandy, Subramanian & Shukurov, 2013; Moss & Shukurov, 1996; Subramanian, 2008). Large-scale dynamo mechanism can give rise to appropriate spiral shapes in magnetic field structure observed in galaxies like axisymmetric and bisymmetric spirals.

Small-scale local fields ($B_{\rm turb}$) at scales $\lesssim 1$ kpc are amplified by stretching and twisting of field lines which are 'frozen' to turbulent gas motions. Small-scale turbulent dynamo can amplify field in much shorter timescales of $\sim 10^{6-7}$ yr. Note that recent numerical simulations by Bhat & Subramanian (2013) showed that small scale fluctuation dynamo can also give rise to significant large scale coherent field. Dynamos basically converts the kinetic energy of fluid motions into magnetic energy and the magnetic field strength grows by stretching until balanced by the magnetic back reaction. Under this condition the Alfvén velocity ($v_{\rm A} = B/\sqrt{4\pi\rho_{\rm gas}}$; where B is the local magnetic field strength and $\rho_{\rm gas}$ is the density of the gas) is comparable to the turbulent velocity dispersion of fluid ($v_{\rm turb}$). It is therefore expected that the field strengths are amplified up to energy 'equipartition' levels, i.e., $B^2/8\pi \approx \frac{1}{2}\rho_{\rm gas}v_{\rm turb}^2$. Further, stronger magnetic fields would result in Parker instability (Biermann et al., 2013; Machida et al., 2013; Parker, 1966; Wang, Lo & Ko, 2010) wherein buoyancy force would carry magnetic field away from the galactic disc. It is now presumed that due to magnetohydrodynamic turbulence of the ISM, the magnetic field and ISM gas density are coupled to each other as, $B \propto \rho_{\rm gas}^{\kappa}$, where, κ is the coupling index (see e.g. Chandrasekhar & Fermi, 1953; Cho, Lazarian & Vishniac, 2003; Cho & Vishniac, 2000; Groves et al., 2003; Niklas & Beck, 1997). The coupling index can assume values between 0.4–0.6 depending on the model of ISM turbulence and equilibrium conditions (Balsara & Kim, 2005; Fiedler & Mouschovias, 1993; Kim, Balsara & Mac Low, 2001;

Murgia et al., 2005; Thompson et al., 2006). Numerical simulations of Cho & Vishniac (2000) affirmed that $\kappa = 0.5$ is a manifestation of 'equipartition' conditions in galaxies. Apart from direct observations of magnetic field and gas density, the slope of the radio–FIR correlation can be used to determine κ (see Section 2.3.2.2) that can validate the assumption of equipartition in galaxies.

Under 'equipartition' conditions, since magnetic field and gas density are coupled, it is therefore expected that the radial scale lengths of magnetic field energy and gas density should be close to each other. However, in contradiction to turbulent generation of magnetic field, it is often observed that the radial scale length of magnetic field is significantly larger than that of the gas density for galaxies (Beck, 2007; Walsh et al., 2002). The magnetic field is seen to dominate in outer parts of the galaxies as compared to turbulent energy of the gas. This raises serious question on application of mean field dynamo models that amplifies field at larger scales. It was proposed that the magnetic field outside the star formation regime is perhaps amplified by dynamo driven by magneto-rotational instability (Rüdiger & Hollerbach, 2004; Sellwood & Balbus, 1999). Such a mechanism can amplify fields well beyond the energy density of turbulent motions.

We did a systematic study of the radial scale lengths of magnetic field and gas densities for six nearby normal galaxies. We also compared the energy densities of various competing forces in the ISM, like magnetic field, gas (thermal + turbulent) and thermal energy of ionised and neutral medium at sub-kpc scales depending on star formation activity. No such detailed study exists in the literature except for a few galaxies, like NGC 6946 (Beck, 2007), M33 (Tabatabaei et al., 2008) and NGC 5236 (Walsh et al., 2002) where such comparisons were done by radially averaging the quantities.

The total field strength ($B_{\rm tot}$) is given by, $B_{\rm tot} = (B^2_{\rm reg} + B^2_{\rm turb})^{1/2}$. Depending on the dominating component of the field, one expects weaker regular field in gaseous arms in galaxies where tangled fields are stronger due to turbulent gas motions, and stronger regular field in the interarm regions. This also emphasizes the importance of spatially resolved study depending on star formation activity that drives turbulence in the ISM at smallest scales by means of Supernova shocks and less energetic processes like stellar winds.

In this thesis we study the local variation of total magnetic field strength for six nearby normal galaxies at sub-kpc spatial resolution. The galaxies studied are NGC 1097, NGC 4254 (M99), NGC 4736 (M94), NGC 5055 (M63), NGC 5236 (M83) and

NGC 6946. Magnetic fields are determined using high resolution 0.33 GHz maps made using the Giant Meterwave Radio Telescope (GMRT). At 0.33 GHz, the emission arises from low energy ($\sim$ 1.5 GeV) CRes that do not suffer from significant energy losses and makes it the optimum frequency to observe normal galaxies. The radio continuum emission at this frequency is expected to be predominantly nonthermal in origin. Further, at 0.33 GHz, the GMRT is sensitive to both small-scale structures as well as large-scale diffuse emission due to its hybrid array configuration.

Total magnetic field strength requires robust estimation of the nonthermal spectral index which is obtained between 0.33 GHz and higher frequency data near 1.4 GHz. Substantial amount of thermal free–free emission could be present at that frequency and requires careful separation. A thorough separation of thermal emission is done for these galaxies at 0.33 GHz and 1.4 GHz using dust extinction corrected Hα emission as a tracer of thermal emission following the method developed by Tabatabaei et al. (2007b). The nonthermal emission using this technique is obtained at an angular resolution of 40 arcsec, limited by *Spitzer* λ160μm maps (used for dust extinction correction of Hα maps) corresponding to $\sim 1-3$ kpc at the distance of the galaxies. However, to trace magnetic field at the resolution of the radio continuum maps, $\sim 15-20$ arcsec corresponding to spatial resoltuion of $\sim 0.4-1$ kpc, we developed a new method to estimate the thermal emission by combining Hα and λ24μm as its tracer.

Previous studies on estimating spatially resolved total magnetic field strength suffered from lack of robust thermal emission separation technique (like M51, Fletcher et al. 2011; NGC 6946, Beck 2007; NGC 4254, Chyży 2008) or the galaxies studied were known starbursts (NGC 253, Heesen et al. 2009; M82, Adebahr et al. 2012) that could lead to significant mixing of magnetic field from other parts of the galaxies due to galactic fountains (see Bregman, 1980; Heald, 2012).

In this chapter we present our current understanding on magnetic field strength and structure of normal galaxies as provided by the observations and briefly describe the methods to probe magnetic field in galaxies. We also discuss the different emission mechanisms originating from normal galaxies at various wavebands and the role of star formation in them. The thesis is organised in the following way: in Chapter 2, we present the background of 'equipartition' magnetic field estimates and various models explaining the radio–FIR correlation. We define our sample and data analysis procedure in Chapter 3. Here we present the total intensity 0.33 GHz continuum maps of the galaxies. In Chapter 4, we present the techniques of separating thermal emission from the total radio emission and present the results on nonthermal spectral index variation.

In Chapter 5, we present spatially resolved radio–FIR correlation and used the slope of well known radio–FIR correlation to validate the 'equipartition' assumption within galaxies at local scales. In Chapter 6, we present the total 'equipartition' magnetic field strength maps and argue using the dispersion seen in the radio–FIR correlation that our estimated values of equipartition magnetic field represents the actual magnetic field well. Further, we compare the energy densities of magnetic field with different competing phases of the ISM. We conclude our results in Chapter 7.

1.1 Study of magnetic fields in galaxies

The field strength determined from mean synchrotron emission surface brightness of nearby galaxies typically lies in the range $5-15$ μG with a mean total magnetic field strength of 9 ± 1 μG (Niklas, 1995). For the Milky Way the magnetic field was found to fall by ~ 50 percent from the centre, where the field strength is ~ 10 μG, to the edge with field strength being ~ 5 μG (Beck et al., 1996). Even dwarf galaxies can have similar field strengths if the star formation rates are high. Giant spiral galaxy like M31 which has relatively low star formation rate is seen to have a mean total field strength of ~ 6 μG. Grand design spirals like NGC 5194 (M51), NGC 5236 (M83) and NGC 6946 have stronger field strength of $\sim$10–15 μG. Significantly strong total field strength with $\langle B_{\rm tot}\rangle \sim 20-30$ μG was found for M51 in the gaseous arms (Fletcher et al., 2011). Interaction of galaxies could lead to field compression giving rise to strong fields up to ~ 30 μG, like NGC 4038 and NGC 4039 (Chyży & Beck, 2004). Strongest field has been observed for the starburst galaxy NGC 3034 (M82) where the total magnetic field strength was estimated to be ~ 80 μG in the centre and $\sim 20-30$ μG in the synchrotron halo (Adebahr et al., 2012). In barred galaxies like NGC 1097, NGC 1365 and NGC 5236 the field strength could be amplified by compression due to bar shock. In NGC 1097 the field was found to be stronger in the bars with $\langle B_{\rm tot}\rangle \sim 25-30$ μG (Beck et al., 2005).

A host of high radio frequency (>1 GHz) polarization studies of nearby galaxies have been done to uncover the magnetic field structure in external galaxies. They have produced interesting results in support of the dynamo action. High radio frequency (above 1 GHz) Faraday rotation measure (RM) observations reveal the presence of both regular (coherent) and random magnetic fields in galaxies. Regular magnetic field is found to have different azimuthal symmetries predicted by dynamo models,

viz., axisymmetric spiral as seen in the galaxy IC 342 (Krause, Hummel & Beck, 1989), bisymmetric spiral seen in the galaxy M81 (Krause, Beck & Hummel, 1989), or combination of axisymmetric and bisymmetric in M33 (Tabatabaei et al., 2008) and axisymmetric and quadri-symmetric in NGC 6946 (Beck, 2007). The regular field as observed by polarized emission is seen to follow the gaseous spiral structure in many galaxies like M51, M81 and M83 (Fletcher et al., 2011; Krause, Beck & Hummel, 1989; Krause, Hummel & Beck, 1989; Neininger, 1992; Neininger et al., 1991). Spiral structure in magnetic field has also been observed in galaxies without any prominent spiral arms like the ringed galaxy NGC 4736 (Chyży & Buta, 2008). Regular magnetic field with spiral pattern are also seen in flocculent galaxies like M33 (Buczilowski & Beck, 1991; Tabatabaei et al., 2008), NGC 5055 (Knapik et al., 2000) and NGC 4414 (Soida et al., 2002). Such spiral patterns are believed to be generated due to mean field dynamo action and can form without the assistance of density waves. However, for grand design spirals with strong density waves like M51, M83 and NGC 2997, enhanced regular fields are observed by Faraday rotation at the inner edges of the inner optical arms (Fletcher et al., 2011; Han et al., 1999). This is perhaps generated by compression and shear of non-axisymmetric gas flow due to density wave potential.

In barred galaxy like NGC 1097, the magnetic field vectors are seen to be aligned with gas streamlines suggesting that the regular field is aligned with shearing flow (Beck et al., 1999, 2005). For NGC 1365, similar magnetic field structures were observed except for weaker shear due to the bar (Beck et al., 2005).

Although, the regular magnetic field is seen to have spiral patterns, the regions of strongest regular field is offset from the gaseous spiral arms and can be seen beyond the optical extent of the galaxies. The regular field in the interarm regions is seen to have high degree of polarization (∼30–60 percent) as compared to arm regions (∼5–30 percent). Figure 1.1 shows the polarized intensity of the galaxy NGC 6946 at 5 GHz by combining data from the VLA and Effelsberg. The grayscale shows the Hα emission. Only 1–5 percent of the emission is polarized in the inner spiral arms and increases to $\gtrsim$ 50 percent in the interarm regions (Beck, 2007; Beck & Hoernes, 1996). Strong polarized emission is seen in the interarm regions of the galaxy M83 (Beck, 2005). The degree of polarization was seen to be as high as $\sim$ 60 percent in the outer parts as compared to the inner parts where the degree of polarization is only $\sim$ 10 percent (Neininger et al., 1993). In the ringed galaxy NGC 4736, the degree of polarization was observed to be lower ($\sim$ 10 percent) in the star forming ring than its vicinity ($\sim$ 15 percent) and rises to $\sim$ 40 percent in the outer parts (Chyży & Buta,

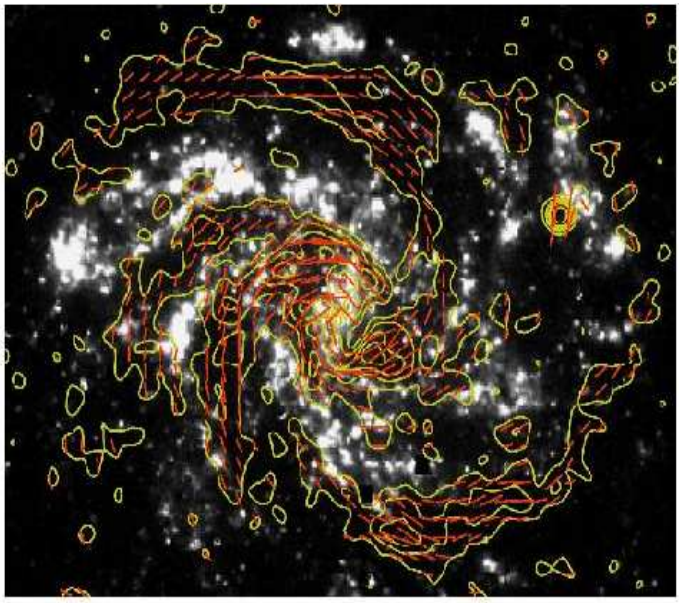

Figure 1.1: The contours show the polarized intensity at 5 GHz for the galaxy NGC 6946 made using data from the VLA and Effelsberg telescope. The grayscale image shows the Hα intensity of the galaxy. *Image courtesy: Rainer Beck* (Beck, 2007).

2008). In M51, emission was found to be $\sim$ 25 percent polarized in arms while in the interarm regions it was $\sim$40 percent (Fletcher et al., 2011). Strong regular field has been observed towards the outer parts of the galaxy NGC 5055 (Knapik et al., 2000). It is now abundantly clear that weaker polarized emission in the gaseous spiral arms is dominated by turbulent magnetic field caused by increased turbulence of gas clouds. In such regions the magnetic field and turbulent gas are expected to remain in energy equipartition. However, in the case of NGC 6946 the enhancement in the degree of polarization seen in the northern and southern interarm regions, referred to as 'magnetic arms' in Beck (2007), is surprising. They are symmetric, almost 100 percent aligned and do not fill the entire interarm regions with a thickness of $\sim$ 1 kpc. High sensitivity observation revealed their extension beyond the optical disc of the galaxy especially in the northern region (Beck, 2007). Such a contrast in degree of polarization between arm and interarm is not due to increased turbulent fields in arms alone and perhaps produced by dynamo action. It is proposed that they are superposition of axisymmetric and quadri-symmetric dynamo modes by Beck (2007). Recently, Chamandy, Subramanian & Shukurov (2013) put forward numerical simulations suggesting finite time dynamo relaxation can cause the magnetic arms to lag the gas/star-forming arms

of the galaxy and gives rise to the magnetic arms.

1.2 Measuring magnetic field

Magnetic field in galaxies can mainly be probed by four techniques, namely, 1) polarization of star light in optical and infrared, 2) Faraday rotation and depolarization in the radio, 3) Zeeman effect and 4) synchrotron emission in the radio. We discuss in short the methods and their limitations.

1.2.1 Polarization of starlight

Rotating elongated dust grains can be aligned by radiative torque (Hoang & Lazarian, 2008) or by field lines (Davis & Greenstein, 1951) perpendicular to the major axis. This results is different extinction properties when observed along major or minor axis of the dust grains and leads to polarization in optical and infrared bands. Thus, polarization observations in optical and/or infrared wavelengths can give estimates of magnetic field parallel to the plane of the galaxy.

However, to estimate the magnetic field using this technique, requires detailed understanding of the magnetic properties of the dust grains and the physics of their alignment. Further, it depends on a number of model dependent parameters like local gas and grain temperatures, space density of grains and the gas density and geometry of the dust grains.

1.2.2 Faraday rotation

Propagation of linearly polarized radio waves from background source through magneto-ionic medium causes rotation of plane of polarization due to Faraday rotation. It can give estimates of the regular field parallel to the line-of-sight ($B_\parallel$). The rotation angle (ϕ) when observed at radio wavelength λ is given by,

$$\phi = k\lambda^2 \int n_\mathrm{e} B_\parallel dl \tag{1.1}$$

where, k is a constant, n_e is the thermal electron density and the integral is over the line-of-sight. The observable quantity, rotation measure (RM) defined as, RM $= \Delta\phi/\Delta\lambda^2 \propto \int n_\mathrm{e} B_\parallel dl$ is used to determine the magnetic field component along the

line-of-sight. It is difficult to unambiguously determine $B_{\parallel}$ from rotation measure as both $B_{\parallel}$ and $n_{\rm e}$ can change along the line-of-sight. This requires a detailed model of $n_{\rm e}$ which is often difficult to obtain for external galaxies. Polarized radio emission may not be observed from a large fraction of the galaxies due to Faraday and/or beam depolarization (Sokoloff et al., 1998).

1.2.3 Zeeman effect

In the presence of magnetic fields, the atomic energy levels can be split into larger number of energy levels. Thus, a line frequency at ν_0 is splitted into two components of circular polarization due to magnetic field along a line-of-sight, and the shifted frequencies are given by,

$$\nu_{\pm} = \nu_0 \pm \frac{eB_{\parallel}}{4\pi mc} \tag{1.2}$$

Here, $\nu_{\pm}$ are the line centers for two circular polarizations, e is the electron charge, m is the mass of electron and c is speed of light. Zeeman splitting can directly measure $B_{\parallel}$, but it it requires a strong, localized magnetic field and detection of such lines in external galaxies is extremely difficult.

1.2.4 Synchrotron emission

Relativistic electrons accelerated in galactic magnetic field gives rise to synchrotron emission at radio frequencies and is given by,

$$I_{{\rm syn},\nu} \propto N(E) B_{\perp}^{1+\alpha_{\rm nt}} \tag{1.3}$$

Here, $I_{{\rm syn},\nu}$ is the synchrotron intensity at radio frequency ν, $N(E)$ is the number density of relativistic electrons per energy interval and $B_{\perp}$ is the magnetic field strength perpendicular to the line-of-sight. Synchrotron emission is seen from a large fraction of a galaxy and can be used to estimate the total magnetic field strength. However, this requires knowledge of $N(E)$ which is not known. One uses the assumption of 'equipartition' of energy between cosmic ray particles and magnetic field to estimate the total magnetic field strength, i.e., the energy density of magnetic field and relativistic particles are same.

We used this method to determine the magnetic field strength in six nearby normal galaxies. Note that the emission in radio is not entirely synchrotron in origin and

is contaminated by thermal free–free emission. Estimation of magnetic field strength maps from nonthermal emission and its spectral index requires careful separation of the thermal component from the total radio emission.

1.3 Emission in galaxies and star formation activity

Emission from normal galaxies originates along the entire electromagnetic spectrum; from radio to gamma rays through infrared, optical and ultraviolet. The emission in each of the wavebands arises from a wide variety of astrophysical processes and thus traces different components of the ISM. In the radio, the continuum emission originates from two main processes: thermal free–free emission from HII regions, predominantly seen at recent star formation sites and the nonthermal synchrotron emission due to acceleration of cosmic ray electrons (CRes) in the ambient galactic magnetic field. In the infrared bands, the emission originates due to re-radiation by dust heated by ultraviolet (UV) photons from stars. The broad band optical emission originates from different class of stars, like old stars ($> 10^8$ yr) in R- and V-band, and young stars ($\sim 10^5 - 10^7$ yr) in the B-band. The ultraviolet emission essentially arises from UV photons produced by the stellar population of the ISM and thereby traces star formation rate in galaxies. In X-ray band, the emission can be thermal in origin, i.e., from gas heated up to 10^4 to 10^6 K, or nonthermal in nature due to inverse-Compton scattering of low energy CRes ($\sim 1 - 10$ GeV) with the cosmic microwave background photons. Also, high energy cosmic ray particles ($\sim$ 100 GeV) gives rise to synchrotron emission in the X-ray band. The gamma ray emission arises from ultra high energy cosmic ray particles ($\gtrsim$ 1 TeV) and ionization of molecules present in dense clouds of the ISM by low energy cosmic ray particles.

Although the emission in different waveband arises from a wide variety of processes, they are connected by star formation activity. The CRes giving rise to the nonthermal radio emission is believed to be accelerated in the shock fronts of supernova remnants of massive ($\gtrsim 8$ $M_\odot$), short lived ($\lesssim 3 \times 10^7$ yr) stars. The same population of star ionizes the HII regions giving rise to free–free emission. They also produce UV photons that heats up the dust to give emission in the far- and near-infrared. In the optical and UV bands, stars are directly responsible for the emission. Massive stars and/or their explosion can heat the ISM gas up to $10^4 - 10^6$ K giving rise to thermal emission in the X-ray band. Dense molecular clouds, which harbours star formation, can be

ionized by heavy cosmic ray particles like protons, to produce charged (π^+ or π^-) or uncharged (π^0) pions. π^0 can decay to produce gamma-ray emission. Since, star formation is directly or indirectly responsible for emission in various wavebands, it therefore gives rise to some of the fascinating correlations seen in normal galaxies, like the radio–FIR correlation (see e.g. Condon, 1992; Helou, Soifer & Rowan-Robinson, 1985; Yun, Reddy & Condon, 2001, and the references therein), radio–CO and CO–FIR correlation (Murgia et al., 2005), radio–gamma ray correlation (Schöneberg, Becker Tjus & Schuppan, 2012) or the correlations between far- or near-infrared emission and emission from optical spectral lines like Hα and Paschen-α (Paα) (Calzetti et al., 2005). It is therefore imperative to study the property of normal galaxies based on star formation activity. We have broadly classified our study between arm and interarm regions, i.e., regions of high and low star formation activity respectively.

1.3.1 Nonthermal radio emission from galaxies

It is believed that the CRes giving rise to the nonthermal emission in the radio frequencies are produced and accelerated in the supernova shock fronts by diffusive shock acceleration. This gives rise to a power law in cosmic ray particle (electrons + heavier particles) energy (E) distribution of the form, $n(E)dE \propto E^{-\gamma}dE$. Here, $n(E)$ is the number density of cosmic ray particles of energy E per energy interval dE and γ is the energy spectral index. The energy spectral index γ, for CRes is related to the nonthermal spectral index ($\alpha_{\rm nt}$) as $\gamma = 2\alpha_{\rm nt} + 1$ and can be measured directly from observations. At the acceleration site one expects $\alpha_{\rm nt} \sim 0.5$ to 0.7 (Bell, 1978; Biermann & Strom, 1993; Bogdan & Völk, 1983). Observations of Galactic supernova remnants confirm the injection $\alpha_{\rm nt}$ to be ~ 0.5 (Green, 2009; Kothes et al., 2006). The CRes then propagate away from the sites of generation to the ISM filling up the disk of the galaxies, and consequently losing energy by several mechanisms and $\alpha_{\rm nt}$ changes with time. They can undergo ionization loss, where the spectral index gets flatter, i.e, $\Delta\alpha_{\rm nt} = -0.5$. CRes can lose energy due to bremsstrahlung or adiabatic cooling, which do not affect $\alpha_{\rm nt}$. However, CRes predominantly lose energy by synchrotron and/or inverse-Compton cooling that steepens $\alpha_{\rm nt}$ such that $\Delta\alpha_{\rm nt} = +0.5$ (see Longair, 2011).

As mentioned earlier, there could be significant contribution due to the presence of thermal free–free emission in radio wavelengths, and thus $\alpha_{\rm nt}$ is contaminated, making the measured value flatter than the true value. This is because, the thermal emission has a spectral index of 0.1. Owing to significantly steeper ($\alpha_{\rm nt} \gtrsim 0.5$) spectral index

of the nonthermal emission, it is likely to exceed the thermal emission by far at low radio frequencies ($\lesssim$ 1 GHz), except perhaps in the innermost and giant HII regions where active star-formation could lead to high thermal emission. Thermal emission is known to correlate almost linearly with the far infrared emission and thus can bias the slope of the correlation. It will be shown in Chapter 2 that the slope of the radio–FIR correlation can help us determine the coupling index between magnetic field and gas density which is used to validate the 'equipartition' assumption. This makes separation of thermal emission important. Further the study of radio–FIR correlation can throw insights into the effects of propagation and evolution of CRe energy spectrum. This is because the radio–FIR correlation holds good if the same emitting region produces both radio and FIR emission. However, due to the differences in the scale-lengths of dust heating UV photons ($\sim$ 100 pc) and CRes at 0.33 GHz and 1.4 GHz ($\sim$ 1 and $\sim$ 2 kpc respectively) the form of the correlation is expected to change.

To measure the spectral indices of nonthermal emission, at sites of generation of CRes and how their propagation affects the spectrum, we observed 11 nearby normal galaxies, namely NGC 0628, NGC 1097, NGC 3034, NGC 3621, NGC 4254, NGC 4736, NGC 5033, NGC 5055, NGC 5236, NGC 6946 and NGC 7793 using the Giant Meterwave Radio Telescope (GMRT) at 0.33 GHz (λ90 cm). However, due to poor data quality (NGC 0628), non-detection of diffuse emission (NGC 5033) and non-availability of complimentary datasets (NGC 3034, NGC 3621 and NGC 7793), we have used data on the six galaxies, NGC 1097, NGC 4254, NGC 4736, NGC 5055, NGC 5236 and NGC 6946 in this thesis. We used archival data/images at higher radio frequencies, near 1.4 GHz (λ20 cm) to determine the spectral index after a thorough separation of the thermal emission at both the frequencies. We have done spatially resolved study for these six nearby normal galaxies to probe various ISM properties at spatial scales of 0.4–2 kpc, depending on the distance of the galaxies.

Chapter 2

Background

In this chapter we discuss on the mathematical details of the 'equipartition' magnetic field strengths and radio–FIR correlation.

2.1 Equipartition fields

Synchrotron emission from galaxies arises due to acceleration of cosmic ray electrons (CRes) in the galactic magnetic field. However, synchrotron emissivity depends on number density of CRes as well as magnetic field strength. Therefore, synchrotron emissivity alone cannot be unambiguously used to determine the field strength. The magnetic field can be determined using synchrotron flux density by assuming energy equipartition between magnetic field and cosmic ray particles first proposed by Burbidge (1956). In this method the magnetic field is estimated by minimizing the total energy in magnetic field and cosmic ray particles (electrons + protons), i.e, $U_{\rm tot} = U_{\rm mag} + U_{\rm CRe} + U_{\rm CRp}$, where $U_{\rm mag} = B^2_{\rm eq}/8\pi$ is the magnetic field energy density, $U_{\rm CRe}$ is the energy density of CRes obtained from synchrotron flux density and $U_{\rm CRp} = \kappa U_{\rm CRe}$ is the energy density of heavier relativistic particles. Here, κ is the ratio of energy of heavier relativistic particles to relativistic electrons.

2.1.1 Classical formula

The total energy in CRes can be computed by integrating over the entire synchrotron emission spectrum assuming a power law distribution of relativistic electrons with energy, i.e, $N(E) = N_0 E^{-\gamma} dE$. Thus, the total energy between $E_{\rm min}$ and $E_{\rm max}$ is given

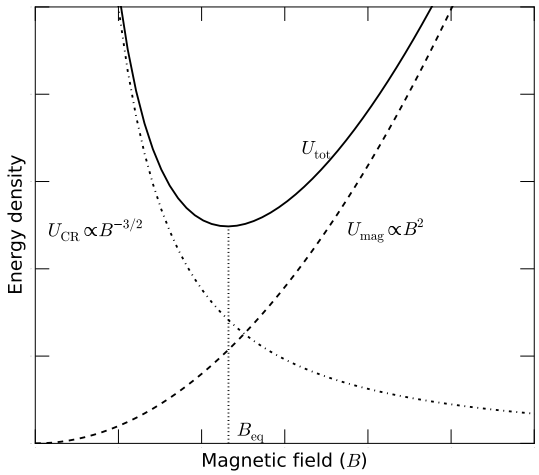

Figure 2.1: Equipartition magnetic fields

by,

$$U_{\rm CRe} = N_0 V \int_{E_{\rm min}}^{E_{\rm max}} EN(E)dE = N_0 V \int_{E_{\rm min}}^{E_{\rm max}} E^{1-\gamma} dE \tag{2.1}$$

Here, V is the volume occupied by CRes. The limits $E_{\rm min}$ and $E_{\rm max}$ are determined by synchrotron cutoff frequencies. The lower cutoff frequency corresponding to $E_{\rm min}$ is determined such that the electrons would become nonrelativistic and will not give rise to synchrotron emission. On the other hand, at upper cutoff frequency corresponding to $E_{\rm max}$, the number density of such particles would be low owing to their steep energy index ($\gamma \approx 2.6$). At such energies the lifetime of the particles would be few times 10^5 yr. Synchrotron luminosity is given by,

$$L_{\rm syn} = V \int_{E_{\rm min}}^{E_{\rm max}} -\frac{dE}{dt} N(E)dE \propto (B \sin\theta)^2 V N_0 \int_{E_{\rm min}}^{E_{\rm max}} E^{2-\gamma} dE \tag{2.2}$$

Here, $-dE/dt$ is the synchrotron power emitted by a single CRe and it can be shown $-dE/dt \propto (B \sin\theta)^2 E^2$, where θ is the angle between magnetic field direction and line-of-sight. Eliminating VN_0 from Equations 2.1 and 2.2, and integrating, we get,

$$U_{\rm CRes} = cL_{\rm syn} B^{-3/2} \tag{2.3}$$

where, c is the proportionality constant depending on $E_{\rm min}$, $E_{\rm max}$ and γ. Now, $U_{\rm CRp} = \kappa U_{\rm CRes}$, thus,

$$U_{\rm tot} = c(1+\kappa)L_{\rm syn}B^{-3/2} + \phi V\frac{B^2}{8\pi} \tag{2.4}$$

Here, ϕ is the source filling factor of the magnetic field. Minimising $U_{\rm tot}$, i.e., $dU_{\rm tot}/dB|_{B=B_{\rm eq}} = 0$ and; putting in all the constants and replacing the synchrotron luminosity by flux density, the equipartition magnetic field is given by Equation 10 in Miley (1980),

$$B_{\rm eq} = 5.69\times10^{-5}\left[(1+\kappa)\frac{1}{\theta_{\rm maj}\theta_{\rm min}\phi}\frac{I_{\rm syn}\nu_0^{\alpha_{\rm nt}}}{l}\frac{\nu_{\rm max}^{1/2-\alpha_{\rm nt}}-\nu_{\rm max}^{1/2-\alpha_{\rm nt}}}{1/2-\alpha_{\rm nt}}\right]^{2/7} \text{ Gauss} \tag{2.5}$$

Here, $I_{\rm syn}$ is the synchrotron flux density (in Jy beam^{-1}) at frequency ν_0 (in GHz). $\theta_{\rm maj}$ and $\theta_{\rm min}$ are the size of the emitting region in arcsec. $\nu_{\rm max}$ and $\nu_{\rm min}$ (in GHz) are the synchrotron cutoff frequencies determined from the limits of integration in Equation 2.2, where, $\nu = 16.1(B\sin\theta)E^2$. The cutoff frequencies are assumed to be $\nu_{\rm min} \sim 0.1$ GHz and $\nu_{\rm max} \sim 100$ GHz.

2.1.2 Revised formula

Beck & Krause (2005) pointed out that the limits of integration ($\nu_{\rm max}$ and $\nu_{\rm min}$) in deriving the classical formula to estimate the magnetic field strength depends on B. This was ignored while minimizing the total energy of magnetic field and cosmic ray particles. Therefore, the classical formula (Equation 2.5) is incorrect. This leads to a constant exponent of 2/7 as given in Equation 2.5. They derived the 'revised' equipartition formula assuming the ratio of number density of relativistic electrons and heavier particles like protons (K_0) to be a constant. Also, the total numbers of protons and electrons that are accelerated are same and are generated with the same power law energy spectrum.

As per cosmic ray particle acceleration models, the energy spectrum of cosmic rays is a power law with a break at the rest mass energy of the particle, i.e, $E_{\rm br} = m_{\rm rest}c^2$. Here, $E_{\rm br}$ is the break energy, $m_{\rm rest}$ is the rest mass of the particle being accelerated and c is the velocity of light (see e.g., Bell, 1978). Thus, the number of cosmic ray

particles per unit volume, $n(E)$, per unit energy interval, dE, is given by,

$$n(E)dE = \begin{cases} n_0 \left(\frac{E_{\rm br}}{E_0}\right)^{(1-\gamma_0)/2} \left(\frac{E}{E_{\rm br}}\right)^{-(\gamma_0+1)/2} dE, & {\rm E_{min}} < E < E_{\rm br} \quad (2.6) \\ n_0 \left(\frac{E}{E_0}\right)^{-\gamma_0} dE, & {\rm E} > {\rm E_{br}} \quad (2.7) \end{cases}$$

Here, γ_0 is the injection energy spectral index of the cosmic ray particles and n_0 is the particle number density at energy E_0. Following Beck & Krause (2005) total number of particles (N) can be obtained by integrating Equations 2.6 and 2.7 over the energy spectrum,

$$N = \int_{E_{\rm min}}^{\infty} n(E)dE = \int_{E_{\rm min}}^{E_{\rm br}} n_0 \left(\frac{E_{\rm br}}{E_0}\right)^{\frac{(1-\gamma_0)}{2}} \left(\frac{E}{E_{\rm br}}\right)^{-\frac{(\gamma_0+1)}{2}} dE + \int_{E_{\rm br}}^{\infty} n_0 \left(\frac{E}{E_0}\right)^{\gamma_0} dE$$

Thus,

$$N \approx \frac{2n_0E_0}{\gamma_0 - 1} \left(\frac{E_0^2}{E_{\rm br}E_{\rm min}}\right)^{\frac{(\gamma_0-1)}{2}} \quad \text{for} \quad E_{\rm min} \ll E_{\rm br}. \quad (2.8)$$

Since, it was assumed that same number of electrons and protons are accelerated to relativistic energies above threshold energy $E_{\rm min}$, from Equation 2.8, the ratio of number density of electrons-to-protons (K_0) is given by,

$$K_0 = n_{0,{\rm p}}/n_{0,e} = (E_{\rm p}/E_{\rm e})^{(\gamma_0-1)/2} \quad (2.9)$$

Similarly, the total energy density of cosmic ray particles, assuming negligible energy loss is given by,

$$E_{\rm CR} = \int_{E_{\rm min}}^{\infty} n(E)EdE = \int_{E_{\rm min}}^{E_{\rm br}} n_0 \left(\frac{E_{\rm br}}{E_0}\right)^{\frac{(1-\gamma_0)}{2}} \left(\frac{E}{E_{\rm br}}\right)^{\frac{-(\gamma_0+1)}{2}} EdE + \int_{E_{\rm br}}^{\infty} n_0 \left(\frac{E}{E_0}\right)^{\gamma_0} EdE \quad (2.10)$$

Now, for $E_{\rm min} \ll E_{\rm br}$ and $2 < \gamma_0 < 3$, from Equation 2.10 we get,

$$E_{\rm CR} = n_0E_0^2 \left(\frac{E_0}{E_{\rm br}}\right)^{\gamma_0-2} \left(\frac{2}{3-\gamma_0} + \frac{1}{\gamma_0 - 2}\right) \quad (2.11)$$

2.1.3 Total energy of cosmic ray particles

Cosmic ray particles can suffer ionization and/or Coulomb losses that tend to flatten the energy spectral index (see e.g. Longair, 2011). For heavier particles, like protons, if the energy is less than their rest mass energy, i.e, $E_{\rm p} < 938.3$ MeV, then the energy spectrum is roughly independent of the energy and thus the number density per unit energy interval can be written as,

$$n(E)dE \simeq n_{0,\rm p}\left(\frac{E_{\rm p}}{E_0}\right)^{-\gamma_{\rm p}} dE, \quad \text{for} \quad E \lesssim E_{\rm p} \tag{2.12}$$

Here, $n_{0,\rm p}$ is the number density of relativistic protons at energy E_0 and $\gamma_{\rm p}$ is the energy spectral index.

On the other hand, for highly relativistic protons the flat energy spectra gradually steepens and assumes a power law index which can be represented by,

$$n(E)dE = n_{0,\rm p}\left(\frac{E}{E_0}\right)^{-\gamma_{\rm p}} dE, \quad \text{for} \quad E > E_{\rm p} \tag{2.13}$$

To compute the total energy density of cosmic ray protons ($U_{\rm CR,p}$), following Beck & Krause (2005), the gradual steepening of the energy spectra can be approximated by a break at energy $E_{\rm p}$. Thus, in the weak shock regime, i.e., $\gamma_{\rm p} > 2$,

$$\begin{aligned} U_{\rm CR,p} &= \int_{E_{\rm min}}^{\infty} n(E)EdE \\ &= \int_{E_{\rm min}}^{E_{\rm p}} n_{0,\rm p}E\left(\frac{E_{\rm p}}{E_0}\right)^{-\gamma_{\rm p}} dE + \int_{E_{\rm p}}^{\infty} n_{0,\rm p}E\left(\frac{E}{E_0}\right)^{-\gamma_{\rm p}} dE \\ &\approx n_{0,\rm p}E_0^2\left(\frac{E_0}{E_{\rm p}}\right)^{2-\gamma_{\rm p}}\left[\frac{1}{2}+\frac{1}{\gamma_{\rm p}-2}\right], \quad \text{for} \quad E_{\rm min} \ll E_{\rm p} \end{aligned} \tag{2.14}$$

In Equation 2.14, $n_{0,\rm p}$ can be replaced by $K_0 n_{0,\rm e}$ (see Equation 2.9), where $n_{0,\rm e}$ is the number density of cosmic ray electrons that can be obtained from the intensity of synchrotron emission (I_ν) as,

$$n_{0,\rm e} = \frac{I_\nu\left[\nu/2c_1\right]^{(\gamma_{\rm e}-1)}/2}{c_2(\gamma_{\rm e})E_0^{\gamma_{\rm e}} l B_\perp^{(\gamma_{\rm e}+1)/2}} \tag{2.15}$$

In principle the ratio of proton-to-electron number density is a function of energy, i.e., $K = K(E)$. However, in the case of negligible energy loss, i.e., $E_{\rm p} < E < E_{\rm syn}$,

K can be assumed to be a constant, K_0. Here, $E_{\rm syn}$ is the energy of electrons above which synchrotron and inverse-Compton losses are dominant. Within this energy range, the energy spectral index for electrons and protons are the same, $\gamma_{\rm p} = \gamma_{\rm e} = \gamma$. Using Equations 2.15 and 2.9 in Equation 2.14, along with the energy of cosmic ray electrons, the total energy density of cosmic ray particles ($U_{\rm CR}$) is given by,

$$U_{\rm CR} = \gamma(K_0+1)\frac{I_\nu \left[\nu/2c_1\right]^{(\gamma-1)/2} E_{\rm p}^{(2-\gamma)}}{2(\gamma-1)c_2(\gamma) l B_\perp^{(\gamma+1)/2}} \tag{2.16}$$

The component of the magnetic field in the plane of sky, $B_\perp$ can be written in terms of the total magnetic field, B as, $B_\perp = B\cos i$ where, i is the inclination angle with respect to the plane of sky such that 0° is face-on.

Under the assumption of 'equipartition' of energy between cosmic ray particles and magnetic field, $U_{\rm CR} = U_{\rm mag} = B_{\rm eq}^2/8\pi$, from Equation 2.16 we get,

$$B_{\rm eq} = \left[4\pi(2\alpha_{\rm nt}+1)(K_0+1)\frac{I_\nu(\nu/2c_1)^{\alpha_{\rm nt}}}{(2\alpha_{\rm nt}-1)c_2(\alpha_{\rm nt})l c_4(i)}\right]^{\frac{1}{\alpha_{\rm nt}+3}} \tag{2.17}$$

Here, $c_4(i) = [\cos i]^{(\gamma+1)/2}$.

Beck & Krause (2005) pointed out that the magnetic field determined using the 'classical' formula (Equation 2.5) underestimates the field strength in regions of comparatively flatter spectral index, $\alpha_{\rm nt} \sim 0.5-0.6$, and overestimates in regions of steeper $\alpha_{\rm nt}$. Figure 2.2 shows the variation of the ratio of magnetic field estimated using the two 'equipartition' formulae, i.e., $B_{\rm eq,classical}/B_{\rm eq,revised}$ as a function of $B_{\rm eq,revised}$. Here, $B_{\rm eq,classical}$ and $B_{\rm eq,revised}$ are the magnetic field strength estimated using the classical formula of Miley (1980) and revised formula of Beck & Krause (2005), respectively for different values of the nonthermal spectral index ($\alpha_{\rm nt}$). Clearly in the regions were $\alpha_{\rm nt}$ is flatter (< 0.7), the magnetic field is underestimated using the classical formula. This is caused due to fixed upper frequency cutoff $\nu_{\rm max} = 100$ GHz, where a significant contribution from higher energy electrons are not considered. Similarly, in the regions of steep spectral index, i.e., $\alpha_{\rm nt} > 0.7$, the classical magnetic field estimates are too high as the lower limit of cutoff frequency, $\nu_{\rm min} = 10$ MHz, corresponds to particle energies of 250 MeV for ~ 10 μG field. This is below the lower break energy $E_{\rm p} = 938$ MeV. Thus, in this case the total cosmic ray energies are overestimated.

As the nonthermal spectral index steepens as a function of galactocentric radius (r), the magnetic field estimated using the classical formula is seen to remain constant

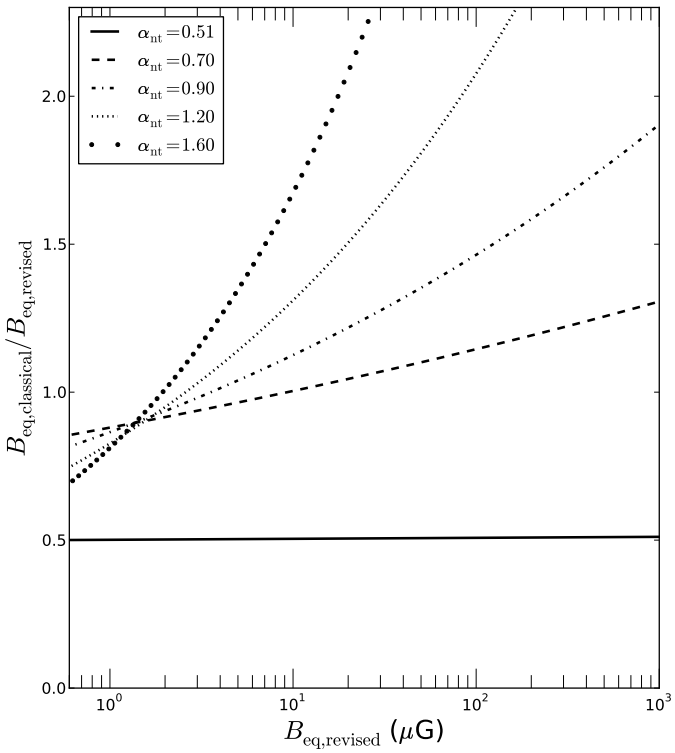

Figure 2.2: Variation of the ratio of equipartition magnetic field determined by the classical formula ($B_{\rm eq,classical}$) and revised formula ($B_{\rm eq,revised}$) as a function of $B_{\rm eq,revised}$ for different values of nonthermal spectral index ($\alpha_{\rm nt}$).

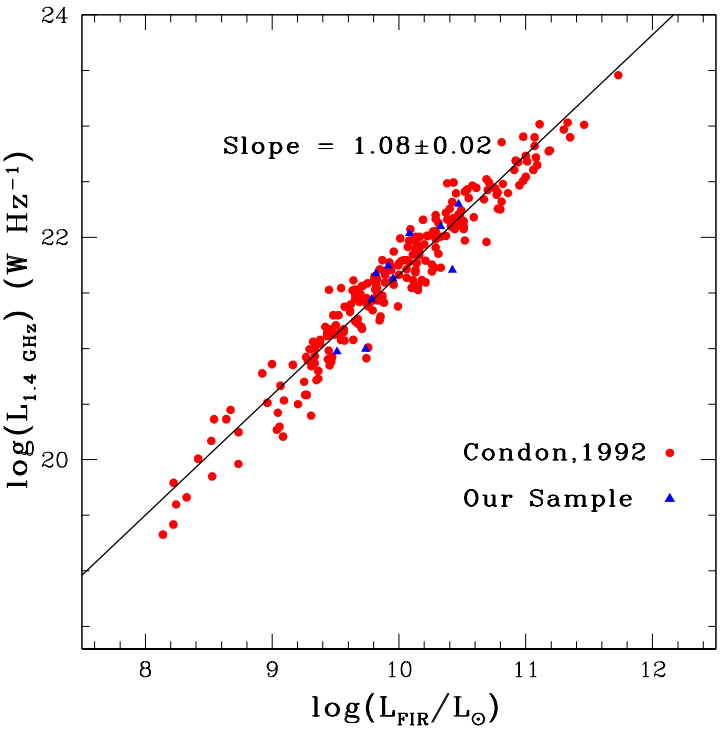

Figure 2.3: The luminosity at 1.4 GHz vs. the FIR luminosity in units of solar luminosity. The red points are taken from Condon (1992) and the blue points are the galaxies observed using the GMRT.

or increasing as a function of r. In this thesis we have therefore used the 'revised' equipartition formula to estimate the magnetic field strengths.

2.2 Radio–FIR correlation

The radio–FIR correlation is one of the tightest and universal correlation known in astrophysics, wherein the luminosities of the radio and far-infrared wavebands are seen to be highly correlated. This was first observed in the center of starforming galaxies (van der Kruit, 1971) and later extended to disk of galaxies (van der Kruit, 1973). The true universality of this correlation was established after the *IRAS* mission for a large number of galaxies. The correlation is seen to span over 5 orders of magnitude in luminosity in both radio and infrared wavelengths and has a dispersion less than factor of 2. Figure 2.3 shows the radio–FIR correlation between the 1.4 GHz radio continuum luminosity and FIR luminosity (see below). The red points are taken from Condon

(1992) and the blue triangles are the sample galaxies observed using the GMRT by us.

In normal galaxies, dust re-radiates majority of its flux between $\lambda 40$ μm and $\lambda 120$ μm. This is measured by the quantity FIR computed using *IRAS* flux densities at $\lambda 60$ μm and $\lambda 100$ μm ($S_{60\mu\mathrm{m}}$ and $S_{100\mu\mathrm{m}}$ respectively; Helou et al., 1988), such that,

$$\frac{FIR}{\mathrm{W\ m^{-2}}} = 1.26 \times 10^{-14} \left(\frac{2.58 S_{60\mu\mathrm{m}} + S_{100\mu\mathrm{m}}}{\mathrm{Jy}} \right) \tag{2.18}$$

To quantify the tightness of the correlation, Helou, Soifer & Rowan-Robinson (1985) introduced the parameter 'q_{FIR}', which is the logarithmic ratio of total far-infrared and radio flux densities, defined as,

$$q_{FIR} = \log \left[\frac{FIR(\mathrm{W\ m^{-2}})}{3.75 \times 10^{12}\ S_\nu(\mathrm{W\ m^{-2} Hz^{-1}})} \right] \tag{2.19}$$

Typically, $\nu \sim 1.4$ GHz for which q_{FIR} is seen to have a rms scatter $\lesssim 0.2$ around a mean value of 2.3. However, the quantity FIR is seen to correlate with a wide range of radio frequencies like, 0.15 GHz (Cox et al., 1988), 1.4 GHz (Condon, 1992), 5 GHz and 10 GHz (Price & Duric, 1992) on global scales for a wide morphological class of galaxies like spirals, irregulars and dwarfs (Dressel, 1988; Price & Duric, 1992; Wunderlich, Wielebinski & Klein, 1987). The correlation is seen to hold good even for monochromatic far-infrared luminosities of galaxies at $\lambda 10$ μm (van der Kruit, 1971, 1973), $\lambda 60$ μm (Yun, Reddy & Condon, 2001) and $\lambda 70$ μm (Appleton et al., 2004). In such cases, the quantity q can be defined as,

$$q = \log \left[\frac{S_{\mathrm{IR}}(\mathrm{Jy})}{S_{\mathrm{radio}}(\mathrm{Jy})} \right] \tag{2.20}$$

where, S_{IR} and S_{radio} are the flux densities at far-infrared and radio wavelengths respectively. Murphy et al. (2006) pointed out that the use of monochromatic far-infrared luminosity does not affect the correlation except for a slight increase in the dispersion.

The slope of the radio–FIR (b; such that $S_{\mathrm{radio}} \propto S_{\mathrm{IR}}^b$) is an useful parameter to understand the relation between magnetic field strength and gas density. In the initial years of discovery of the correlation, the slope was thought to be unity for global studies of the correlation for a wide range of radio frequencies from 0.151 GHz to 10.7 GHz. A simple model of direct and linear relationships between star formation, FIR emission and CRes production was put forward. However, it was soon evident that the slope is nonlinear at lower radio frequencies ($\lesssim 5$ GHz) that demanded more sophisticated

models to explain the correlation. At 10.7 GHz for a sample of 74 galaxies the slope was found to be 1.02 ± 0.03 (Rengarajan & Iyengar, 1990). The slope was found to be 0.99±0.38 at 4.75 GHz for a sample of 99 galaxies (Wunderlich, Wielebinski & Klein, 1987). At 1.49 GHz, Condon, Anderson & Helou (1991) found a slope of 1.11±0.02 for a sample of 258 galaxies. At 0.408 GHz for a sample of 120 galaxies Rengarajan & Iyengar (1990) found a slope of 1.02±0.06 and at 0.151 for 65 galaxies the slope is found to be 1.16±0.04 (Fitt, Alexander & Cox, 1988). Price & Duric (1992) reported the slope between nonthermal radio emission at 5 GHz and total FIR emission to be 1.33.

In spatially resolved studies, the radio–FIR correlation is seen to hold at scales of few tens of parsecs to tens of kiloparsecs (see e.g., Beck & Golla, 1988; Dumas et al., 2011; Hoernes, Berkhuijsen & Xu, 1998; Hughes et al., 2006; Murgia et al., 2005; Paladino et al., 2006; Paladino, Murgia & Orrú, 2009; Tabatabaei et al., 2007a; Xu et al., 1992). Such studies clearly exhibits a non-linear relationship between the two emissions at local scales depending on the property of ISM. Decomposition of the FIR emission into warm and cool dust ($\sim$ 30 K and $\sim$ 19 K respectively) components showed the thermal component of the radio emission to be strongly correlated with the warm dust emission for the galaxy M31 with a slope of unity (Hoernes, Berkhuijsen & Xu, 1998). This is because both the emission directly arises from massive (> 20 $M_\odot$) ionizing stars. Such strong correlation between thermal radio emission and warm dust was seen for M33 (Tabatabaei et al., 2007a), NGC 6946 (Frick et al., 2001; Tabatabaei et al., 2013) and LMC (Hughes et al., 2006).

On the other hand the cool (cirrus) dust emission arises from dust heated by the interstellar radiation field (ISRF) and is seen to be correlated with the nonthermal component of radio emission. This correlation is physically more interesting and gives rise to non-linear slope. For M31, slope of the nonthermal radio emission and cool dust emission at $\sim$ 19 K was found to be 0.8 ± 0.09 (Hoernes, Berkhuijsen & Xu, 1998). Paladino et al. (2006) found a mean slope of 0.7 ± 0.1 between radio continuum emission at λ20 cm and FIR emission at λ24 μm for a sample of six galaxies at spatial scales of 0.12–0.4 kpc. For NGC 6946, using synchrotron emission at λ20 cm and FIR data from *Herschel* space telescope at λ70, λ100, λ160 and λ250 μm, Tabatabaei et al. (2013) found slopes of 0.65, 0.67, 0.84 and 0.96 respectively. Dumas et al. (2011) found the slope of the radio–FIR correlation to vary between central, arm, interarm and outer regions for the galaxy M51 at scales of $\sim$ 0.25 kpc. The slope is found to be comparatively flatter in the central disk and arms ($b \sim 0.67$ and ~ 1 respectively),

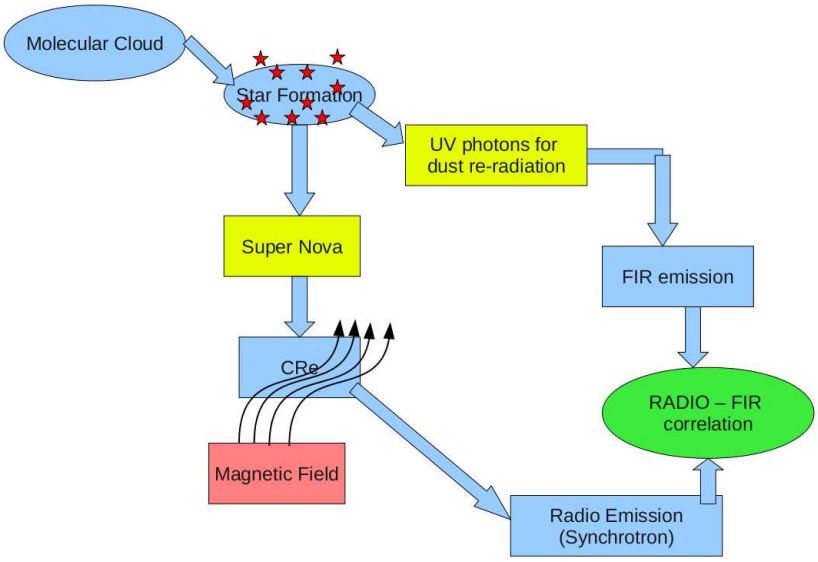

Figure 2.4: Basic model for the radio–FIR correlation.

while in the interarm and outer disk the slope steepens to $b \sim 2$.

2.3 Models of radio–FIR correlation

Several models has been put forward to understand the universality and tightness of the radio–FIR correlation. Star formation is thought to be the origin of this correlation (Harwit & Pacini, 1975), wherein the far infrared emission arises from re-radiation by dust heated by UV photons from massive (~ 10 $M_\odot$) stars. On the other hand the radio emission arises due to nonthermal emission from CRes produced in supernova remnants of these massive, short lived ($\lesssim 10^6$ yr) stars. Figure 2.3 pictorially shows the connections giving rise to the radio–FIR correlation. However, the tightness of the radio–FIR correlation remains puzzling due to several independent physical parameters that are responsible for the emission, viz., magnetic field, production and acceleration of CRes, star formation rate, production of UV photons and absorption and re-radiation by dust. Several models have been proposed explaining the tightness of the correlation. We discuss in brief some of the models given by Völk (1989), Helou & Bicay (1993) and Niklas & Beck (1997).

2.3.1 Calorimeter model: Völk (1989)

In one of the first attempts to explain the radio–FIR correlation, Völk (1989) presented a calorimeter model wherein the ratio of radio emission and dust emission is constant as both are proportional to the supernova rate. In this model, all systems are assumed to be optically thick, i.e., relativistic electrons giving rise to radio emission are completely trapped within the host galaxy and all the UV radiation is absorbed by dust (Murgia et al., 2005). In this scenario, synchrotron and inverse-Compton losses occur within the host galaxy and thus each galaxy acts as a calorimeter.

The synchrotron loss $(dE/dt)_{\rm syn}$ is given by,

$$\left(\frac{dE}{dt}\right)_{\rm syn} = \frac{4}{3}\sigma_{\rm T} c \left(\frac{v}{c}\right)^2 \gamma^2 U_{\rm mag} \tag{2.21}$$

Here, $\sigma_{\rm T}$ is the Thompson cross-section, c is the velocity of light, v is the velocity of the relativistic electrons, γ is the Lorentz factor and $U_{\rm mag}$ is the magnetic field energy density. Similarly, the inverse-Compton loss rate $(dE/dt)_{\rm IC}$ is given by,

$$\left(\frac{dE}{dt}\right)_{\rm IC} = \frac{4}{3}\sigma_{\rm T} c \left(\frac{v}{c}\right)^2 \gamma^2 U_{\rm rad} \tag{2.22}$$

Here, $U_{\rm rad}$ is the radiation field energy density.

If the galaxy acts as a calorimeter, the ratio of total synchrotron loss to total energy loss, i.e, $(dE/dt)_{\rm syn}/[(dE/dt)_{\rm syn} + (dE/dt))_{\rm IC}]$ is given by, $(1 + U_{\rm rad}/U_{\rm mag})^{-1}$. Völk (1989) argued that this factor must be nearly constant to maintain the observed radio–FIR correlation. They estimated, $1 + U_{\rm rad}/U_{\rm mag}$ to be in the range 3–4 for our Galaxy and M82 which lies in the radio–FIR correlation line.

This model explains the radio–FIR correlation at global scales, however the assumption that the electrons loose all their energy within the galaxy would give rise to steep nonthermal spectral index, i.e., $\alpha_{\rm nt} \geq 1$. Lisenfeld, Völk & Xu (1996) put forward a non-calorimeter model which allows a finite escape probability of the synchrotron emitting relativistic electrons. In this case $\alpha_{\rm nt}$ is predicted to be $\sim 0.9 - 1$. However, Niklas, Klein & Wielebinski (1997) found only one-third of the galaxies from a sample of 74 galaxies have such steep $\alpha_{\rm nt}$. This indicates that most of the galaxies are not electron calorimeters. Further, this model faces difficultly in explaining the spatially resolved radio–FIR correlation seen within the galaxies.

2.3.2 Non-calorimeter models

To explain the radio–FIR correlation, non-calorimeter models has been proposed by Helou & Bicay (1993) and Niklas & Beck (1997). We discuss both the models in brief.

2.3.2.1 Model of Helou & Bicay (1993)

Helou & Bicay (1993) put forward a non-calorimeter model to explain the radio–FIR correlation taking into account diffusion, radiative decay and escape of CRes giving rise to synchrotron emission in the radio. Further, they explore both optically thin and thick regime of dust heating UV photons. It is assumed that dust heating UV photons and CRes are generated in constant proportion through star formation; and magnetic field (B) and gas density ($\rho_{\rm gas}$) are locally coupled as $B \propto \rho_{\rm gas}^{\kappa}$. In this model, Helou & Bicay (1993) explains the constant value of q_{FIR} seen for the galaxies or correspondingly the constancy of Q defined as $Q = L_{\rm FIR}/L_{\rm syn}$, where $L_{\rm FIR}$ and $L_{\rm syn}$ are the total infrared and synchrotron luminosities respectively.

Following Helou & Bicay (1993), for dust heating luminosity of $L_{\rm heat}$, $L_{\rm FIR}$ can be written as, $L_{\rm FIR} = L_{\rm heat}(1-e^{-\tau})$, where τ is the optical thickness of dust to the heating radiation. On the other hand, the synchrotron luminosity for a CRes luminosity $L_{\rm CRes}$ is given by, $L_{\rm syn} = \eta L_{\rm CRes} t_x (1+t_x)^{-1}$ where η is the fraction of total energy lost by CRes as synchrotron emission and $t_x = t_{\rm esc}/t_{\rm syn}$ is the ratio of escape timescale of CRes ($t_{\rm esc}$) to synchrotron loss timescale ($t_{\rm syn}$). Now, the parameter Q can be written as,

$$Q = \frac{L_{\rm FIR}}{L_{\rm syn}} = \left[\frac{L_{\rm heat}}{L_{\rm CRes}}\right]\left[\frac{(1-e^{-\tau})}{t_x(1+t_x)^{-1}}\right] \approx \text{constant} \tag{2.23}$$

In order to maintain a constant value of Q, the factors $L_{\rm heat}/L_{\rm CRes}$ and $(1-e^{-\tau})/[t_x(1+t_x)^{-1}]$ must be individually constant. The condition $L_{\rm heat}/L_{\rm CRes}$ = constant is the manifestation of the fact that both dust heating UV photons and synchrotron emitting CRes have a common source of origin through star formation. Helou & Bicay (1993) argue that such a condition can be met without severely constraining the energetic of stars or their initial mass functions.

Helou & Bicay (1993) showed that the factor $(1-e^{-\tau})/[t_x(1+t_x)^{-1}]$ depends weakly on τ and is constant when $t_x = \tau$ for entire viable range of τ. This condition is physically less apparent and can be understood if magnetic field and gas density are coupled as $B \propto \rho_{\rm gas}^{0.5}$. This is because, t_x scales as B^2 and the optical depth τ scales as the gas density $\rho_{\rm gas}$.

This model successfully explains the correlation at global scales and implies that the nonthermal spectral index to be correlated with the magnetic field strength. Such a correlation was absent for a sample of 74 galaxies (Niklas & Beck, 1997). Furthermore, the local radio–FIR correlation seen in galaxies cannot be explained by this model.

2.3.2.2 Model of Niklas & Beck (1997)

In another non-calorimeter model, Niklas & Beck (1997) explained the observed slope of the radio–FIR correlation. In this model, the nonthermal radio emission is constrained by assuming a coupling between magnetic field and gas density of the form $B \propto \rho_{\rm gas}^{\kappa}$ and energy equipartition between cosmic ray particles and magnetic field. On the other hand, the FIR emission is constrained through the Kennicutt–Schmidt (KS) law ($\rho_{\rm SFR} \propto \rho_{\rm gas}^{n}$, where $n = 1.4 \pm 0.15$; Kennicutt, 1998). Here, $\rho_{\rm SFR}$ is the star formation rate volume density. Further, $\rho_{\rm SFR}$ is directly proportional to the number density of dust heating UV photons and thus by extension the FIR luminosity. This formalism explains the radio–FIR correlation at global as well as local scales, except perhaps at scales of few hundred parsecs where the equipartition assumption may not hold good. Also, diffusion of CRes away from their sources of generation could affect the form of the correlation.

Based on this formalism and its assumptions, Dumas et al. (2011) studied the environmental dependencies of the slope b of the radio–FIR correlation with other ISM coupling indices like KS-law index (n), magnetic field and gas density coupling index (κ) and nonthermal spectal index ($\alpha_{\rm nt}$). The nonthermal emission ($S_{\nu,{\rm nt}}$) at radio frequency ν assuming energy equipartion between magnetic field and cosmic ray particles is given by (see Equation 2.17),

$$S_{\nu,{\rm nt}} \propto B_{\rm eq}^{3+\alpha_{\rm nt}} \tag{2.24}$$

Here, $B_{\rm eq}$ is the total equipartition magnetic field strength. The magnetic field is assumed to be coupled to $\rho_{\rm gas}$. Thus from Equation 2.24,

$$S_{\nu,{\rm nt}} \propto \rho_{\rm gas}^{\kappa(3+\alpha_{\rm nt})} \tag{2.25}$$

The infrared emission is also be connected to $\rho_{\rm gas}$. For optically thick dust to UV photons, the entire UV emission is re-radiated by dust and thereby traces star formation. Under this condition the intensity of dust heating UV photons ($I_{\rm UV}$) is

directly proportional to infrared intensity ($S_{\rm IR}$), i.e., $S_{\rm IR} \propto I_{\rm UV} \propto \rho_{\rm SFR}$. From KS-law it follows,

$$S_{\rm IR} \propto \rho_{\rm gas}^{n} \tag{2.26}$$

Similarly, for optically thin dust, the infrared intensity is related to UV intensity as, $S_{\rm IR} \propto \tau I_{\rm UV} \propto \tau \rho_{\rm gas}^{n}$. Here, τ is the optical depth and is proportional to dust density ($\rho_{\rm dust}$). For a constant gas-to-dust ratio, ($\rho_{\rm dust} \propto \rho_{\rm gas}$; Xu & Helou, 1996),

$$S_{\rm IR} \propto \rho_{\rm gas}^{1+n} \tag{2.27}$$

Moreover, in low density regions, the dust can be heated by the interstellar radiation field (ISRF) also known as 'cirrus' emission. In this case,

$$S_{\rm IR} \propto \rho_{\rm dust} \propto \rho_{\rm gas} \tag{2.28}$$

For a radio–FIR correlation slope of b (i.e, $S_{\nu,\rm nt} \propto S_{\rm IR}^{b}$) evaluating the exponent of $\rho_{\rm gas}$ in Equation 2.25 with Equations 2.26, 2.27 and 2.28 we get,

$$b = \begin{cases} \dfrac{\kappa(3+\alpha_{\rm nt})}{n}, & \text{optically thick dust} \quad (2.29) \\ \dfrac{\kappa(3+\alpha_{\rm nt})}{n+1}, & \text{optically thin dust} \quad (2.30) \\ \kappa(3+\alpha_{\rm nt}), & \text{cirrus emission} \quad (2.31) \end{cases}$$

This model explains the radio–FIR correlation at all scales and can be used to determine the coupling index (κ) between magnetic field and gas density. It turns out that the absolute value of κ can specify if equipartition conditions are valid within galaxies (see Chapter 1). In our study, we use this prescription to validate equipartition assumptions that is used to estimate the magnetic field strength.

Chapter 3

Sample Selection and Observations

In this Chapter we report 0.33 GHz interferometric observation of seven nearby galaxies, NGC 1097, NGC 3034, NGC 4254, NGC 4736, NGC 5055, NGC 5236 and NGC 6946, using the Giant Meterwave Radio Telescope (GMRT).

3.1 Galaxy sample

Angular extent and flux density are the two main criteria used to select the sample galaxies for our study. Large angular size ($\gtrsim$ 5 arcmin) would allow enough synthesized beams across the galaxies to discern arm and interarm regions for spatially resolved study. We note that an interferometer can detect a source without losing flux density, if its angular extent is smaller that the resolution of the shortest baseline which for the GMRT corresponds to $\sim$ 18 arcmin at 0.33 GHz. To reliably detect low surface brightness diffuse emission across the galaxies at 0.33 GHz, the integrated continuum flux density of the galaxies must be more than 200 mJy at 1.4 GHz. Using the GMRT with 32 MHz band-width at 0.33 GHz one can achieve a rms noise of $\sim$ 200 μJy beam^{-1} (assuming a synthesized beam of $\sim$15 arcsec) in a full synthesis run. Thus, for 3σ detection of uniform diffuse emission from a source of size $\sim 7 \times 7$ arcmin^2, the integrated flux density should be $\sim$ 450 mJy. Assuming a spectral index of $\sim$ 0.7 for normal galaxies, the integrated flux density at 1.4 GHz must be $\sim$ 170 mJy and hence the flux density criteria.

Based on the above two criteria, the sample was chosen from the Spitzer Infrared Nearby Galaxy Survey (SINGS; Kennicutt et al., 2003) to compliment the study of nonthermal emission from normal spiral galaxies with other publicly available data.

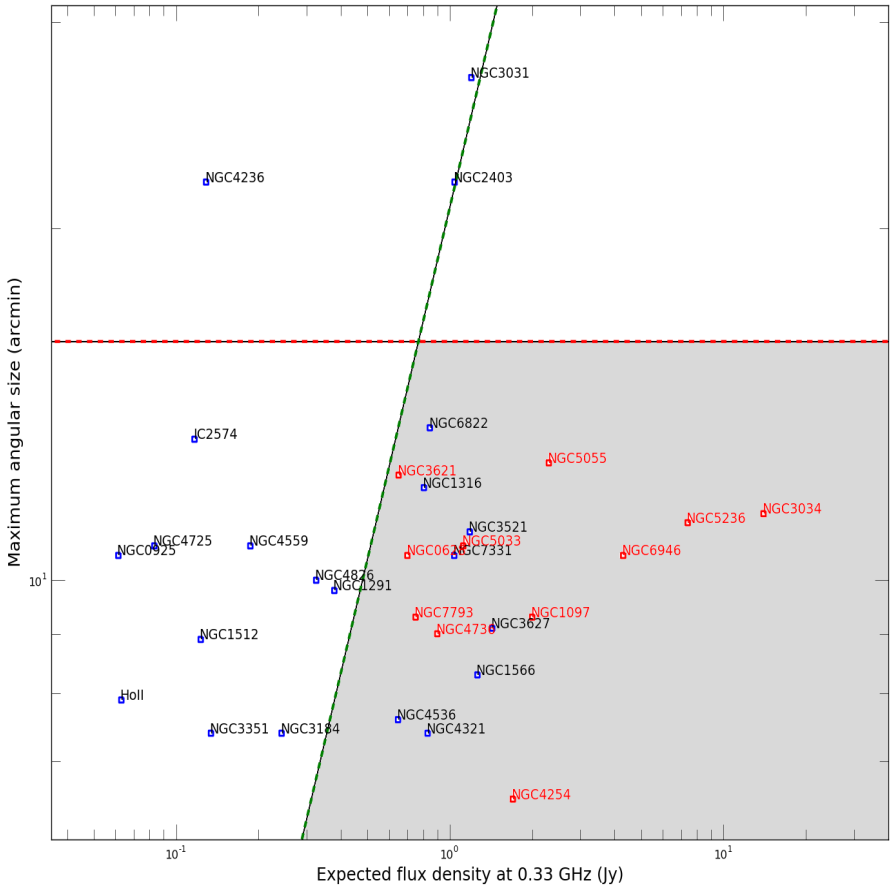

Figure 3.1: The plot shows the expected flux density at 0.33 GHz and the maximum angular size of the galaxies from SINGS sample. The red dashed line is the maximum detectable angular size using the GMRT at 0.33 GHz. The green dashed line is the 3σ surface brightness threshold ($\sim$ 600 μJy beam^{-1}). All the galaxies in the shaded region are expected to be detected by the GMRT. The galaxies marked in red are the galaxies observed for this thesis.

Figure 3.1 shows the expected integrated flux at 0.33 GHz for the SINGS sample galaxies and the maximum angular size of the galaxies. The red dashed line marks the maximum angular size that can be detected by the GMRT at 0.33 GHz. The green dashed line shows the angular size with integrated flux density for detecting the sources with surface brightness of 600 μJy beam^{-1}. Thus, all the galaxies in the shaded regions can be detected by the GMRT at 0.33 GHz.

Our sample (see Table 3.1, also shown in red in Figure 3.1) includes seven nearby spiral galaxies, with clearly demarcated arm and interarm regions as seen both in the optical and radio continuum. The galaxies are NGC 1097, NGC 3034, NGC 4254, NGC 4736, NGC 5055, NGC 5236 and NGC 6946. The optical size of these galaxies are typically 6–12 arcmin and the GMRT synthesized beam (typically $\sim$ 15 arcsec) at 0.33 GHz can resolve the arm interarm regions. All the galaxies have 1.4-GHz integrated continuum flux density greater than 200 mJy (as measured in NRAO VLA[1] Sky Survey (NVSS) data; Condon et al. 1998), which is necessary to ensure detection of low surface brightness diffuse emission across the galaxy. A wealth of high quality, publicly available, multi waveband data are present for these galaxies to study various properties of the ISM, like HI and CO to trace neutral gas, Hα to trace thermal bremsstrahlung emission and thermal electron density, far infrared to trace cold dust ($\sim$ 20 K) responsible for absorption of Hα emission, etc (see Table 3.1). To study the spectral index variations across the galaxies, we used a higher radio frequency, near 1.4 GHz, archival continuum interferometric data/maps (discussed in Chapter 4). In Table 3.1 we summarise the salient features of the galaxies and the source of obtaining the archival data. These datasets are useful to do further analysis. We present the optical DSS images of the sample galaxies in Figure 3.2. All the images are of angular size 12×12 arcmin^2. In all, eleven galaxies have been observed using the GMRT at 0.33 GHz, however, due to non-availability of complimentary data for the galaxies NGC 0628, NGC 3621, NGC 5033 and NGC 7793, we have used data from seven galaxies in this chapter. We present a short description of these seven galaxies.

NGC 0628 (M74) is a face-on (i = 24°) grand design spiral galaxy with two clear arms in the optical driven by density waves. The 1.36 GHz radio continuum emission from the spiral arms can be seen clearly at high surface brightness. However, surprisingly, the radio continuum emission is depleted towards the centre unlike the bright optical emission (Braun et al., 2007). This galaxy has been studied at 0.327

[1]The Very Large Array (VLA) is operated by the NRAO. The NRAO is a facility of the National Science Foundation operated under cooperative agreement by Associated Universities, Inc.

Table 3.1: The sample galaxies observed with the GMRT at 0.33 GHz.

Name	RA	Dec	Morphological type	Angular size (D_{25})(arcmin^2)	i (°)	Distance (Mpc)	Spatial resolution (pc arcsec^{-1})	Other Available data¶	
(1)	(2)	(3)	(4)	(5)	(6)	(7)	(8)	(9)	
NGC 0628$^{\oplus}$ (M74)	01h36m41.7s	+15d47′01″	SAsc	10.5×9.5	24	9.0†	43.6	λ20cm	–
								λ24, 70, 160μm	SINGS[5]
								CO	HERACLES[6]
								HI	THINGS[7]
								Hα	1.5m CTIO
NGC 1097	02h46m19.0s	−30d16′30″	SBbc	9.3×6.3	45	14.5†	70.3	λ20cm	VLA CD array[4]
								λ24, 70, 160μm	SINGS
								CO	HERACLES
								HI	THINGS
								Hα	1.5m CTIO
NGC 3034* (M82)	09h55m52.7s	+69d40′46″	IO	11.2×4.3	75	3.97†	21	λ20cm	VLA D array
								Hα	2.1m KPNO
NGC 3621$^{\oplus}$	11h18m16.5s	−32d48′51″	SAsd	12.3×7.1	65	6.76†	33	λ20cm	–
								λ24, 70, 160μm	SINGS
								CO	–
								HI	THINGS
								Hα	4m CTIO
NGC 4254 (M99)	12h18m49.6s	+14d24′59″	SAsc	6.2×5.1	34	15.43†	74.8	λ20cm	VLA C array[8]
								λ24, 70, 160μm	SINGS
								CO	HERACLES
								HI	VIVA[14]
								Hα	2.1m KPNO
NGC 4736 (M94)	12h50m53.0s	+41d07′14″	SAab	11.2×9.1	41	4.66[1]	22.3	λ20cm	Westerbork SINGS[9]
								λ24, 70, 160μm	SINGS
								CO	HERACLES
								HI	THINGS
								Hα	1m JKT[10]

In column (5) D_{25} refers to the optical diameter measured at the 25 magnitude arcsec^{-2} contour from de Vaucouleurs et al. (1991). Column (6) gives the inclination angle (i) defined such that 0° is face-on. Distances in column (7) are taken from: [1] Karachentsev et al. (2003) and the NED [†]. Column (9) lists available ancillary data that have been used in this paper. [¶] The wavelengths represents the waveband in which other data were available/used (see Section 3.1 for exact frequencies). [*] Thermal-nonthermal emission separation was not done for this galaxy (see text for details). [⊕] The GMRT data for these galaxies are not presented in this thesis due to non-availability of complimentary data. [4]VLA archival data using CD array configuration (project code: 237), Spitzer infrared nearby galaxy survey [5](Kennicutt et al., 2003), [6]HERA CO-line extragalactic survey (Leroy et al., 2009), [7]The HI nearby galaxy survey (Walter et al., 2008), [8]VLA archival data using C array configuration (project code: AU007), [9]Braun et al. (2007), [10]Knapen et al. (2004), [14]VLA Imaging of Virgo Spirals in Atomic Gas (VIVA; Chung et al., 2009).

Table 3.1: Continued

Name	RA	Dec	Morphological type	Angular size (D_{25})(arcmin^2)	i (°)	Distance (Mpc)	Spatial resolution (pc arcsec^{-1})	Other Available data¶	
(1)	(2)	(3)	(4)	(5)	(6)	(7)	(8)	(9)	
NGC 5033$^{\oplus}$	13h13m27.4s	+36d35′38″	SAsc	10.7×5.0	68	19.5†	94.5	λ20cm	–
								λ24, 70, 160μm	SINGS
								CO	–
								HI	–
								Hα	2.1m KPNO
NGC 5055 (M63)	13h15m49.3s	+42d01′45″	SAbc	12.6×7.2	59	9.2†	44.6	λ18cm	Westerbork SINGS
								λ24, 70, 160μm	SINGS
								CO	HERACLES
								HI	THINGS
								Hα	2.3m KPNO
NGC 5236 (M83)	13h37m00.9s	−29d51′56″	SABc	11.2×11	24	4.51[2]	22	λ20cm	VLA CD array[11]
								λ24, 70, 160μm	SINGS
								CO	NRAO 12m[12]
								HI	THINGS
								Hα	0.9m CTIO
NGC 6946	20h34m52.3s	+60d09′14″	SABcd	11.5×9.8	33	6.8[3]	33	λ20cm	VLA C+D array[13]
								λ24, 70, 160μm	SINGS
								CO	HERACLES
								HI	THINGS
								Hα	2m KPNO
NGC 7793$^{\oplus}$	23h57m49.8s	−32d35′49.8″	SAsd	9.3×6.3		4.2†	20.4	λ20cm	–
								λ24, 70, 160μm	SINGS
								CO	–
								HI	THINGS
								Hα	1.5m CTIO

Distances in column (7) are taken from: [2] Karachentsev et al. (2002), [3] Karachentsev, Sharina & Huchtmeier (2000). Column (9) lists available ancillary data that have been used in this paper. $^{\oplus}$ The GMRT data for these galaxies are not presented in this thesis due to non-availability of complimentary data. ¶ The wavelengths represents the waveband in which other data were available/used (see Section 3.1 for exact frequencies). [11]VLA archival data using CD array configuration (project code: AS325), [12]Crosthwaite et al. (2002), [13]VLA archival map combining data from C and D array (Beck, 2007).

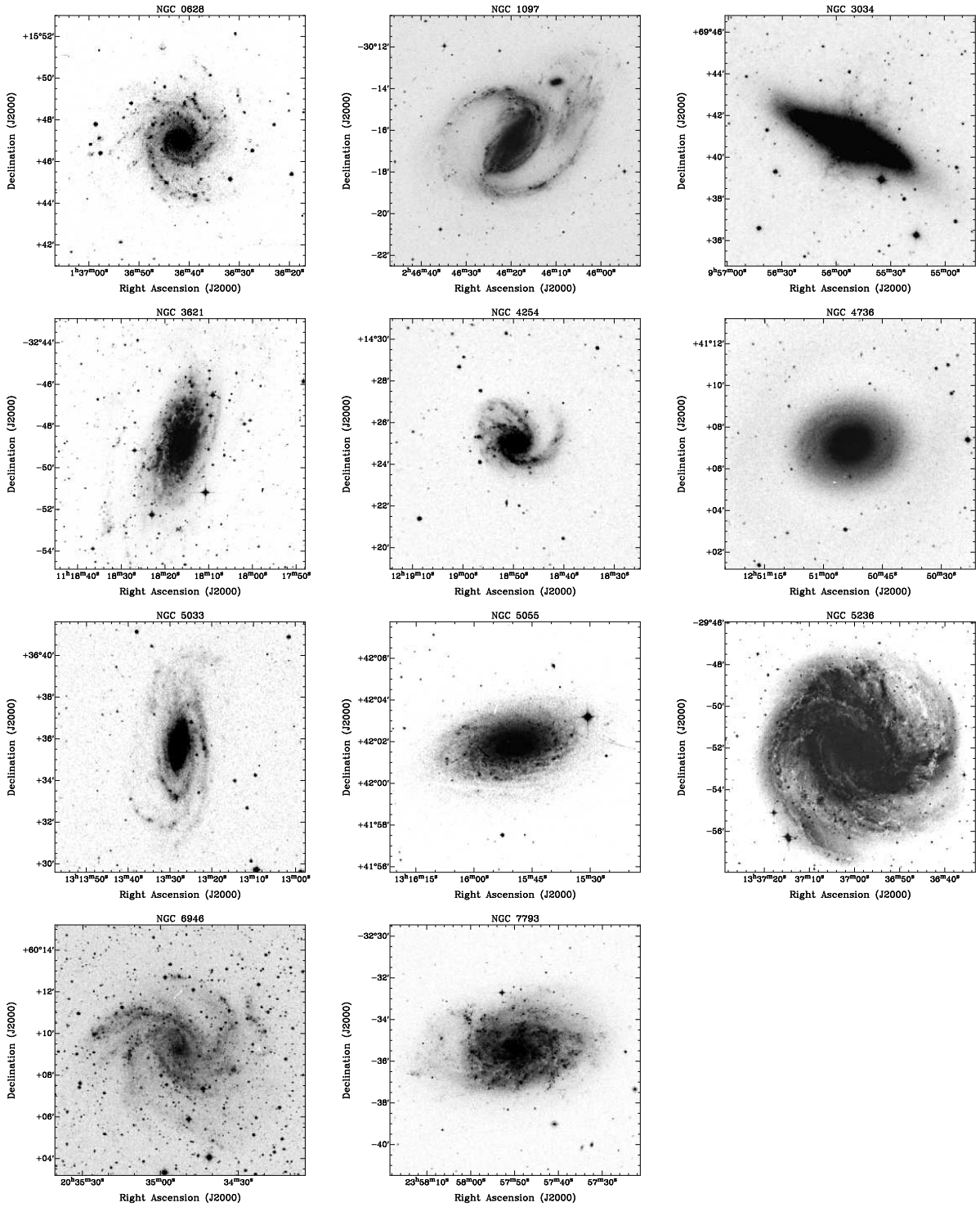

Figure 3.2: The optical DSS image of the sample galaxies observed by the GMRT. All the images are 12×12 arcmin^2 in size.

GHz and 1.4 GHz at an angular resolution of 66 arcsec by Paladino, Murgia & Orrú (2009) using the VLA. The spiral arm structure was not discernible in their image due to poor angular resolution. They studied the spectral index variation across the galaxy, in which it was found to be ~ 0.6 towards the centre and steepened to ~ 1 towards the edge.

From the radio continuum study at 1.36 GHz of Braun et al. (2007), this galaxy is expected to have an angular size of ~ 10 arcmin at 0.33 GHz. This requires full UV-coverage while observing with the GMRT at 0.33 GHz to detect all the features reliably. However, due to seven non-working antennas during the observation, this galaxy could not be imaged with high sensitivity. We have therefore not used the data on this galaxy for the thesis.

NGC 1097, in the optical is a spectacular barred spiral galaxy with prominent dust lanes in the bar. The central bar extends for about 20 kpc from the centre and then continues into the two optical spiral arms. The galaxy has an active Seyfert nucleus, and a circumnuclear ring of about 1.5 kpc diameter. Amongst the major radio continuum studies of this galaxy, Ondrechen & van der Hulst (1983) reported radio emission at 1.465 GHz coincident with the narrow dust lanes in the bar. Recently Beck et al. (2005) obtained a spectral index map for this galaxy from observations at 4.8 and 8.4 GHz, which revealed relatively steep spectral index of $\sim$1 in the inner ridge of the bar, and becoming shallower to ~ 0.7 as one moves to the outer ridge.

NGC 3621 is an inclined galaxy ($i = 65°$) with loosely wound spiral arms (Buta, Corwin & Odewahn, 2007). The optical spectra shows Seyfert-2 emission line spectra suggesting presence of black hole (Barth et al., 2009) even though no evidence of bulge is seen from decomposition of Two Micron All Sky Survey images. This galaxy hosts both active nuclei and nuclear star cluster (Barth et al., 2009). No major radio continuum study exists in the literature for this galaxy.

This galaxy lacked CO data and is not used in this thesis. The 0.33 GHz GMRT data is being analyzed.

NGC 3034 (M82) is a prototypical, starburst, edge-on galaxy. The galaxy was initially classified as irregular, however recently Mayya, Carrasco & Luna (2005), have reported the discovery of two symmetric spiral arms in the near infra-red. The galaxy is bright in the radio continuum, and has a synchrotron emitting halo extending up to a diameter of about 8 kpc. Based on a low frequency spectral index study of the whole galaxy from 0.33 to 4.835 GHz, Seaquist & Odegard (1991) found a spectral index of ~ 0.4 in the nuclear region, steepening to ~ 1 at a radius of 1 kpc due to transport of

CRes from the disk by galactic winds.

NGC 4254 (M99) is a face-on ($i = 34°$) galaxy with prominent spiral arms and is located in the outskirts of the Virgo cluster. This galaxy has an optical size of ~ 6.5 arcmin. Deep HI observations revealed tail of clouds extending to ∼11 arcmin in the northern direction (Phookun, Vogel & Mundy, 1993) that could be modelled by tidal encounter and ram pressure stripping (Vollmer, Huchtmeier & van Driel, 2005). Kantharia, Rao & Sirothia (2008) studied the radio continuum properties of this galaxy at 0.24, 0.325, 0.61 and 1.28 GHz. They report the total spectral index in the disc of the galaxy to lie in the range $\sim 0.4 - 0.8$ while in the outer parts it steepens to $\sim 1.2 - 1.8$.

NGC 4736 (M94) is the nearest large spiral galaxy with double ringed morphology. The inner ring is mainly made of recent star forming HII regions, showing bremsstrahlung spectra (Duric & Dittmar, 1988) and is distinctly visible in the Hα. The outer ring however is a low surface brightness feature in the optical. The rings were suggested to be caused by inner and outer Lindblad resonances (Schommer & Sullivan, 1976). The radio continuum study by de Bruyn (1977) between 0.61 and 1.415 GHz, presented spectral index maps with the spectral index being ~ 0.5 towards the centre of the galaxy and steepening towards the outer parts of the galaxy.

NGC 5033 is a tidally distorted galaxy with Seyfert-I nucleus. This galaxy is highly inclined with $i = 68°$. One of the southern arms of this galaxy has different pitch angle than other arms, perhaps due to the tidal interaction. In the radio continuum, this galaxy is seen to have a bright inner disc and a faint outer disc at 1.36 GHz (Braun et al., 2007).

The diffuse emission from the disk of this galaxy is not detected by the GMRT at 0.33 GHz except for the central 2×1 arcmin^2 region. The rms noise is 500 μJy beam^{-1} and the central region is a source with total flux density of 350 mJy mostly originating from the Seyfert nuclei. This galaxy could not be used for our intended spatially resolved study and is therefore not used in this thesis.

NGC 5055 (M63) is a nearby flocculent spiral which has short multiple arms. Although this galaxy lacks organized spiral arms in the optical, polarization observation at 10.55 GHz shows regular, spiral magnetic fields with radial component due to possible dynamo action (Knapik et al., 2000). Radio continuum spectral index maps between 0.61 and 1.417 GHz by Hummel & Bosma (1982) showed spectral index of about 0.6 in the central regions of the galaxy, which steepens to ~ 1 towards the outer parts. The galaxy appears featureless in the above radio continuum study as well as

in the high frequency 10.7 GHz map by Klein & Emerson (1981).

NGC 5236 (M83) is a large barred spiral galaxy and is seen almost face-on. The central bar extends up to 3 arcmin ($\sim$ 4 kpc), showing clear dust lanes. The galaxy is bright in radio continuum and the central bar and the disk is seen in the 1.465 and 4.885 GHz observation of Ondrechen (1985). Sukumar, Klein & Graeve (1987) found the total and nonthermal integrated spectral index to be 0.75 and 0.8 respectively, obtained between 0.327, 1.465 and 4.75 GHz and a thermal fraction of 20 percent at 4.75 GHz.

NGC 6946 is a large spiral galaxy with multiple arms. The galaxy has well separated arm and interarm regions and has been the subject of several studies in the radio continuum. There are several star forming regions in the galaxy and one of them shows the first likely detection of 'anomalous' dust emission, due to spinning dust, outside of the Milky Way (Murphy et al., 2010). Observations at 0.61, 1.415 and 5 GHz by van der Kruit, Allen & Rots (1977) revealed a bright radio disk of nonthermal origin. Based on 10.7 GHz observations, Klein et al. (1982) estimated a thermal fraction of 19 ± 10 percent. The spectral index study by Beck (2007) between 1.465 and 8.5 GHz, clearly shows a flatter spectral index of $\sim$ 0.5 in the arms which steepens to about $\sim$ 1 in the interarm regions.

NGC 7793 is a nearby large spiral galaxy with multiple spiral arms when seen in the optical (see Figure 3.2) and $\lambda 24 \mu$m in the far infrared. The Hα image reveals multiple compact regions along the arms undergoing star formation. This galaxy has been studied in the radio continuum at 0.327 GHz and 1.4 GHz at a resolution of 20 arcsec by Paladino, Murgia & Orrú (2009). The global spectrum could be well represented by synchrotron self-absorption at low radio frequencies below $\sim$ 0.2 GHz (Paladino, Murgia & Orrú, 2009). They found the spectral index to vary from $\sim$ 0.6 in the centre to $\sim$ 1 towards the edge of the galaxy.

We have not used the data on this galaxy due to non-availability of complimentary dataset tracing the CO emission. The 0.33 GHz GMRT data is being analyzed.

3.2 Radio frequency observations and analysis

We conducted interferometric observations at 0.33 GHz for the galaxies in our sample with the Giant Meterwave Radio Telescope (GMRT) near Pune, India (Swarup et al., 1991). The data with 16 MHz bandwidth (corresponding to $\nu_{\rm RF}$ of 0.325 to 0.341 GHz,

Table 3.2: Observational summary of 0.33 GHz observations of our sample galaxies. Time spent on source excludes calibration overheads. Column (5) gives the synthesized beam achieved and column (6) gives the map rms ($\sigma_{\rm map}$). Column (7) gives the integrated flux of the source inside the $\sim 3\sigma_{map}$ contour. $^{\oplus}$The data on the four galaxies at the bottom are not analyzed.

Name	Obs. date	Time on source (hrs)	Calibrators	used	Synthesized beam ($''\times''$)	σ_{map} (μJy/beam)	Integrated Flux (Jy)
(1)	(2)	(3)	(4)		(5)	(6)	(7)
NGC 1097	29-Oct-09	6	*Flux Cal:*	3C48	16×11	300	2.0±0.14
				3C286			
			Phase Cal:	0116-208			
				0409-179			
NGC 3034	31-Oct-09	4.5	*Flux Cal:*	3C48	22×15	3000	14±1
(M82)			*Phase Cal:*	0834+555			
				1459+716			
NGC 4254	23-May-12	4.6	*Flux Cal:*	3C286	13×11	230	1.7±0.2
(M99)			*Phase Cal:*	3C286			
NGC 4736	04-Jul-09	7	*Flux Cal:*	3C286	13×12	250	0.9±0.06
(M94)			*Phase Cal:*	3C286			
NGC 5055	02-Nov-09	3	*Flux Cal:*	3C286	17×10	240	2.3±0.2
(M63)			*Phase Cal:*	3C286			
NGC 5236	31-Oct-09	5	*Flux Cal:*	3C286	16×12	500	7.4±0.5
(M83)			*Phase Cal:*	1311-222			
NGC 6946	29-Jul-09	6.5	*Flux Cal:*	3C286	12×11	300	4.3±0.24
				3C147			
			Phase Cal:	1459+716			
				2350+646			
							Comments
NGC 0628$^{\oplus}$	07-Sep-12	7	*Flux Cal:*	3C48	22×18	700	Undetected
			Phase Cal:	3C48			
NGC 3621$^{\oplus}$	09-Jun-12	5.5	*Flux Cal:*	3C147	–	–	Data being analyzed
				3C286			
			Phase Cal:	1154-350			
NGC 5033$^{\oplus}$	10-Jun-12	8	*Flux Cal:*	3C286	11×10	500	Only inner disc
			Phase Cal:	3C286			detected
NGC 7793$^{\oplus}$	08-Sep-12	4.5	*Flux Cal:*	3C48	–	–	Data being analyzed
			Phase Cal:	0025-260			

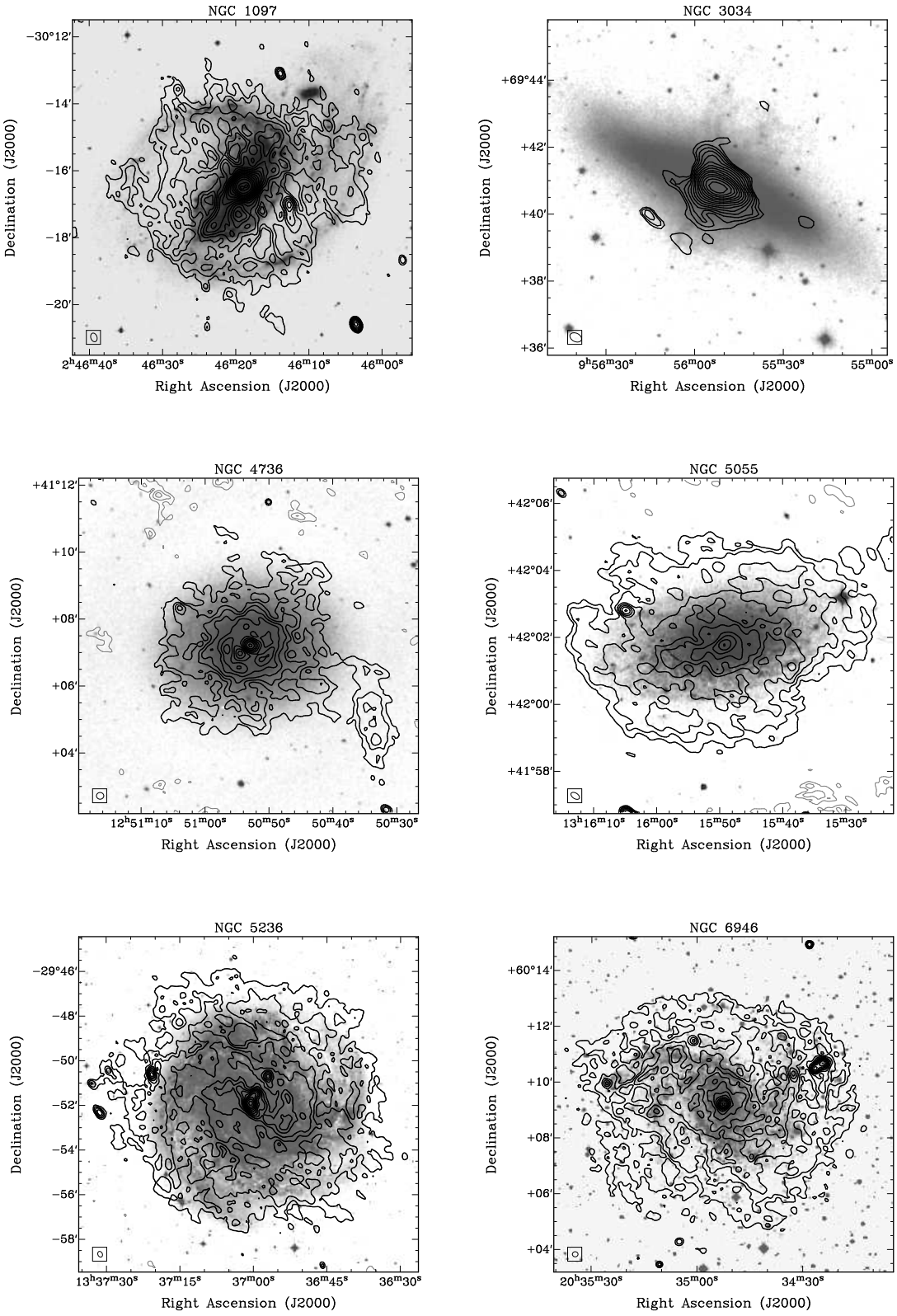

Figure 3.3: The contour maps are GMRT 0.33 GHz observations of the sample galaxies which are overlaid on the optical DSS image in grayscale. The contour levels starts from 3σ, increasing in multiples of $\sqrt{2}$. The grey contours shows $(-2, -3, -4) \times \sigma$.

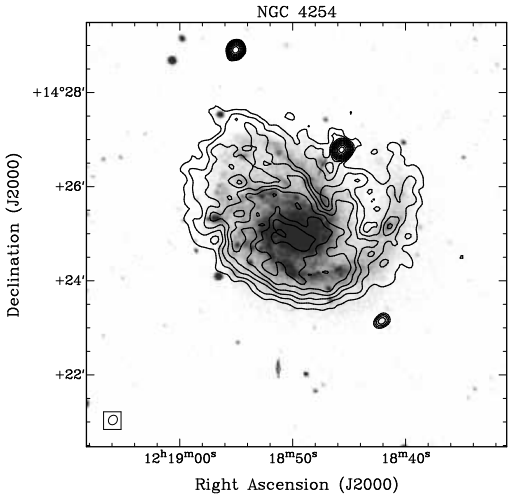

Figure 3.3: continued...

and a centre $\nu_{\rm RF}$ of 0.333 GHz), divided into 128 channels, were recorded following the usual protocol of observing flux and phase calibrator interlaced with observation on the source. At the beginning and end of the observing run, one of the flux calibrators 3C48, 3C286 or 3C147 was observed for about $\sim 10-20$ minutes. Phase calibrators were observed every $\sim$30$-$35 minutes for $\sim$4$-$5 minutes. Calibrators chosen for each of the observed sources are listed in Table 3.2.

Data reduction was done using the Astronomical Image Processing System (AIPS) as described below. After editing the data for strong *radio frequency interference* (RFI), standard flux and phase calibration were applied to the source. The Baars et al. (1977) absolute flux density scale was used to determine the flux densities of the flux calibrators and then applied them to the phase calibrator and the source.

The task 'FLGIT' was used to remove low level RFI at $4-6\sigma$ level across the frequency channels. This task fits a baseline across frequency channels for each integration time and removes those channels that are deviant by the user specified threshold. Even lower level RFI was subsequently removed using the tasks 'TVFLG', 'WIPER' and/or 'SPFLG'. The procedure was iteratively done by obtaining the gain solutions after every RFI removal stage. The complex gain of an interferometer can vary both in amplitude and phase as a function of frequency and time. The amplitude can vary in time due to changes in instrumental gain during the observation run and the phase can very due to

Table 3.3: Multifrequency integrated flux density for our sample galaxies.

Source	Frequency (GHz)	Flux density (Jy)	Ref.
NGC 1097	0.333	2.1±0.14	This work
	1.365	0.350±0.025	1
	1.465	0.42±0.02	VLA CD array
	1.665	0.262±0.030	1
	4.850	0.142±0.012	1
	8.450	0.094±0.018	1
NGC 3034	0.038	23±3	2
	0.178	14.6±0.7	2
	0.333	14±1	This work
	0.750	10.7±0.5	2
	1.415	8.0±0.4	3
	2.695	5.7±0.3	2
	5.0	3.9±0.2	2
	10.7	2.25±0.06	4
	14.7	1.79±0.04	4
NGC 4254	0.240	1.96±0.3	22
	0.323	1.7±0.2	This work
	0.325	1.6±0.2	22
	0.430	1.26±0.1	25
	0.610	1.08±0.1	22
	1.280	0.377±0.03	22
	1.430	0.512±0.019	23
	1.465	0.475±0.015	VLA C array
	4.86	0.162±0.006	23
	8.46	0.102±0.005	23
	10.55	0.093±0.009	24
NGC 4736	0.333	0.9±0.06	This work
	0.408	0.539±−	5
	0.610	0.435±0.026	7
	1.365	0.320±0.01	6
	1.415	0.276±0.02	7
	4.995	0.111±0.01	7
	10.7	0.096±0.018	8
	15	0.017±−	9
NGC 5055	0.333	2.3±0.13	This work*
	0.408	1.16±0.022	5
	0.610	0.83±0.04	10
	0.750	0.88±-	11
	1.417	0.409±0.02	10
	1.696	0.285±0.02	WSRT
	2.295	0.26±0.02	12
	3.7	0.254±−	13
	10.7	0.117±0.026	14

Table 3.3: continued... Multifrequency integrated flux density for our sample galaxies.

Source	Frequency (GHz)	Flux density (Jy)	Ref.
NGC5236	0.327	6.86±0.62	15
	0.333	7.3±0.4	This work
	1.452	2.3±0.15	VLA CD array
	1.465	2.2±0.11	15
	2.7	1.24±−	16
	4.75	0.97±0.13	15
NGC 6946	0.158	$7.54^{+2.40}_{-3.54}$	17
	0.178	5.88±0.44	18
	0.333	4.5±0.24	This work
	0.408	3.95	5
	0.610	2.34	19
	1.415	1.54±0.10	19
	1.465	1.41±0.08	VLA C+D array
	2.695	0.83±0.03	20
	4.86	0.54±0.05	VLA+Effelsberg
	8.50	0.45±0.05	21
	10.70	0.359±0.042	8

[1]Beck et al. (2002), [2]Kellermann, Pauliny-Toth & Williams (1969), [3]Hummel (1980), [4]Klein, Wielebinski & Morsi (1988), [5]Gioia & Gregorini (1980), [6]Braun et al. (2007), [7]de Bruyn (1977), [8]Klein & Emerson (1981), [9]Nagar, Falcke & Wilson (2005), [10]Hummel & Bosma (1982), [11]de Jong (1966), [12]Arp (1973), [13]Kuril'Chik, Onishchenko & Turevskil (1967), [15]Sukumar, Klein & Graeve (1987), [16]Wright et al. (1990), [17]Brown & Hazard (1961), [18]Caswell & Wills (1967), [19]van der Kruit, Allen & Rots (1977), [20]de Jong (1967), [21]Kuril'chik et al. (1970), [22]Kantharia, Rao & Sirothia (2008), [23]Chyży, Ehle & Beck (2007), [24]Soida, Urbanik & Beck (1996), [25]Israel & van der Hulst (1983).
*Note that the flux density measured by our observations is larger than that extrapolated from observations at higher radio frequencies. This is perhaps due to larger angular extent of the galaxy NGC 5055 (see Figure 3.3 and Section 4.4) at 0.333 GHz than at higher frequencies.

instrumental effects as well as varying ionosphere. For our observations, typically the phases varied within 10–20 degrees between scans on the phase calibrators for antennas with long baselines ($\gtrsim$10 km) where the effect of ionospheric variations are largest. For shorter baselines the phases varied less than 15 degrees. The gain variations are solved for both amplitude and phase by assuming a point source model for the calibrators. In that case the phase as a function of baseline length and time should be close to zero and the amplitude should be constant. Closure properties of phase and amplitude put further constraints while solving for the gains. The final gain solution that was applied to the target source when the closure errors were less than 1 percent on the phase calibrators.

The calibrated data were then used to obtain the deconvolved images using the task 'IMAGR'. Prior to this, the data were condensed in frequency by vector averaging 6 adjacent channels of 125 KHz each (resulting in channel width of 750 KHz) using the task 'SPLAT'. This ensured that the bandwidth smearing was less than the size of one synthesized beam at 0.33 GHz. To account for wide field imaging with non-coplanar baselines, the technique of polyhedron imaging was used in IMAGR (Cornwell & Perley,

1992), where the field of view is subdivided into a number of smaller fields (facets). For our purpose we used $7 \times 7 = 49$ facets covering the primary beam up to the half power beam width (HPBW $\sim 1.5^{\circ}$). Strong sources outside the HPBW, if present, were included in additional facets.

Several rounds of *phase only* self-calibration were done iteratively, by choosing clean components such that, the flux density within each synthesized beam is more than 8σ. Any stripe present in the map due to bad data, which remained unrecognized, were removed using a Fourier transform method[1]. In the first few rounds of the *phase only* self-calibration, the rms noise in the maps went down by more than 50 percent, i.e., the rms noise were typically $\sim 0.7 - 1$ mJy beam^{-1} initially and went down to $\sim 0.3 - 0.4$ mJy beam^{-1} after about 2–3 rounds. In the subsequent rounds of self-calibration, the rms noise improved at only few percent to 10 percent level. We used the field point sources to perform the first few rounds of *phase only* self-calibration as the entire galaxy was not visible due to low surface and high rms noise except for the bright core and few knots in the arm regions. However, after a few rounds of self-calibration when the map rms noise was low, the peak flux within the galaxy changed by less than 5 percent and the overall change in the galaxy structure between subsequent rounds were of the order of 10 percent or less. In the last iteration, one round of *amplitude and phase* self-calibration was done. The amplitude increased typically by $\lesssim 5$ percent after the *amplitude and phase* self-calibration. Final maps were made from full *uv* coverage and the *uv* data were weighted using Briggs' robust weighting of 0 (Briggs, 1995). Further, to account for sparse *uv* coverage at large *uv* distances, we used Gaussian *uv* tapering of $\sim 12 - 15$ kiloλ depending on the declination of the source. To CLEAN the extended diffuse emission from the galaxies we used SDI CLEAN algorithm (Steer, Dewdney & Ito, 1984). The final full resolution images obtained are shown in Figure 3.3 and their corresponding synthesized beams are listed in column 6 of Table 3.2.

The integrated flux density of the all the seven galaxies were obtained by integrating within the $3\sigma_{\rm map}$ (where $\sigma_{\rm map}$ is the map noise) contour and is given in Table 3.2. We compared the flux density obtained for each of our sample galaxies with measurements done at other radio frequencies by other researchers and are given in Table 3.3. Figure 3.4 shows the integrated broadband spectrum for our sample galaxies. Our flux density measurements are in good agreement with the interpolated flux densities from higher and lower radio frequency observations reported in earlier studies.

[1] see http://ncra.tifr.res.in/∼aritra/stripe_removal.pdf

The uncertainties in the estimated flux density ($S_{\rm source}$) depend on the rms noise in the map as well as on errors associated with uncalibrated system temperature ($T_{\rm sys}$) variations, which is about 5 percent (Roy & Rao, 2004) at 0.33 GHz for the GMRT. The flux density error ($\delta S_{\rm source}$) can be calculated as,

$$\delta S_{\rm source} = \sqrt{\left(\frac{\delta T_{\rm sys}}{T_{\rm sys}} \times S_{\rm source}\right)^2 + \sigma^2_{\rm map}}$$

The flux density also has an systematic error of about 8 percent associated with the absolute flux scale error at 0.33 GHz.

3.2.1 Missing flux density

For an interferometer with the shortest baseline $D_{\rm min}$, the deconvolution algorithm (CLEAN) can can recover all the flux from angular scales less than $\sim 0.6\lambda/D_{\rm min}$, provided the *uv*-plane is densely sampled at the shortest spacings. The galaxies in our sample have optical angular size less than $\sim$ 12 arcmin. For face-on galaxies, the optical and radio continuum sizes are comparable, however, for highly inclined galaxies, the sizes may differ slightly. In GMRT the projected shortest baseline $D_{\rm min}$ is $\lesssim$100 meters for full synthesis observations, which at 0.33 GHz allows to detect all the flux from angular scales less than $\sim$ 18 arcmin. Given that all the galaxies in our sample are less than $\sim$ 12 arcmin, the *uv*-plane is well sampled (see Figure 3.6) and hence we do not expect any *missing flux density*. The extent of missing flux density with our GMRT data was tested as follows: we took an existing archival 1.465 GHz map of NGC 6946, which was made by combining interferometric data from the VLA using C and D array (Beck, 2007). This galaxy is $\sim$ 11 arcmin in size. The map was then sampled to the 0.33 GHz GMRT *uv* coverage and subsequently imaged. All the flux in the source ($>$ 99 percent) could be recovered. Figure 3.5 shows the model GMRT map (right panel) made from the actual VLA map (middle panel). All the fine scale as well as large scale structures have been successfully recovered by the GMRT *uv* coverage. The integrated flux of the model GMRT map is within 2 percent of the actual flux measured by the VLA. The right panel of Figure 3.5 shows the difference image after subtracting the model map from the actual map. The residual is in units of Jy beam^{-1} and is within the map rms noise of the VLA image, which is $\sim$ 50 μJy beam^{-1}. This clearly shows that GMRT *uv*-coverage is sufficient to reliably image extended objects with angular size $\lesssim$ 15 arcmin. However, this is an issue for the archival higher frequency

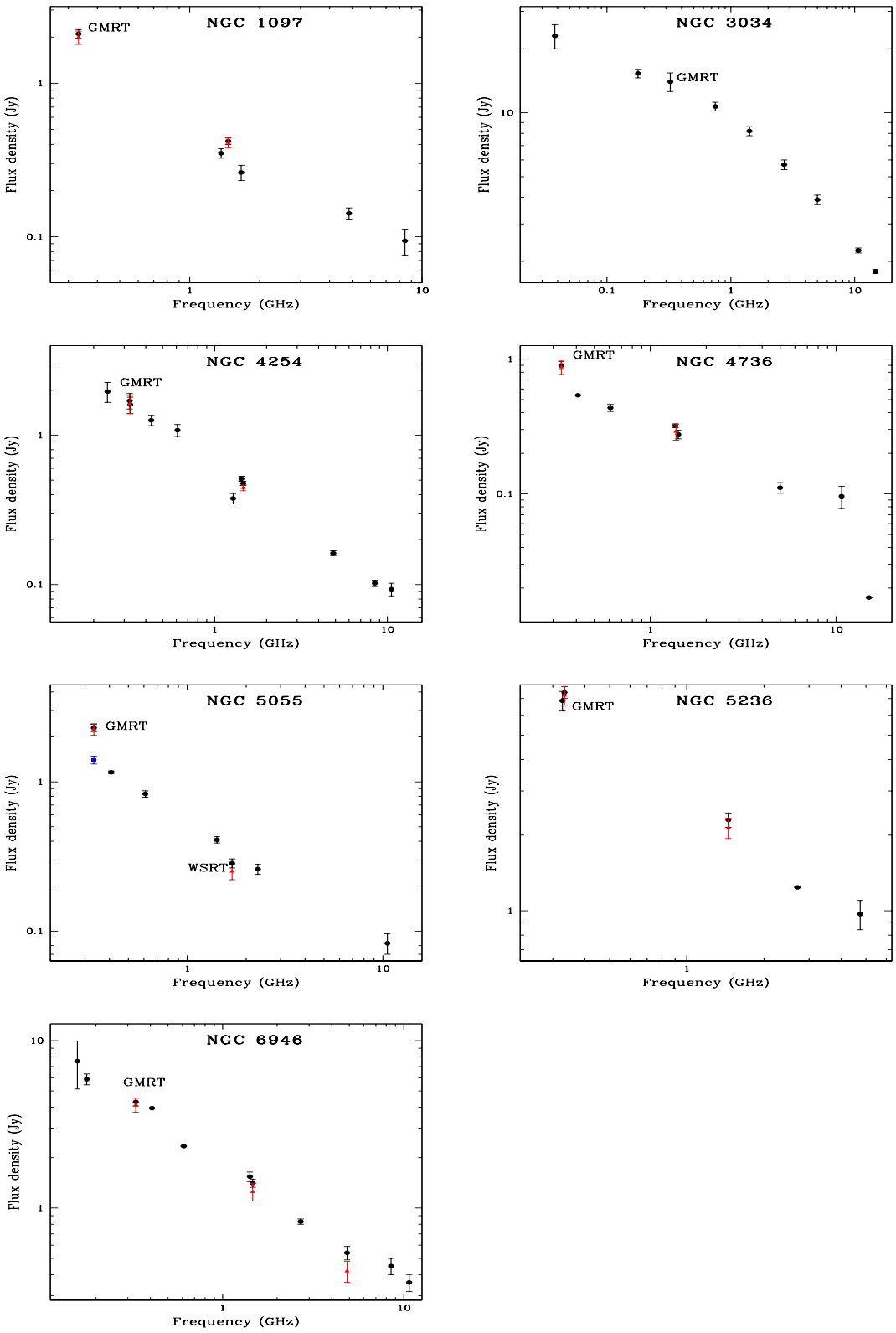

Figure 3.4: Integrated flux density as a function of frequency. The black circles represent the integrated flux densities without the thermal-nonthermal emission separation (see Table 3.3), while the red triangles represent the nonthermal flux densities of the galaxies (see Chapter 4). The 0.333 GHz flux density of the galaxy NGC 5055 is larger compared to that at higher frequencies due to its larger angular size at that frequency. The blue square for NGC 5055, is the flux density measured within 6.7×3.2arcmin^2, which is the size detected at higher radio frequencies (see Section 4.4).

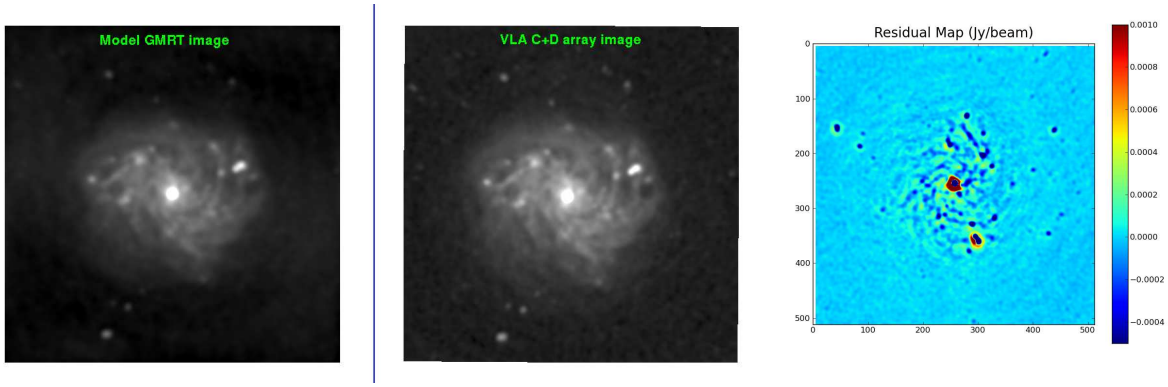

Figure 3.5: Comparison of model GMRT map (left panel) with the actual VLA map (middle panel). The right panel shows the residual map (in Jy beam^{-1}) after subtracting the model map from the actual map. The residual map is within the VLA rms noise of ~ 50 μJy beam^{-1}. This shows that the small scale as well as large scale structures are seen in the model image indicating sufficient *uv*-sampling.

data which is discussed below.

3.2.1.1 Archival data on the galaxies

NGC 1097: To find the spectral index with GMRT 0.33 GHz, we analyzed the archival 1.465 GHz data observed using CD array from the VLA (project code: AW237). The map has an angular resolution of 40×40 arcsec^2, and the shortest measured baseline is $\sim$150λ, which can detect angular scales up to $\sim$ 14 arcmin. However, the *uv* coverage is sparse for angular scales above $8'$ (see Figure 3.6). Since the size of the galaxy is about 9 arcmin, there could be missing flux density at large angular scales in these data.

NGC 3034: We used the archival 1.49 GHz VLA map (Condon, 1987, , obtained from the NED) at a resolution 60×60 arcsec^2 to obtain the spectral index with 0.33 GHz. The 1.49 GHz observations were made with the VLA D configuration with shortest baseline length of $\sim 170\lambda$, and are sensitive to angular sizes less than $\sim$ 12 arcmin. This should be sufficient to detect the galaxy, which has an optical size (D_{25}) of $\sim$ 11 arcmin. However, due to very bright emission from the core, the high resolution radio continuum map is dynamic range limited.

NGC 4254: We analyzed archival VLA C array data (project code: AU0076) at 1.465 GHz. The total emission map was made with an angular resolution of 14×13 arcsec^2 to obtain spectral index with 323 MHz. The VLA dataset had shortest baseline

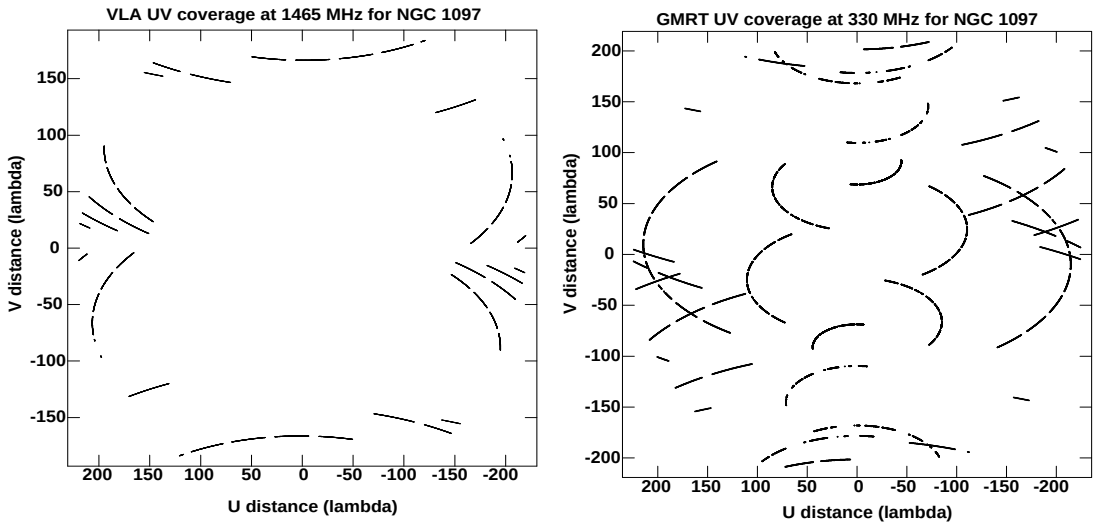

Figure 3.6: *uv* coverage in the range of *uv* distance 0–220λ for NGC 1097 at a declination of $\sim -30.25°$. The left plot is for the VLA in CD array and the right plot is for the GMRT. Sources of angular size above ~ 9 arcmin should be detected in this *uv* range. Note that the *uv* coverage for the VLA is sparse resulting in incomplete sampling of the *uv* plane, which leads to missing flux density problems above this angular scale. However, for the GMRT, several complete *uv* tracks are present.

of $\sim 150\lambda$ that corresponds to a maximum detectable angular size of ~ 14 arcmin. NGC 4254 has a maximum angular size of ~ 6 arcmin in the radio and therefore this map do not suffer any missing flux density.

NGC 4736: We used the archival WSRT[1] 1.375 GHz map taken from the Westerbork SINGS sample (Braun et al., 2007) at a resolution of 19×12.5 arcsec^2 after smoothing to 20×20 arcsec^2 to obtain the spectral index. The observations was made using the 'maxi-short' array configuration of the WSRT where the shortest east-west baseline was $\sim 170\lambda$, 250λ and 330λ (36, 54 and 72 meters respectively), and are sensitive to angular scales less than ~ 12 arcmin. NGC 4736, having a angular size of ~ 6 arcmin in the radio, has good sampling of the *uv*-plane and thus this map is not affected by lack of short spacing measurements.

NGC 5055: The archival 1.7 GHz map with resolution 18.5×12.5 arcsec^2 from the Westerbork SINGS (Braun et al., 2007) was used for obtaining the spectral index with 0.33 GHz, after smoothing to 20×20 arcsec^2. The 'maxi-short' configuration of the

[1]The Westerbork Synthesis Radio Telescope (WSRT) is operated by the Netherlands Foundation for Research in Astronomy (NFRA) with financial support from the Netherlands Organization for scientific research (NWO).

WSRT at 1.7 GHz allows us to image angular scales up to $\sim$ 10 arcmin. However, the *uv* coverage is too sparse to detect flux from structures above $\sim$ 7 arcmin. NGC 5055 has an angular extent $\gtrsim$ 8 arcmin, and thus we believe this map has missing flux density.

NGC 5236: The archival data at 1.452 GHz VLA CD array (project code: AS325) were downloaded and analyzed to produce a 26×14 arcsec^2 map, which was used for obtaining spectral index with our 333 MHz observations. The 1.452 GHz dataset had shortest baseline of $\sim 150\lambda$ which is sensitive to a maximum angular size of $\sim$ 14 arcmin. The *uv* coverage is sparse for structures above $\sim$ 10 arcmin. NGC 5236 is about 11 arcmin in size and hence there may be a small amount of missing flux density in this observation.

NGC 6946: For obtaining the spectral index with 0.33 GHz, we used an archival VLA 15×15 arcsec^2 map at 1.465 GHz. The VLA map was made by combining interferometric data from C configuration (Beck, 2007) and D configuration (Beck, 1991). Beck (2007) noted the integrated flux density from the VLA map and single dish Effelsberg measurement had similar values and there was no indication of missing large angular scale structures.

3.2.1.2 GMRT maps at 0.33 GHz

The 0.33 GHz GMRT observations of seven nearby galaxies (6–10 arcmin in size) with angular resolution better than 20 arcsec are by far the highest angular resolution maps for these galaxies at this frequency which are sensitive to both small ($\sim$ 0.5 kpc) and large ($\gtrsim$ 10 kpc) scale structures. These observations probe linear scales of about 0.4–1.5 kpc at the distance of the galaxies. The hybrid array of GMRT enables us to recover emission from both the diffuse and small scale emission in these sources, which we have adequately verified by comparing our estimated integrated flux densities with those available in the literature. The typical noise in the maps is $\sim$ 300 μJy beam^{-1} (except for NGC 3034), making them 10 times more sensitive than previous studies at similar frequency of other nearby galaxies (Heesen et al., 2009; Paladino, Murgia & Orrú, 2009; Sukumar, Klein & Graeve, 1987). All our maps have a dynamic range > 1000, which allows us to reliably determine the flux densities in regions near strong emission sites, mainly the nuclear region.

At 0.33 GHz the galaxies appear smoother than at higher frequencies, where spiral arms are often discernible. The thermal emission (which is primarily associated with

ionized structures observed in Hα maps) for all the galaxies is expected to be very low (less than 5 percent of the total emission, see Chapter 4), and hence at these frequencies, the emission is essentially nonthermal. The smooth appearance is consistent with the conjecture that nonthermal emission at 0.33 GHz primarily results from a population of old ($> 10^7$ yrs) CRes, which diffuses away from their formation sites filling up a volume of radius $\gtrsim 1$ kpc, without loosing much energy. This scale is larger than the width of the gaseous spiral arms and comparable to the width of the inter-arm region (see e.g., Condon, 1992), hence reducing any contrast in intensity across the galaxy. The prominent radio structures observed at higher frequencies (> 1 GHz) are due to enhanced thermal and enhanced synchrotron emission.

We emphasize that the GMRT 0.33 GHz images of the galaxies do not suffer from missing flux density, while some of the higher frequency maps (especially NGC 1097 and NGC 5055) may have missing flux density from large angular size structures. Thus, the true spectral index, particularly in the outer parts of the galaxies could be flatter than that determined in Chapter 4.

Chapter 4

Nonthermal emission from the galaxies

The radio continuum emission from normal galaxies originates from two emission processes: thermal free-free emission from HII regions predominantly seen at recent star formation sites, and the nonthermal synchrotron emission due to acceleration of cosmic ray electrons (CRes) in the ambient galactic magnetic field. A typical galactic magnetic field strength of a few microgauss (1 – 15 μG) and CRes in the energy range 1 to 10 GeV give rise to nonthermal radio emission between 0.1–10 GHz. However, only at frequencies below 1 GHz, does the thermal fraction of the emission reduce significantly, and hence low frequency studies are direct probes of nonthermal emission in galaxies.

It is now abundantly clear that CRes in normal galaxies are accelerated in supernova remnant shock fronts (with typical linear size < 1 pc) of Type II and Type Ib supernovae produced by short lived ($< 10^7$ yr) massive stars. Subsequently, the CRes diffuse away from their sites of origin and lose their energy primarily via synchrotron and inverse-Compton radiation in about $10^7 - 10^8$ yrs (see Condon, 1992, for a review). In turbulent magnetic fields, such as those encountered in the spiral arms, the CRe diffusion speed is the Alfvén speed ($\sim$ 100 km s^{-1}), and hence the CRes can expand to a volume of radius ~ 1 kpc without loosing much energy. The CRes can also propagate by diffusion to ~ 0.8 kpc assuming a diffusion coefficient of 10^{28} cm^2 s^{-1}. Note that the diffusion coefficient is larger along the magnetic field lines than across them. These increases the observed extent of the nonthermal emitting source. Note that the CRes would occupy a larger volume when observed at lower frequencies, since lower energy electrons suffer lesser energy loss and hence can diffuse farther. The CRes generated at the shock front

have steep electron energy spectra which results in a nonthermal synchrotron spectrum, well represented by a power law, $S_{\nu,\rm nt} \propto \nu^{-\alpha_{\rm nt}}$, where $S_{\nu,\rm nt}$ is the nonthermal radio flux density at a frequency ν and $\alpha_{\rm nt}$ is the nonthermal spectral index. The effects of CRe generation and propagation will cause $\alpha_{\rm nt}$ to vary from point to point in the galaxy. At the acceleration sites one expects $\alpha_{\rm nt} \sim 0.5$ to 0.7 (Bell, 1978; Biermann & Strom, 1993; Bogdan & Völk, 1983), getting steeper due to various losses as the CRes diffuse away (see Section 1.3.1).

To confirm the aforementioned scenarios a host of studies have been done in the past (see e.g. Beck et al., 2005; Beck & Graeve, 1982; Berkhuijsen, Beck & Hoernes, 2003; Carilli et al., 1992; Klein et al., 1982; Klein, Grve & Wielebinski, 1983; Murgia et al., 2005; Niklas, Klein & Wielebinski, 1997; Paladino, Murgia & Orrú, 2009; Segalovitz, 1977a,b; van der Kruit, Allen & Rots, 1977). However, due to the presence of thermal free-free emission, the $\alpha_{\rm nt}$ is contaminated, making the measured value flatter than the true value. This is because the thermal emission has a spectral index of 0.1, while the nonthermal emission is significantly steeper ($\alpha_{\rm nt} > 0.5$)[1]. At frequencies below 1 GHz, the nonthermal emission is expected to dominate. Niklas, Klein & Wielebinski (1997) have shown for a sample of 74 galaxies, about 8 percent of the emission at 1 GHz is thermal in origin. At even lower frequencies, the contribution of thermal emission reduces significantly, although there can be considerable local variation between, e.g., arms, interarms and giant HII regions etc., so as to make the separation of the thermal emission important. Previous studies at low frequencies probed linear scales larger than 1 kpc, and hence any small scale structures were lost. These considerations emphasize the importance of high resolution, low frequency observations and separation of thermal emission from the total emission to study the properties of nonthermal emission.

There are several techniques to separate the thermal emission from the total radio emission at radio frequencies. Contribution of the thermal and nonthermal emission to the total emission can be estimated by fitting the broadband spectrum of the total emission ($S_{\nu,\rm tot}$),

$$S_{\nu,\rm tot} = S_{\rm th}\nu^{-0.1} + S_{\rm nt}\nu^{\alpha_{\rm nt}}.$$

Here, $S_{\rm th}$ and $S_{\rm nt}$ are coefficients of thermal and nonthermal emission, and $\alpha_{\rm nt}$ is the nonthermal spectral index. In this method, there are 3 free parameters, namely, $S_{\rm th}, S_{\rm nt}$ and $\alpha_{\rm nt}$, which would require measurements at 4 different radio frequencies at least for

[1]Note that we use the parameter α for the total spectral index, where $S_{\nu,\rm tot} \propto \nu^{-\alpha}$, and $S_{\nu,\rm tot}$ is the total (thermal+nonthermal) flux density.

better solutions (see e.g. Duric, Bourneuf & Gregory, 1988). This method has been successfully used to determine the nonthermal emission for the integrated flux of the galaxies, however, it is difficult for spatially resolved studies as the signal-to-noise do not allow unique solutions. Moreover, these objects lack high quality interferometric data at higher frequencies which are not affected by missing flux problems as was pointed in Section 3.2.1.

In another technique, the thermal emission can be separated by estimating its contribution from tracers like Hα (Niklas, Klein & Wielebinski, 1997; Tabatabaei et al., 2007b) or dust emission at $\lambda 24$ μm. In this work we have used Hα emission from galaxies as a tracer of thermal emission following the novel technique developed by Tabatabaei et al. (2007b). We describe this method is detail.

4.1 Hα as tracer for thermal emission (kpc scales)

Hα emission in galaxies originates from the recombination of the same ionised gas as the bremsstrahlung emission and thus can be used to estimate the thermal emission (Valls-Gabaud, 1998). The Hα intensity, $I_{\rm H\alpha}$, can be written as,

$$I_{\rm H\alpha} = 9.41 \times 10^{-8} T_{e4}^{-1.017} 10^{-0.029/T_{e4}} \frac{EM}{\rm cm^{-6}pc} \quad {\rm erg\ cm^{-2}s^{-1}sr^{-1}} \tag{4.1}$$

Here, T_{e4} is the thermal electron temperature in units of 10^4 K and EM is the emission measure, defined as $EM = \int n_e^2 dl$, where, n_e is the thermal electron density. From the radiative transfer equation, flux density of the thermal emission, $S_{\nu,\rm th}$, at a radio frequency ν is given by,

$$S_{\nu,\rm th} = \frac{2kT_e\nu^2}{c^2}(1 - e^{-\tau}) \tag{4.2}$$

Here, k is the Boltzmann constant, T_e is the thermal electron temperature, c is the velocity of light and τ is the free–free optical depth. It can be shown that τ is related to EM as,

$$\tau = 0.0082\ T_e^{-1.35} \left(\frac{\nu}{\rm GHz}\right)^{-2.1} (1 + 0.08)\ EM \tag{4.3}$$

Since Hα emission is affected by extinction due to the presence of dust in the parent galaxies, far-infrared data at $\lambda 70\mu$m and $\lambda 160\mu$m are used to obtain a model for extinction, which is then used to correct the Hα data. The corrected Hα image is then used to predict the thermal emission at radio frequencies of interest (the method

is described in detail in sections 3 to 6 of Tabatabaei et al., 2007b).

We have applied the above method for separating thermal emission for six galaxies: NGC 1097, NGC 4254, NGC 4736, NGC 5055, NGC 5236 and NGC 6946. The far infrared data for the galaxy NGC 3034 was not usable for this study due to nonlinearities and streaking effects in the maps and therefore the data on this galaxy is not used for separating the thermal emission. We describe the ancillary data used and the various steps in this method.

(i) *Data sets.* The far infrared images at $\lambda 70\mu$m and $\lambda 160$ μm were obtained from the publicly available data from the *Spitzer Infrared Nearby Galaxy Survey* (SINGS; Kennicutt et al. 2003). All $\lambda 70$ μm images have a pixel size of 4.5 arcsec and a point spread function (PSF) of about 16 arcsec. At $\lambda 160$ μm, each pixel is 9 arcsec in size and has a PSF of 40 arcsec. Both the $\lambda 70$ μm and $\lambda 160$ μm maps are calibrated in surface brightness units of MJy sr^{-1}.

The continuum-subtracted Hα images for NGC 1097 (1.5-m CTIO, filter: CT6586), NGC 4254 (KPNO 2.1-m telescope, filter: KP1564) and NGC 6946 (KPNO 2.1-m telescope, filter: KP1563) were obtained from the ancillary data at the SINGS website. The maps were in units of DN s^{-1}pixel^{-1}, which was converted to erg s^{-1}cm^{-2} using the calibration provided in the SINGS Fifth Data Delivery documentation[1],

$$\frac{f_{\mathrm{H}\alpha}}{\mathrm{erg\ s^{-1}cm^{-2}}} = 3\times10^{-5}\times\mathrm{counts}\times\mathrm{PHOTFLAM}\times\frac{d\lambda}{\lambda^2} \tag{4.4}$$

Here, $f_{\mathrm{H}\alpha}$ is the intensity of Hα emission, counts is the value of the pixel, PHOTFLAM is the conversion factor provided in the FITS file header, $d\lambda$ is the FWHM of the filter in Angstrom and λ is the central wavelength of the filter in Angstrom.

The continuum-subtracted Hα images for NGC 4736, observed with the 1-m JKT at La Palma, filter: Ha6570, (Knapen et al., 2004), NGC 5055 observed with the 2.3-m telescope at KPNO, filter: 6580 and NGC 5236 observed with the 0.9-m telescope at CTIO, filter:6563 were downloaded from the NED.

The counts per second (cps), in these maps were converted to apparent magnitude, m_{AB}, using the zero-point (zp) given in the FITS file header. The apparent magnitude m_{AB} was further converted to specific intensity, using, $f_\nu(\mathrm{erg\ s^{-1}cm^{-2}Hz^{-1}}) = 10^{-(\mathrm{m_{AB}}+48.6)/2.5}$. The flux in units of erg s^{-1}cm^{-2} was computed using, $f = f_\nu d\nu = f_\nu c(d\lambda/\lambda^2)$.

All the $\lambda 70-\mu$m and continuum-subtracted Hα maps were convolved to the coarser

[1] http://data.spitzer.caltech.edu/popular/sings/20070410_enhanced_v1/Documents/sings_fifth_delivery_v2.pdf

40-arcsec PSF of $\lambda160\mu$m, and pixels were regridded to 9 arcsec. All the subsequent calculations were done on a pixel-by-pixel basis after aligning the maps to a common coordinate system.

(ii) *Dust Temperature and optical Depth.* Following Tabatabaei et al. (2007b), as a first step for extinction correction of Hα maps, the optical depth due to obscuring dust were estimated. For this the colour temperature ($T_{\rm dust}$) of the dust is found by fitting a modified black body spectrum accounting for dust absorption efficiency to the infrared maps at $\lambda70\mu$m and $\lambda160\mu$m, using,

$$I_{70\mu\rm m}/I_{160\mu\rm m} = (160\mu\rm m/70\mu\rm m)^{\beta}[B_{70\mu\rm m}(T_{\rm dust})/B_{160\mu\rm m}(T_{\rm dust})] \quad (4.5)$$

Here, $I_{70\mu\rm m}$ and $I_{160\mu\rm m}$ are the measured intensities at $\lambda70\mu$m and $\lambda160\mu$m respectively. β is the index of dust absorption efficiency between the above mentioned far infrared wavelengths and $B_{\lambda}(T_{\rm dust})$ is the Planck function. In our analysis, β was set as 2 (Draine & Lee, 1984). We used Newton-Raphson method to solve for $T_{\rm dust}$ in Equation 4.5. The distribution of the dust temperature for all the six galaxies are shown in the leftmost panel of Figure 4.1. The mean temperature estimated for all the galaxies is between 19−22 K. Note that a single dust temperature model has been assumed. The optical depth at 160μm ($\tau_{160\mu\rm m}$) was then obtained by using the equation, $I_{160\mu\rm m} = B_{160\mu\rm m}(T_{\rm dust})(1 - e^{-\tau_{160\mu\rm m}})$. The H$\alpha$ optical depth was obtained as $\tau_{\rm H\alpha} \sim f_{\rm d} \times 2200 \times \tau_{160\mu\rm m}$ (Krügel, 2003) where the Hα filling factor $f_{\rm d} = 0.33$ (Dickinson, Davies & Davis, 2003). For all the six galaxies the $\tau_{\rm H\alpha}$ lie in the range 0.03 – 0.6 at linear scales > 1 kpc, with the highest values being towards the center of the galaxies. The observed Hα intensity, $I_{\rm H\alpha,obs}$, was then corrected using, $I_{\rm H\alpha} = I_{\rm H\alpha,obs}e^{\tau_{\rm H\alpha}}$.

(iii) *Emission Measure.* Extinction-corrected Hα maps were used to estimate the emission measure using Equation 4.1 and assuming an electron temperature of $T_e = 10^4$ K. The emission measure radial profile for all the six galaxies are shown in the middle panel of Figure 4.1. The emission measure towards the center of the galaxies lie in the range $10^3 - 10^4$ pc cm^{-6} and falls off to $\sim 10 - 10^2$ pc cm^{-6} towards the edge of the galaxies. These range of emission measure values are consistent with those observed in the Milky way (see for e.g. Berkhuijsen, Mitra & Mueller 2006).

(iv) *Thermal emission at Radio frequencies.* We determined the optical depth of the thermal free–free emission using Equation 4.3 and subsequently estimated the thermal brightness temperature ($T_{\rm B}$) using, $T_{\rm B} = T_e(1 - e^{-\tau})$. The thermal flux density ($S_{\nu,\rm th}$)

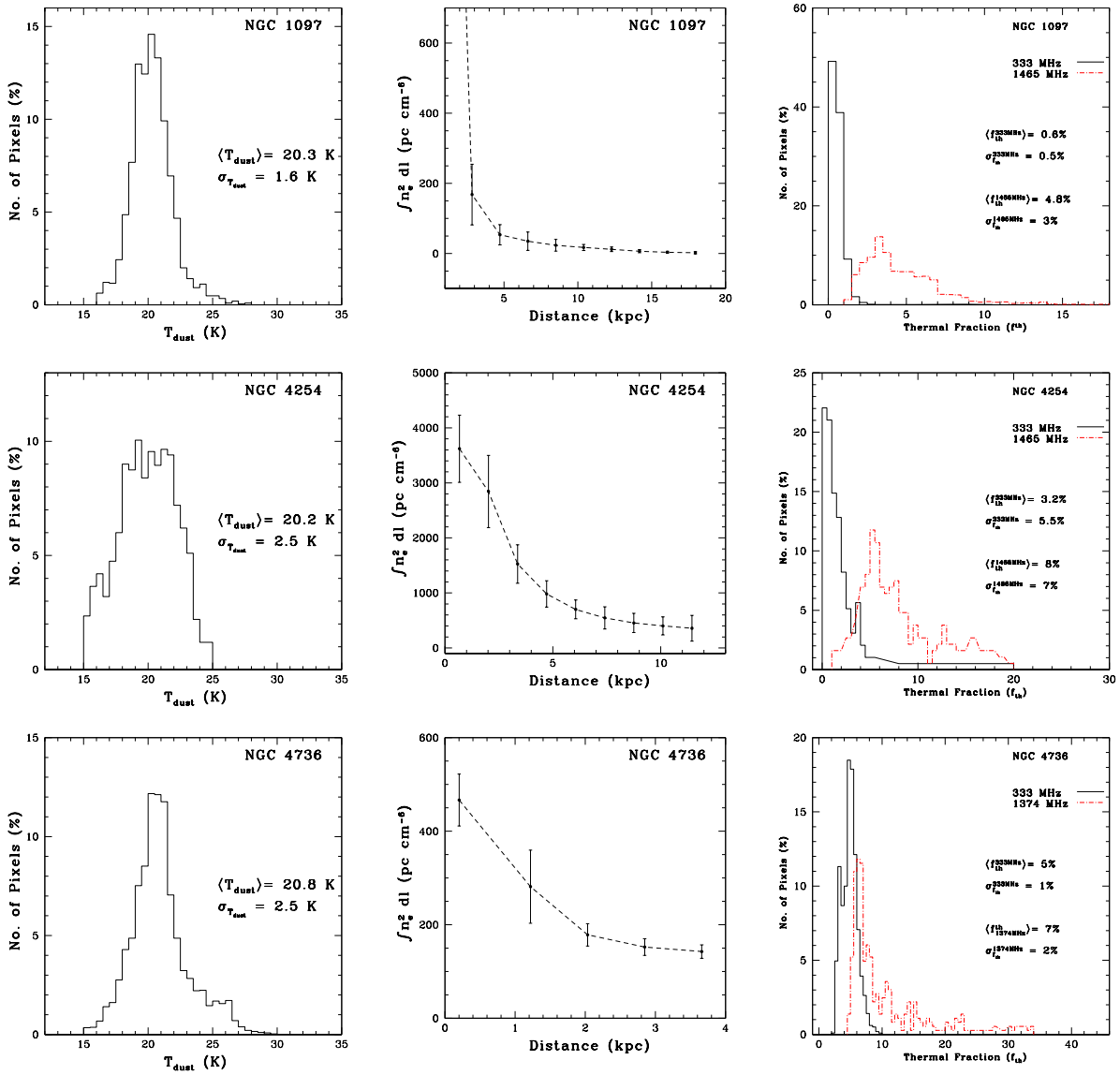

Figure 4.1: Left-hand panel: The pixel-wise distribution of the estimated dust temperature ($T_{\rm dust}$). The bins are at intervals of 0.5 K. Middle panel: The radial profile of the estimated emission measure ($EM = \int n_e^2 dl$ pccm^{-2}). The EM is azimuthally averaged over annuli of one beamwidth, i.e, 40 arcsec. Right-hand panel: The pixel-wise distribution of the thermal fraction ($f_{\rm th}$) with a bin size of 0.5 per cent. The solid black histograms show the distribution at 0.33 GHz, while the dashed red histograms show the distribution near 1.4 GHz. The top, middle and bottom rows are for NGC 1097, NGC 4254 and NGC 4736 respectively. Each pixel is of size 10 arcsec, corresponding to a physical scale of about 700, 750 and 400 pc respectively.

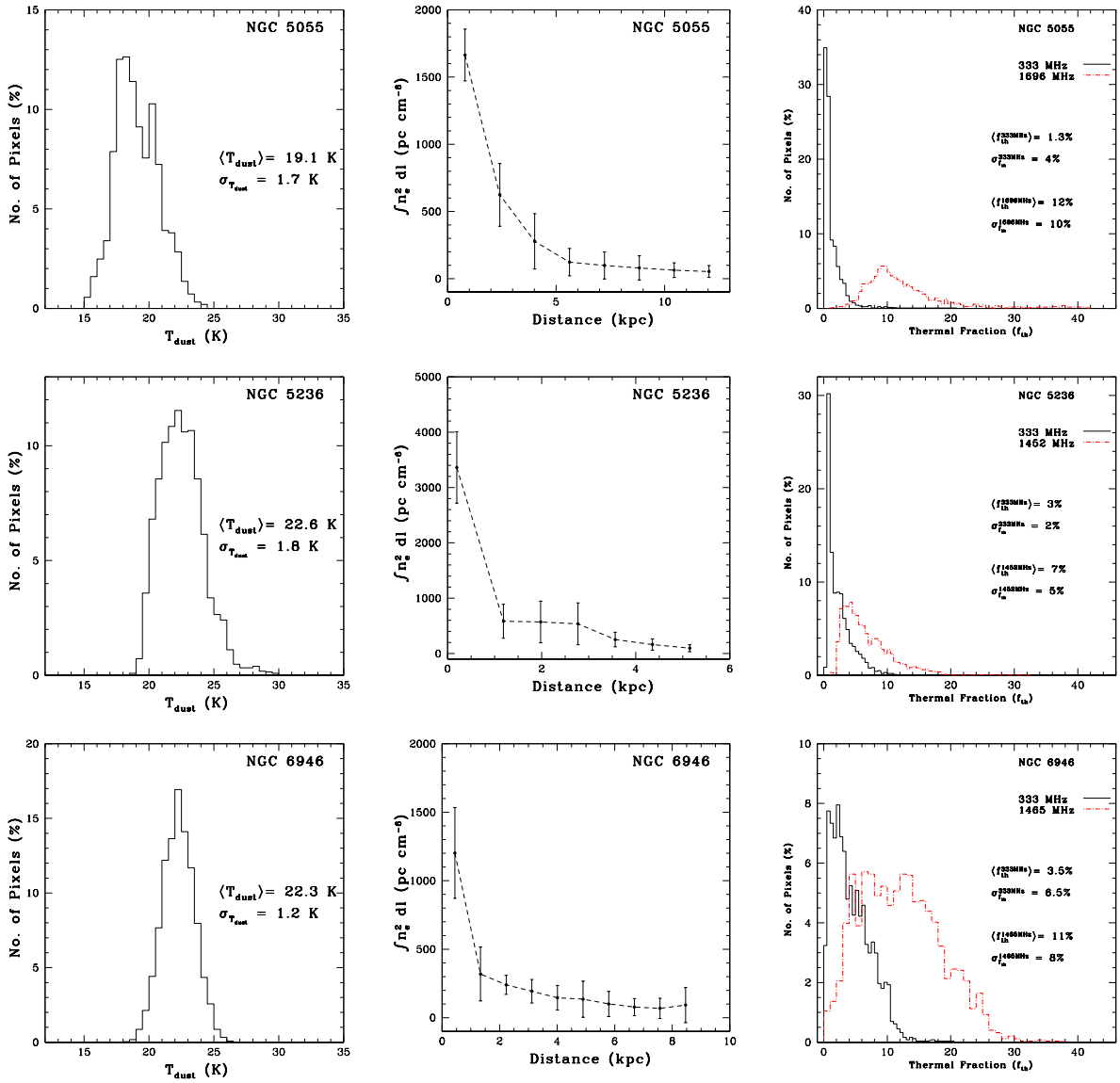

Figure 4.1: *continued...* Left-hand panel: The pixel-wise distribution of the estimated dust temperature ($T_{\rm dust}$). The bins are at intervals of 0.5 K. Middle panel: The radial profile of the estimated emission measure ($EM = \int n_e^2 dl$ pccm^{-2}). The EM is azimuthally averaged over annuli of one beamwidth, i.e, 40 arcsec. Right-hand panel: The pixel-wise distribution of the thermal fraction ($f_{\rm th}$) with a bin size of 0.5 per cent. The solid black histograms show the distribution at 0.33 GHz, while the dashed red histograms show the distribution near 1.4 GHz. The *top*, *middle* and *bottom* rows are for NGC 5055, NGC 5236 and NGC 6946 respectively. Each pixel is of size 10″, corresponding to a physical scale of about 340, 220 and 330 pc respectively.

at a radio frequency ν was obtained from the $T_{\rm B}$ using Rayleigh-Jeans approximation,

$$\frac{S_{\nu,\rm th}}{\rm Jy\ beam^{-1}} = 8.18 \times 10^{-7} \left(\frac{\theta_{\rm maj}}{\rm arcsec}\right) \left(\frac{\theta_{\rm min}}{\rm arcsec}\right) \left(\frac{\nu}{\rm GHz}\right)^2 \frac{T_{\rm B}}{\rm K}$$

Here, $\theta_{\rm maj}$ and $\theta_{\rm min}$ is the size of the restoring beam in the radio map (in this case 40 arcsec).

For all the six galaxies, the pixel-wise distribution of the thermal fraction[1] ($f_{\rm th}$) at 0.33 GHz and near 1 GHz are shown in the rightmost panel of Figure 4.1. The mean $f_{\rm th}$ at 0.33 GHz and near 1 GHz for all the galaxies were found to be less than 5 per cent and less than 12 per cent respectively. However, in certain giant HII regions, the thermal fraction can go up to 10 per cent at 0.33 GHz and 30 per cent near 1 GHz. Tabatabaei et al. (2007b) pointed out that the primary source of error in the thermal fraction arises from the unknown value of the T_e. Following Tabatabaei et al. (2007b), we estimate the uncertainty in the thermal fraction at 0.33 GHz and near 1 GHz to be $\sim$ 10 per cent and 15 per cent respectively.

We would like to point out that, using this method of separating the thermal emission, the resolution is limited by the 40-arcsec Spitzer λ160 μm maps which corresponds to 1–3 kpc at the distance of the galaxies. Though this resolution is enough to study the nonthermal properties in arms and interarms, it is not enough to study the variations in magnetic field. In Section 4.2 we discuss a new technique developed to separate the thermal emission using dust emission at λ24 μm as the tracer at resolutions better than the resolution of radio maps. Note that this technique was developed recently and is used only while deriving the magnetic field strength maps.

4.2 Hα corrected λ24 μm as tracer of thermal emission (sub-kpc scales)

Due to poorer resolution of the far infrared maps used for determining absorption correction of the Hα emission, the overall resolution of the nonthermal emission maps was only 40 arcsec. To improve the resolution of nonthermal emission we used λ24-μm emission from dust as a tracer of thermal emission (Murphy et al., 2006, 2008). All our sample galaxies were observed by the *Spitzer space telescope* as a part of the SINGS

[1]Thermal fraction is defined as: $f_{\rm th} = S_{\nu,\rm th}/S_{\nu,\rm tot}$, where, $S_{\nu,\rm th}$ is the flux density of the thermal emission. In the text we express $f_{\rm th}$ as percentages.

at λ24 μm with an angular resolution of $\sim$6 arcsec. The thermal emission maps could be obtained at that resolution, however, the resolution of the nonthermal maps are limited by the resolution of the total intensity radio images given in Table 4.1.

The Paschen-α (Paα) emission is related to the ionizing photon rate (Osterbrock, 1989), which is an indicator of star formation rate in galaxies as well as thermal free–free emission. However, detection of Paα emission from galaxies is challenging and it has been used to image only on a few galaxies. Paα emission can be calibrated from the λ24 μm emission as it is a tracer of star formation as well. The λ24 μm dust emission is also a tracer of star formation and is highly correlated with the Paα emission (see e.g. Calzetti et al., 2005) and can be used to estimate the later. The luminosity of λ24 μm ($L_{24\mu\mathrm{m}}$) and Paα ($L_{\mathrm{Pa}\alpha}$) are related through the following relation (Calzetti et al., 2005),

$$\log L_{24\mu\mathrm{m}} = (1.03 \pm 0.04) \log L\mathrm{Pa}\alpha + (0.9 \pm 1.3) \tag{4.6}$$

The λ24 μm emission can thus be scaled to the Paα emission, and further related to the free–free thermal emission in the radio by the formula (see Murphy et al., 2006; Rubin, 1968),

$$\frac{S_{\nu,\mathrm{th}}}{\mathrm{Jy\ beam^{-1}}} \sim 7.93 \times 10^{-3} T_{e4}^{0.45} \nu_{\mathrm{GHz}}^{-0.1} \left[\frac{f_{24\mu\mathrm{m}}}{\mathrm{Jy\ beam^{-1}}}\right] \tag{4.7}$$

Here, ν_{GHz} is the radio frequency in units of GHz. In this analysis, we used *Spitzer* MIPS λ24 μm maps which have a resolution of 6 arcsec, better than the resolution of the radio maps. The resolution of the nonthermal maps are determined by the lowest resolution radio maps and subsequently the λ24 μm maps were convolved to it. Though this method of separating the thermal emission improves the resolution of the nonthermal maps, however, we note that λ24 μm emission from dust is not a direct tracer of thermal emission. The calibration to obtain the Paα emission from the λ24 μm emission (Equation 4.6) was found for the galaxy M51. This relation is not universal and can show differences between galaxies and measurements made from using a direct tracer like Hα (Calzetti et al., 2005; Pérez-González et al., 2006). Moreover, the λ24-μm emission arises not only from dust grains heated by ultra violet photons, but also from heating of diffuse cirrus clouds by the interstellar radiation field and also from old stars, mostly from the central regions of galaxies. This could lead to overestimation of thermal emission in such regions. To avoid this shortcoming, and to ensure that both the methods give identical results at the resolution of the absorption corrected Hα emission, we corrected the thermal fraction determined from λ24-μm to

Table 4.1: The resolution of available radio maps in units of arcsec^2.

Name	λ90 cm	λ20 cm	nonthermal maps	linear scale (kpc)
NGC 1097	16×11	40×30	40×40	2.80
NGC 4254	13×11	20×20	20×20	1.50
NGC 4736	13×12	19×12.5	20×20	0.45
NGC 5055	17×10	18.5×12.5	20×20	0.90
NGC 5236	16×12	26×14	26×14	0.55
NGC 6946	12×11	15×15	15×15	0.50

Table 4.2: Mean values of the thermal fractions at λ20 cm determined using Hα method (column 2) and λ24μm method (column 3).

Name	$\langle f_{\rm th,H\alpha}\rangle$ (%)	$\langle f_{\rm th,24\mu m}\rangle$ (%)	$\langle f_{\rm th,H\alpha}/f_{\rm th,24\mu m}\rangle$
NGC 1097	5±3	7±2	0.75±0.3
NGC 4254	8±3	6±2	1.23±0.4
NGC 4736	7±2	10±2	0.67±0.2
NGC 5055	10±3	11±2	0.87±0.3
NGC 5236	7±2	8.5±3	0.73±0.3
NGC 6946	10±3	8.5±2	1.18±0.4

the thermal fraction from Hα following the method described below. All the maps were brought to the same pixel size (3 arcsec) and aligned to a common coordinate system. All the pixels with signal-to-noise ratio more than 4 were considered for this analysis.

In step (i), the convolved λ24-μm emission was used to estimate the thermal emission using Equation 4.7 at a resolution given in Table 4.1. We then estimated the thermal fraction at each pixel of the map. In step (ii), the maps made in step (i) are convolved to a resolution of 40 arcsec. At this resolution, the thermal fraction maps made from λ24 μm ($f_{\rm th,24\mu m}$) must match the corresponding thermal fraction maps made from Hα ($f_{\rm th,H\alpha}$). Therefore, in step (iii) we divided the thermal fraction maps made from Hα by the maps made in step (ii). In step (iv), the correction factor to scale the $f_{\rm th,24\mu m}$ for each pixel was determined within beam of 40 arcsec from the ratio map determined in step (iii). This correction factor for each pixel was multiplied with map (i) to obtain the corrected thermal fraction map ($f^{\rm corr}_{\rm th,24\mu m}$). We note that the ratio of $f_{\rm th,H\alpha}$ and $f_{\rm th,24\mu m}$ determined in step (iii) is expected to be ~ 1. However, Equation 10 in Murphy et al. (2008) uses the calibration for the galaxy M51 to scale dust emission at λ24 μm to trace thermal emission. This is known to vary between galaxies and

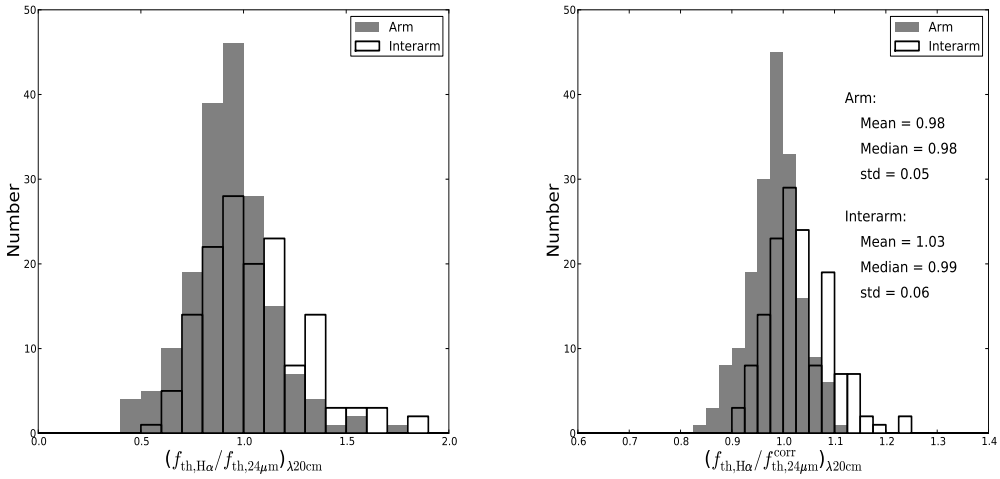

Figure 4.2: Left panel shows the histogram of the correction factor $(f_{\rm th,H\alpha}/f_{\rm th,24\mu m})$ after normalizing with median values of the ratio for each of the galaxies. Right panel shows the distribution of $f_{\rm th,H\alpha}/f^{\rm corr}_{\rm th,24\mu m}$ for all the galaxies at 1.4 GHz determined within 40 arcsec regions. The grey and unfilled histograms are for arm and interarm regions.

may have systematic offsets between $f_{\rm th,H\alpha}$ and $f_{\rm th,24\mu m}$. Table 4.2 shows the thermal fraction determined using the Hα- and λ24μm-method (columns 2 and 3 respectively). The two methods match well within $\sim$ 30 percent of each other. The mean correction factor for each of the galaxies are listed in column 4 of Table 4.2. The correction factor would take care of the systematic calibration-offsets between galaxies. As pointed out earlier, the thermal emission is overestimated due to the use of λ24 μm, however, NGC 4254 and NGC 6946 shows higher thermal fraction from the Hα method perhaps be due to unknown thermal electron temperature. A detailed study exploring the dust emission properties and Hα attenuation for these galaxies are necessary to understand this. The resultant maps provide us with thermal fraction of the galaxies with a resolution better than 40 arcsec. Figure 4.2, left panel shows the histogram plot of the ratio $f_{\rm th,H\alpha}/f_{\rm th,24\mu m}$ determined within regions of 40 arcsec for all the galaxies at λ20 cm. The ratio has been normalized by the median values of each galaxy to account for the systematic offset between galaxies. The grey and unfilled histograms are for arm and interarm regions respectively. For $\sim$ 65 percent of the regions, the ratio is seen to be smaller than unity suggesting λ24-μm emission to be higher than the star formation rate. Figure 4.2, right panel compares the thermal fraction determined within 40 arcsec

regions using Hα- and corrected λ24μm-method at λ20 cm. Although, after correction, $f^{\rm corr}_{\rm th,24\mu m}$ agrees with $f_{\rm th,H\alpha}$ within $\sim$ 10 percent, there is significant spread. However, to the first order, when compared to $f_{\rm th,H\alpha}$, $f^{\rm corr}_{\rm th,24\mu m}$ has significantly less spread and systematic offset than $f_{\rm th,24\mu m}$. Thermal emission was estimated using $f^{\rm corr}_{\rm th,24\mu m}$ and was subtracted from the total emission to obtain the nonthermal emission. The resolution of the nonthermal maps thus obtained using this method are given in Table 4.1.

4.3 Nonthermal spectral index ($\alpha_{\rm nt}$)

The nonthermal spectral index $\alpha_{\rm nt}$, is the main parameter of interest because it is used to model CRe generation and propagation. However, it is not possible to measure it directly. The quantity which is measured is the total spectral index α which is contaminated by thermal free-free emission. This contamination is significant for spatially resolved regions of the galaxy where $f_{\rm th}$ is high. In this section, we assess the effect of $f_{\rm th}$ on $\alpha_{\rm nt}$ obtained between 0.33 GHz and near 1.4 GHz in spatially resolved regions of the galaxy. To do this, we use the method described in Section 4.1 and apply it to six of the sample galaxies (except NGC 3034). The far infrared λ160μm map has an angular resolution of 40×40 arcsec^2, and hence the final nonthermal spectral index maps have this angular resolution, which is significantly coarser than the total spectral index (hereafter α) maps. The usefulness of this method lies in the fact that it can be used in spatially resolved parts of the galaxy. Further, Tabatabaei et al. (2007b) demonstrate the robustness of this method over several other existing thermal-nonthermal separation techniques (see references therein, Broadbent, Osborne & Haslam, 1989; Gioia, Gregorini & Klein, 1982; Hummel & Bosma, 1982).

The mean $f_{\rm th}$ for all our sample galaxies was found to be less than 5 percent at 0.33 GHz, although the value can go up to 10 percent in some specific bright HII regions and in the spiral arms. Applying the same method to the available higher frequency data at or close to 1.4 GHz, we found the mean $f_{\rm th}$ to be less than 12 percent. The distribution of the $f_{\rm th}$ at 0.33 GHz and near 1.4 GHz for six galaxies are shown in right most panels of Figure 4.1.

The nonthermal 0.33 GHz and higher frequency maps were further used to obtain $\alpha_{\rm nt}$ variation for the six galaxies. The left panels of Figure 4.3, shows the α maps and the right panels shows the $\alpha_{\rm nt}$ maps. Figure 4.4 shows the variation of α and $\alpha_{\rm nt}$ with radius for the galaxies. Here, the spectral index was estimated by azimuthally averaging

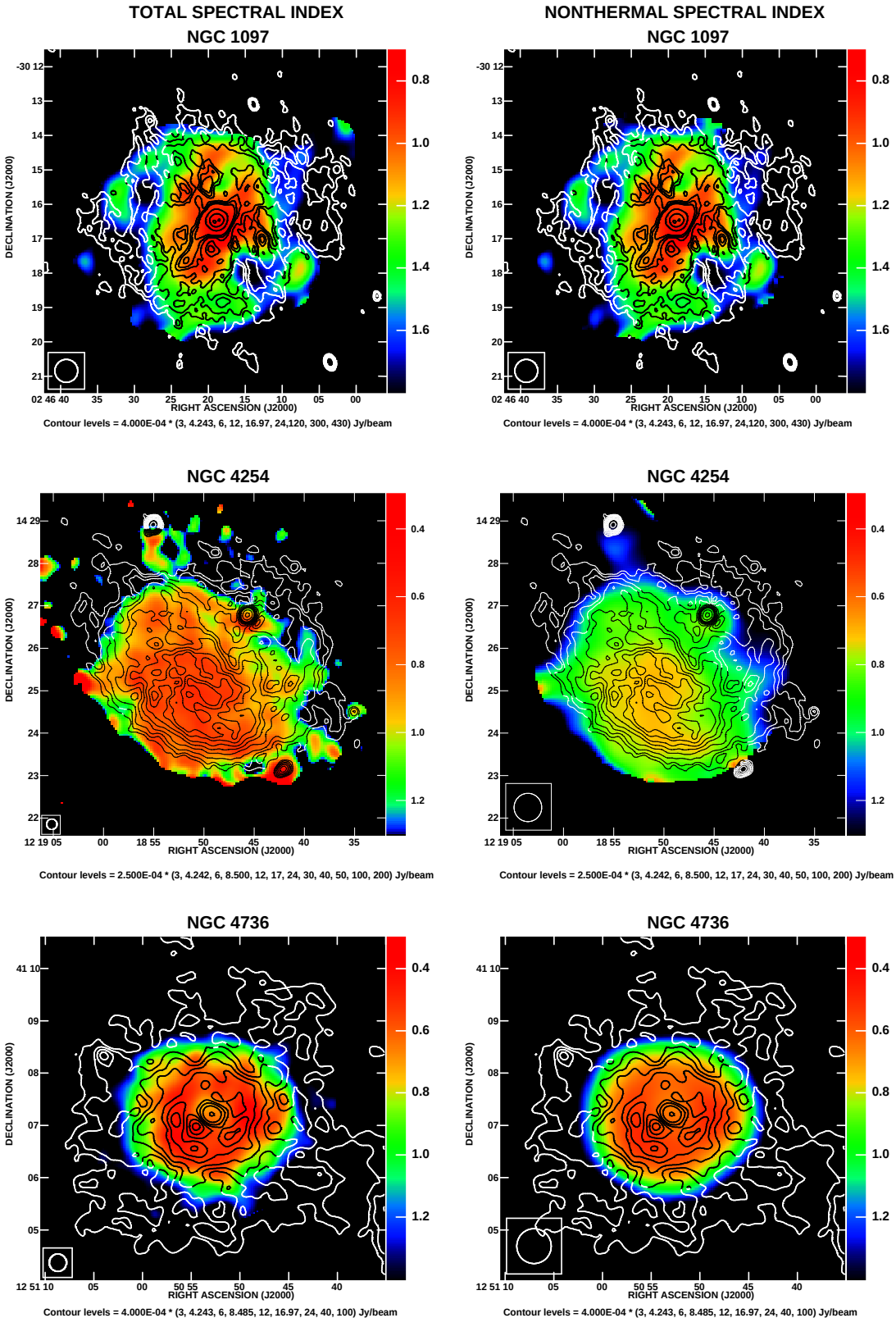

Figure 4.3: *Left column:* The total spectral index (α) maps between GMRT 0.33 GHz and near 1 GHz. The top row is NGC 1097, middle row is NGC 4254 and the bottom row is NGC 4736. The α maps for NGC 1097, NGC 4254 and NGC 4736 have a resolution of 40×40, 15×15 and 20×20 arcsec^2 respectively. *Right column:* The nonthermal spectral index ($\alpha_{\rm nt}$) between 0.33 GHz and near 1 GHz at resolution of 40 arcsec. Overlaid are the 0.33 GHz contours. Contour levels are indicated below each figure.

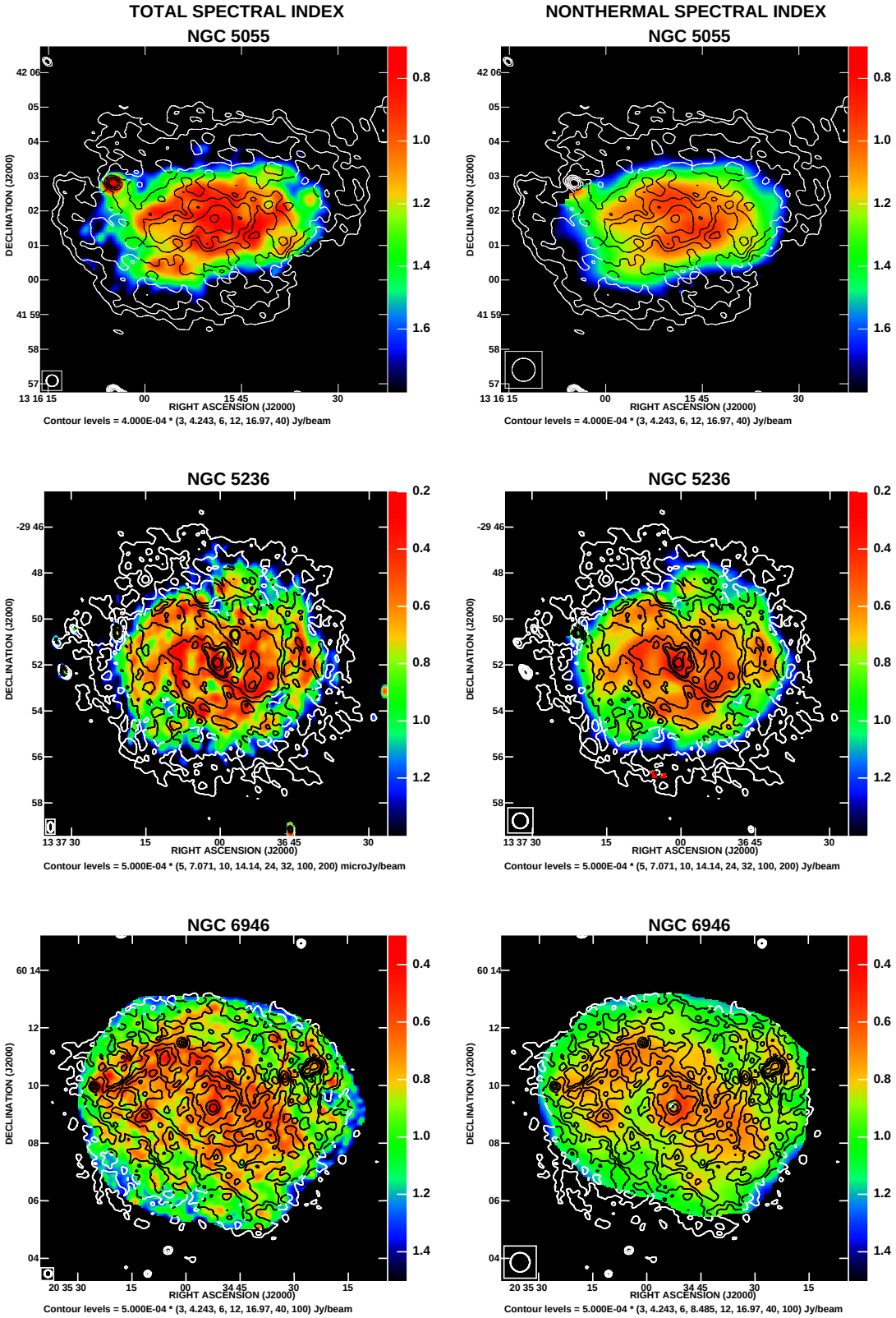

Figure 4.3: *continued... Left column:* The total spectral index (α) maps between GMRT 0.33 GHz and near 1 GHz. The top row is NGC 5055, middle row is NGC 5236 and the bottom row is NGC 6946. The α maps for NGC 5055, NGC 5236 and NGC 6946 have a resolution of 20×20, 26×14 and 15×15 arcsec^2 respectively. *Right column:* The nonthermal spectral index ($\alpha_{\rm nt}$) between 0.33 GHz and near 1 GHz at resolution of 40 arcsec. Overlaid are the 0.33 GHz contours. Contour levels are indicated below each figure.

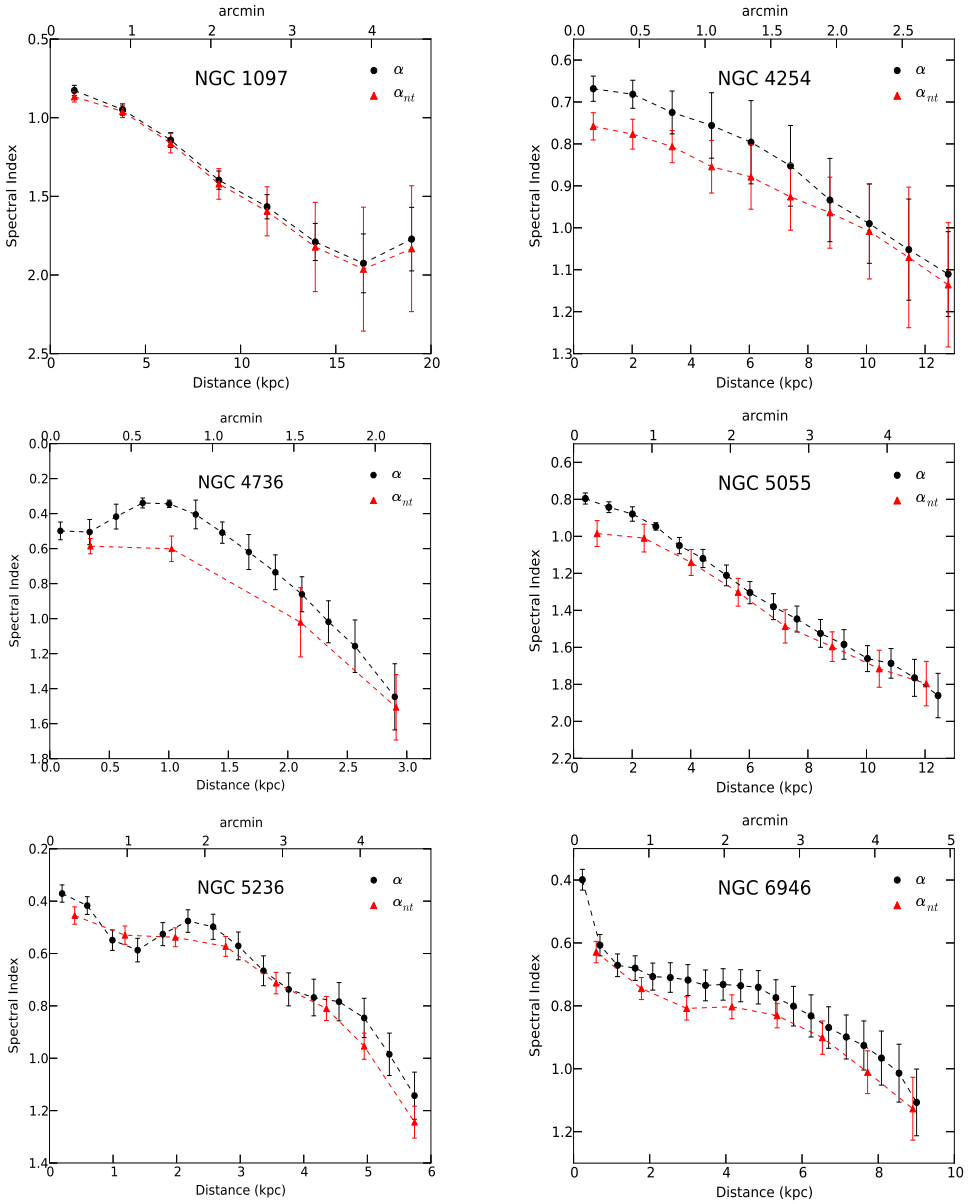

Figure 4.4: Azimuthally averaged spectral index determined within annuli of one beam width. The black circles are the total spectral index (α), while the red triangles are the nonthermal spectral index ($\alpha_{\rm nt}$). The top x-axis shows the angular distance from the center in arcmin.

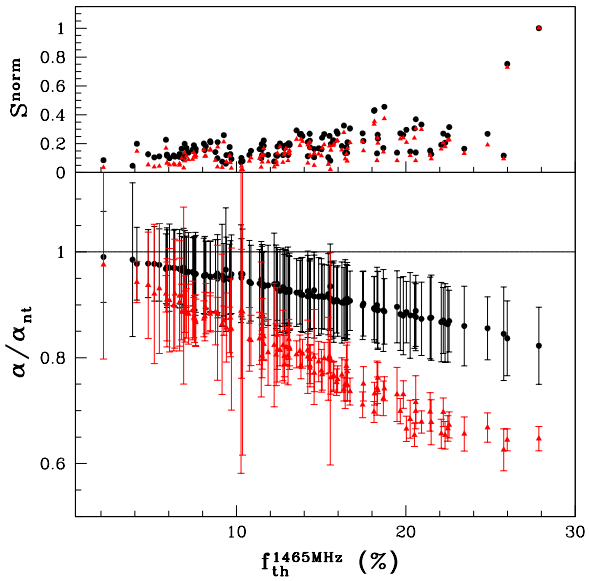

Figure 4.5: The bottom panel of the plot shows the ratio $\alpha/\alpha_{\rm nt}$ as a function of $f_{\rm th}$ at 1.465 GHz for NGC 6946 obtained at spatially resolved regions of the galaxy. The black circles corresponds to $\alpha/\alpha_{\rm nt}$ between 0.33 and 1.465 GHz, while the red triangles shows between 1.465 GHz and 4.86 GHz. The top panel shows the flux density normalized to the peak value at 0.33 GHz (in black) and 1.465 GHz (in red) respectively. Note that generally higher flux density regions have high thermal fractions.

over annuli of one beam width. The radial profiles clearly reveal that the nonthermal spectral index is nominally steeper than the uncorrected values, and further steepens towards the outer parts of the galaxy. However, we note that towards the outer parts of the galaxies, the steepening of both the total and nonthermal spectral indices may be caused due to 'missing flux density' problems (see Section 3.2.1).

We are now in a position to quantify the importance of thermal-nonthermal separation, for robust estimates of $\alpha_{\rm nt}$ between 0.33 GHz and near 1 GHz. The uncertainty in $\alpha_{\rm nt}$ can be estimated by propagating the various sources of errors in obtaining the nonthermal maps. Three primary sources of error affect the $\alpha_{\rm nt}$ measurement, namely: the rms in the two radio maps ($\sigma_{\nu,\rm map}$), the error associated with the uncalibrated system temperature of the instrument $\sigma_{\nu,\rm Tsys}$, and the error in thermal fraction, $\sigma_{\rm T}$. $\sigma_{\nu,\rm Tsys}$ is about 5 percent at 0.33 GHz for the GMRT and assumed about 2 percent for VLA and WSRT near or at 1.4 GHz maps. The error $\sigma_{\rm T}$ is estimated to be about 10 percent at these frequencies by Tabatabaei et al. (2007b) (also see Section 4.1). Incorporating these errors, we have computed the ratio $\alpha/\alpha_{\rm nt}$ in regions by dividing the galaxy into rectangular grids of size of approximately 40 arcsec. We find that for thermal fraction less that 5 percent at 0.33 GHz and less than about 10 percent near 1.4 GHz, $\alpha_{\rm nt} \sim \alpha$. This effect is illustrated for NGC 6946 in the bottom panel of Figure 4.5,

where the $\alpha/\alpha_{\rm nt}$ is plotted (in black) as a function of thermal fraction near 1.4 GHz. Within the error bars the ratio is consistent with unity for thermal fraction less than 10 percent. For higher thermal fraction (predominantly in the arms or HII regions) the ratio drops below unity, and correction to α, to obtain $\alpha_{\rm nt}$, could be as high as 20 percent. The thermal-nonthermal separation is even more important for $\alpha_{\rm nt}$ calculated between higher frequency pairs like 1.4 GHz and 4.8 GHz. The ratio $\alpha/\alpha_{\rm nt}$ for NGC 6946 obtained between 1.465 GHz and 4.86 GHz (using archival map downloaded from NED, Beck 2007) is plotted in red in Figure 4.5, where we clearly see that the ratio is significantly below unity for the whole range of thermal fractions. Note that since there is also a systematic uncertainty associated with the absolute calibration scale for calibrating radio flux densities, the absolute value of the spectral index can vary by about 10 percent.

4.3.1 $\alpha_{\rm nt}$ vs. gas density

The nonthermal spectral index is expected to change as the CRes propagate away from the sites of their generation due to energy losses. As discussed in Section 1.3.1, ionization loss can flatten $\alpha_{\rm nt}$ by 0.5 and can give rise to the $\alpha_{\rm nt} < 0.5$. Bremsstrahlung loss do not affect $\alpha_{\rm nt}$ and therefore $\alpha_{\rm nt}$ remains close to the value at which they are injected, i.e, 0.5–0.7. Synchrotron and inverse-Compton losses can steepen $\alpha_{\rm nt}$ by 0.5 and gives rise to $\alpha_{\rm nt} > 0.9$. Each loss mechanism have different timescales that determine the lifetime of CRes and thereby changing the value of $\alpha_{\rm nt}$. The ionization loss timescale ($\tau_{\rm ion}$) is given by,

$$\tau_{\rm ion} = 9.5 \times 10^6 \left(\frac{n}{\rm cm^{-3}}\right)^{-1} \left(\frac{E}{\rm GeV}\right) \quad {\rm yr} \tag{4.8}$$

Here, n is the gas density of the neutral medium and E is the energy of the CRes. The bremsstrahlung loss timescale ($\tau_{\rm brem}$) is given by,

$$\tau_{\rm brem} = 3.96 \times 10^7 \left(\frac{n}{\rm cm^{-3}}\right)^{-1} \quad {\rm yr} \tag{4.9}$$

And the synchrotron loss timescale ($\tau_{\rm syn}$) is given by,

$$\tau_{\rm syn} = 8.35 \times 10^9 \left(\frac{E}{\rm GeV}\right)^{-1} \left(\frac{B}{\mu\rm G}\right)^{-2} \quad {\rm yr} \tag{4.10}$$

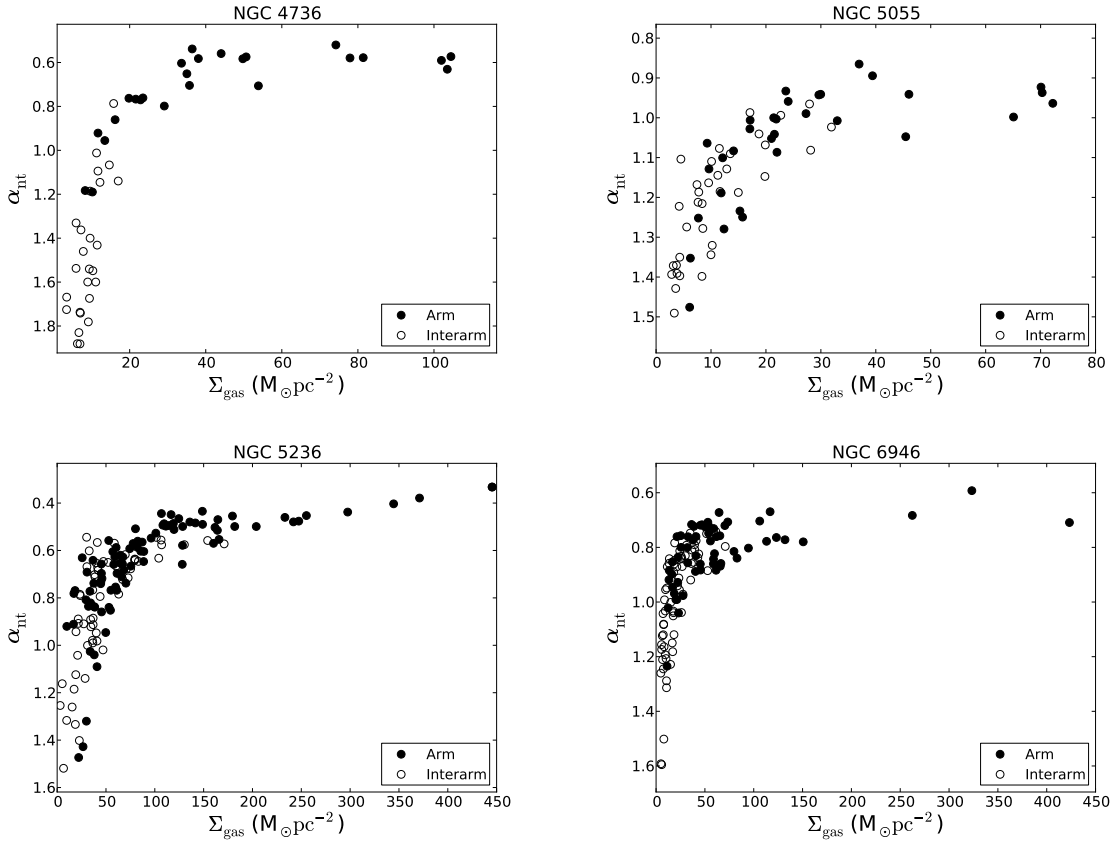

Figure 4.6: Variation of nonthermal spectral index (α_{nt}) with the total gas surface density (Σ_{gas}). The filled circles are for arms and unfilled circles are for interarm regions.

The CRe loss timescales depends on local gas density and magnetic field and thus value of α_{nt} indicates the dominant energy loss mechanism.

We study the variation of α_{nt} with the total gas surface mass density [$\Sigma_{gas} = 1.36(\Sigma_{H_I} + \Sigma_{H_2})$] in Figure 4.6 for four of the galaxies, NGC 4736, NGC 5055, NGC 5236 and NGC 6946. Here, Σ_{H_I} and Σ_{H_2} are the surface mass density of atomic and molecular gas respectively (see Appendix A) and the factor 1.36 is to account for helium. The solid circles are for arm regions while the open circles are for interarm regions. In arms, i.e., regions of higher gas density ($\gtrsim$ 50 $M_\odot pc^{-2}$), α_{nt} is found to flatten slightly with gas density and lie in the range 0.5 – 0.8 close to the value at which the CRes are injected. This perhaps could be caused due to ionisation losses of the CRes in denser ISM or due to young CRes that are freshly produced. Moreover, we note that the observed α_{nt} is produced from CRes with large distribution of ages and the average

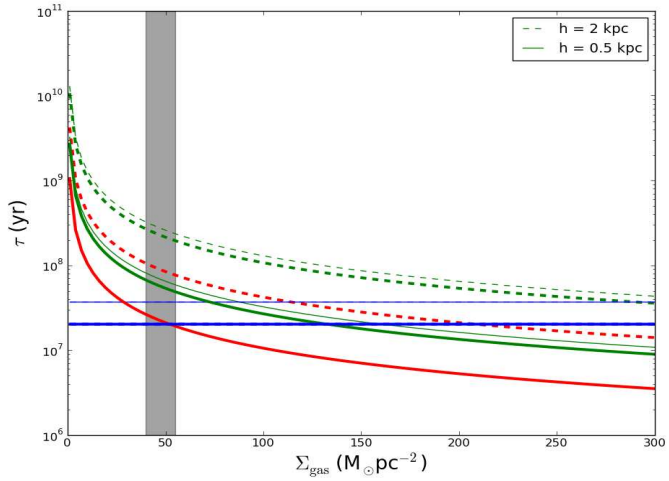

Figure 4.7: CRe energy loss timescales with total gas surface mass density. The blue, green and red curves are for synchrotron, ionization and bremsstrahlung loss timescales respectively. The dashed and solid curves are for neutral gas scale height of 2 and 0.5 kpc respectively. The thick and thin lines are for magnetic field strength of 15 and 10 μG respectively.

age increases with increasing distance from the source of their generation which requires detail modelling for complete interpretation of our results. In the interarm regions, i.e., regions of low gas surface density ($\lesssim$ 50 $M_{\odot}pc^{-2}$), $\alpha_{\rm nt}$ is seen to steepen sharply with $\alpha_{\rm nt} > 1$, indicating energy loss by synchrotron and/or inverse-Compton losses.

In Figure 4.7 we plot the timescales of bremsstrahlung (red curves), ionization (green curves) and synchrotron (blue lines) losses with gas surface density for typical magnetic field strengths of 10 μG (thin curves) and 15 μG (thick curves). The solid and dashed curves are for neutral gas scale height of 0.5 and 2 kpc respectively. The gas density (n) was computed from $\Sigma_{\rm gas}$ for the above mentioned scale heights. All the curves are drawn for CRes emitting at 1.4 GHz. For a typical scale height of 0.5 kpc, bremsstrahlung and ionization loss timescales are seen to dominate over the synchrotron loss timescale for surface mass densities above 40–55 $M_{\odot}pc^{-2}$ (marked as shaded region in Figure 4.7). In such regions $\alpha_{\rm nt}$ is expected to remain close to what is injected into the ISM or flatter. While for low gas density regions the synchrotron loss timescales are lower than that of ionization and bremsstrahlung timescales and the $\alpha_{\rm nt}$ is expected to be steeper than 1. Such a change of $\alpha_{\rm nt}$ is seen in Figure 4.6. To understand the absolute values of $\alpha_{\rm nt}$ in each regime a, detail model of ionization rates

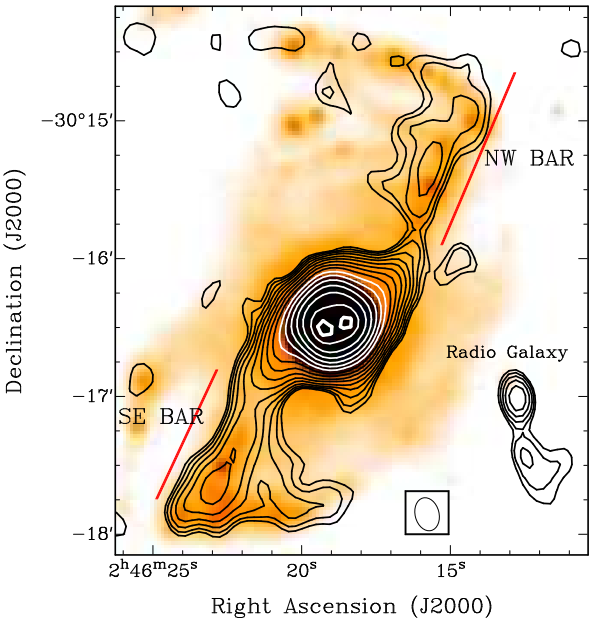

Figure 4.8: The bar in the galaxy NGC 1097. In shades of orange is the 24μm MIPS image (resolution $\sim$6″), overlaid is the high resolution 0.33 GHz map made using baselines more than 1 kiloλ with a resolution 14.5 × 10 arcsec^2. The contours start from 1 mJy, and subsequent contours are in multiples of $\sqrt{2}$. The highest intensity contour is at 150 mJy beam^{-1}.

and magnetic field in essential and would be considered in future work.

4.4 Discussion on Individual Galaxies

NGC 1097: Our 0.33 GHz map (see Figure 3.3) has an angular resolution of 16 × 11 arcsec^2, which corresponds to a spatial resolution of $\sim$ 1.1 kpc, if the galaxy is at a distance of 14 Mpc. The only other low frequency radio continuum study of this galaxy was done by Ondrechen & van der Hulst (1983), Ondrechen, van der Hulst & Hummel (1989) and Beck et al. (2005) at $\sim$ 1.465 GHz. They reported strong radio emission coincident with the narrow dust lanes in the bar. The central bar region is also clearly visible in our 0.33 GHz map, and is coincident with dust emission inferred from the far infra-red λ24μm images from *Spitzer*, as seen in Figure 4.8. The bar pattern rotates in the clockwise direction (see Ondrechen, van der Hulst & Hummel 1989), and as expected prominent shock fronts are visible on the leading side of the bar with respect to the sense of rotation. The $f_{\rm th}$ in the bar region at 0.33 GHz is estimated to be <1 percent, hence the radio emission at this frequency is entirely nonthermal in origin.

These observations fit well with the explanation that the radio emission from the bar results due to shock compression of gas, dust and magnetic field, as was concluded by Ondrechen & van der Hulst (1983). The total emission from the bar and the central component (the region shown in Figure 4.8) is 835±57 mJy, out of which 750±52 mJy arises from the central compact region (25×21 arcsec^2 in size). For a similar sized central region Ondrechen & van der Hulst (1983) quote a flux density of 260 mJy at 1.465 GHz, based on which we get a α of ~ 0.75 close to what is estimated by Beck et al. (2005). The $\alpha_{\rm nt}$ within a 40 arcsec region based on our analysis is 0.85 ± 0.1. This $\alpha_{\rm nt}$ close to the nuclear region is steeper when compared with other galaxies in our sample. This indicates possibility of radiative cooling by inverse Compton/synchrotron processes due to strong magnetic field up to 60 μG (Beck et al., 2005).

The southeastern (SE) side of the bar has a flux density of 50 ± 4 mJy and the northwestern (NW) side has a flux density of 30 ± 2 mJy, measured within the 2 mJy closed contours. The red lines in Figure 4.8 show the SE bar and NW bar. In the optical, the bar region continues into two prominent arms however the radio emission is highly diffuse. We find the thermal fraction of the interarm region at 0.33 and 1.465 GHz to be 0.2 percent and 2.5 percent respectively whereas in the spiral arm regions it is 1 percent and 4.5 percent respectively. In the arm regions, the $\langle\alpha_{\rm nt}\rangle$ is 1.4 ± 0.09 while it gets significantly steeper (1.8 ± 0.12) in the interarm regions which may be caused due to missing flux density problems. The radial profile of the α and $\alpha_{\rm nt}$ in Figure 4.4, gets steep towards the outer parts of the galaxy possibly due to missing flux density. We emphasize that the overall thermal fraction in this galaxy is very low, with $\langle f_{\rm th}\rangle$ of $\sim$0.6 percent at 0.33 GHz and $<$4.8 percent at 1.465 GHz (see Figure 4.1).

At 0.33 GHz, we detect the radio galaxy discovered by Beck et al. (2005), located $\sim$ 90 arcsec from the nucleus of NGC 1097 towards the southwest at a PA of $-110°$ (see Figure 4.8). The radio galaxy has a total flux density of 9.5 ± 0.5 mJy, with 4.8 ± 0.25 mJy in the northern component [RA = 02h46m12.7s, dec = $-$30d17′01″ (J2000)] and 3.8 ± 0.2 mJy in the southern component [RA = 02h46m12.5s, dec = $-$30d17′26.6″ (J2000)].

NGC 3034 (M82): The 0.33 GHz map (see Figure 3.3) of this galaxy has an angular resolution of 22×15 arcsec^2, corresponding to a spatial resolution of about 0.5 kpc for a distance of 3.9 Mpc. We find the integrated flux density at 0.33 GHz to be 14 Jy which is consistent with flux densities measured at other frequencies. The rms of the image, which is 3 mJy beam^{-1}, is dynamic range limited since the peak flux density in the galaxy is 3 Jy beam^{-1}. Morphologically the galaxy is featureless at

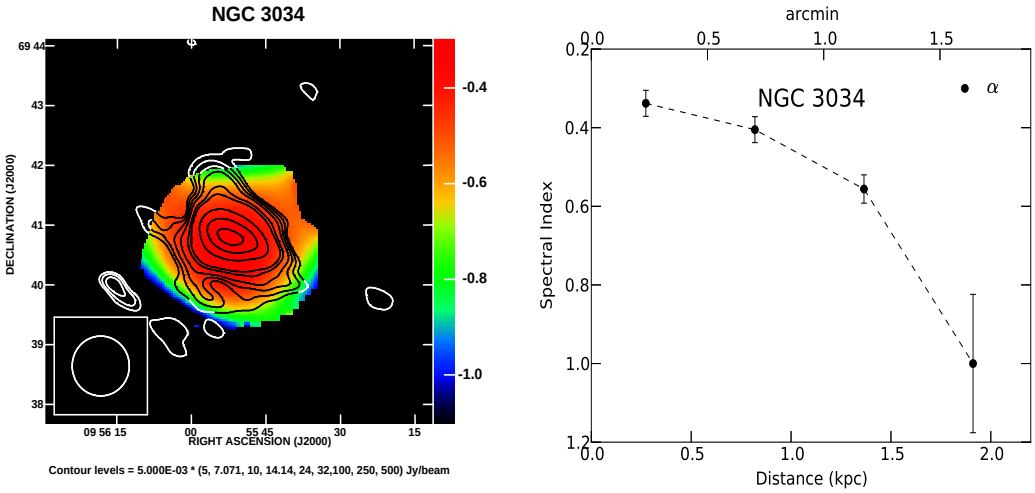

Figure 4.9: Left-hand panel: Total spectral index map of the galaxy NGC 3034 at an angular resolution of 60×60 arcsec^2. Overlaid is the 0.33 GHz total intensity contour. Right-hand panel: The azimuthally averaged total spectral index profile of NGC 3034. The averaging was done for half the synthesized beam and therefore adjacent points are not independent. The nonthermal spectral index map was not possible for this galaxy (see text for details).

our resolution, although the northern extension [RA = 09h55m56s, dec = +69d41′48″ (J2000)] is coincident with the base of the Hα/optical horn (see Figure 3.3), which is likely due to synchrotron emitting particles convected outwards by the nuclear wind, tracing the Hα horns. The galaxy was observed between 0.33 GHz to 4.835 GHz by Seaquist & Odegard (1991), and a similar horn was seen at ∼1.515 GHz. Their study also revealed a nonthermal radio halo surrounding the galaxy, however our observations do not show this due to dynamic range limitations.

For this galaxy, the thermal-nonthermal separation was not possible, due to nonlinearity and streaking effects in the $\lambda 160\mu$m MIPS image. However, we have computed the α map and radial profile as shown in Figure 4.9. The 0.33 GHz GMRT map was convolved to the resolution of VLA map at 60 arcsec. This is a good approximation for $\alpha_{\rm nt}$ index variation across the galaxy since the thermal fraction of this galaxy has been estimated to be 15 percent at 32 GHz (Klein, Wielebinski & Morsi, 1988), corresponding to $\sim$ 3 and 2 percent at 1.4 GHz and 0.33 GHz respectively. The spectral index is seen to be very flat with $\alpha = 0.35 \pm 0.03$ towards the center and steepens to 1 ± 0.2 at a distance of ∼2 kpc from the center. Similar radial variation of the spectral index was also reported by Seaquist & Odegard (1991) and recently by Adebahr et al. (2012).

NGC 4254 (M99): The 0.32 GHz observation of NGC 4254 has an angular resolution of 13×11 arcsec^2 (see Figure 3.3) corresponding to spatial resolution of ∼

0.9 kpc at a distance of $\sim$ 15.4 Mpc. This galaxy has been studied at 0.325 GHz by Kantharia, Rao & Sirothia (2008) using the GMRT, however their resolution was limited to 34×20 arcsec^2 and their map rms noise was 1.6 mJy beam^{-1} which is $\sim$5 times higher than our map (see Table 3.2). At our resolution and sensitivity we clearly detect diffuse extended structure in the north of this galaxy. The southern arm is seen to extend to the north due to tidal interactions. The southern arm has a linear angular size of $\sim$ 7 arcmin, i.e., $\sim$ 30 kpc and is extended well beyond the optical extent of the galaxy in that direction at 2σ level. Moreover, in the radio emission is seen to have a sharp edge in the souther side of the galaxy and is diffuse towards the north. The northern diffuse emission is more than 1.5 times in extend than that in the southern side perhaps caused due to Virgo infall. Such an asymmetry is also seen in high frequency radio continuum maps at 4.86 and 8.46 GHz (Chyży, Ehle & Beck, 2007). The degree of polarization in the southern region is up to 40 percent polarized with mean of $\sim$ 24 percent (Chyży, Ehle & Beck, 2007). This could be caused by shock compression due to Virgo infall. The nonthermal spectral index in the compressed region is $\sim$ 0.85 and is comparatively steeper than the disc where $\alpha_{\rm nt} \sim 0.7$.

The mean thermal fraction in the disc of this galaxy at 0.32 GHz and 1.465 GHz is found to be $\sim$ 3.5 and $\sim$ 8 percent respectively. At 8.46 GHz, Chyży, Ehle & Beck (2007) estimated the thermal fraction to be $\sim$ 20 percent, which at 1.465 GHz corresponds to $\sim$ 5 percent. Their estimates are lower than that our estimated value. This is perhaps caused due to their use of a constant nonthermal spectral index of 1 throughout the galaxy. The emission in the northern diffuse region and the extended southern arm is almost entirely nonthermal at both the frequencies and $\alpha_{\rm nt}$ is generally steeper in that region and lies in the range $\sim 1 - 1.4$.

NGC 4736 (M94): The 0.33 GHz map (see Figure 3.3) of this galaxy has an angular resolution of 13×12 arcsec^2, corresponding to a spatial scale of about 0.3 kpc for a distance of 4.7 Mpc. The other low frequency study of this galaxy exist at 0.61 GHz (de Bruyn, 1977), observed with much lower angular resolution of 56×85 arcsec^2. At our angular resolution we clearly detect emission from the inner star forming circumnuclear ring of the galaxy as shown in Figure 4.10 overlaid on the Hα map convolved to the same radio resolution . The ring is located at about 50 arcsec (major axis), corresponding to 1.1 kpc, from the center, and is $\sim$19 arcsec (420 pc) wide (up to the half power) having a flux density of 240$\pm$13 mJy. The estimated thermal fraction of the ring at 0.33 GHz and 1.375 GHz is 5 ± 1 and 10 ± 4 percent respectively, and hence the ring at 0.33 GHz is largely nonthermal in origin.

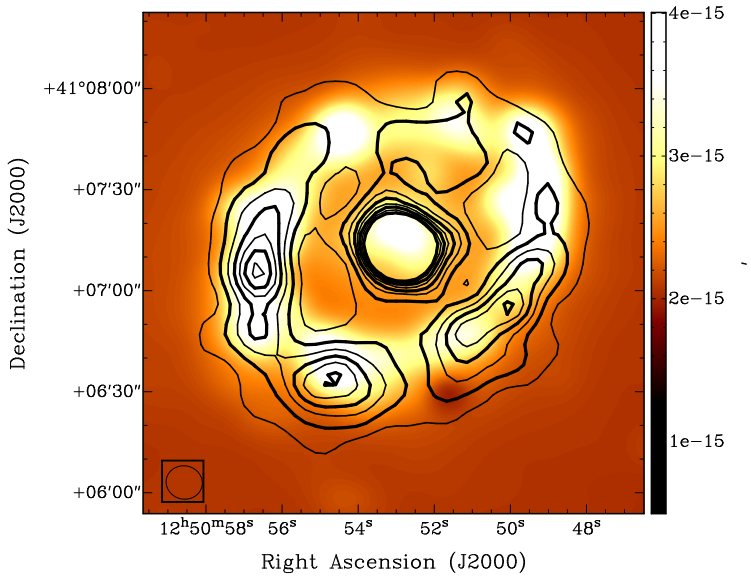

Figure 4.10: The star forming inner circumnuclear ring in NGC 4736. The contours are the high resolution 0.33 GHz GMRT map with synthesized beam of 10.8×9.9 arcsec^2 and the grey scale shows the Hα image (in erg s^{-1}cm^{-2}) from the Jacobi Kapteyn Telescope with the 6570Å filter (Knapen et al., 2004), smoothed to the same resolution as the 0.33 GHz map. The lowest contour is at 3 mJy increasing in steps of 1 mJy.

Radio emission from the ring is also seen in the higher frequency 8.46 GHz observations made by Chyży & Buta (2008), however at these frequencies the emission is a mixture of thermal and nonthermal components. The ring has relatively high thermal fraction which leads to a noticeable change in spectral index (see Figure 4.4) such that $\langle\alpha\rangle$ is 0.45 ± 0.02, while the $\langle\alpha_{\rm nt}\rangle$ is 0.6 ± 0.1. The ring has massive on going star formation (Smith et al., 1991) and $\alpha_{\rm nt}$ value indicates that both CRe generation and escape happens on timescales shorter than the radiative timescale. The compact nucleus lies within the central 0.5 kpc (25×22 arcsec^2) with integrated flux density of 110±6 mJy and a peak flux of 45 mJy beam^{-1} and $\alpha_{\rm nt} = 0.6 \pm 0.05$. Outside the ring extending to the edge of the galaxy there is no thermal emission observed leading to $\alpha_{\rm nt} \sim \alpha$.

NGC 5055 (M63): The 0.33 GHz observation (see Figure 3.3) has an angular resolution of 17×10 arcsec^2 corresponding to a spatial scale of 0.7 kpc at a distance of 9 Mpc. As is evident from the figure, the extent of the galaxy is larger at 0.33 GHz than the optical. In an earlier study by Hummel & Bosma (1982) at 0.61 GHz and 1.41 GHz at much lower angular resolution of 58×87 arcsec^2, the galaxy appears featureless which is also the case in our higher resolution 0.33 GHz map. However, 10.55 GHz

polarization observations by Knapik et al. (2000) show regular spiral structure. The overall radio emission at 0.33 GHz at a level of 4σ is $\sim$8.6×5.3 arcmin^2 in extent, which has an integrated flux density of 2.3±0.13 Jy. This value is higher than what one would obtain using a spectral index of 0.78 estimated between 0.61 and 1.417 GHz (Hummel & Bosma, 1982). The reason for this is Hummel & Bosma (1982) estimate the integrated flux density within a region 6.7×3.2 arcmin^2 at 0.61 GHz, which is smaller than our detected size at 0.33 GHz. However, if a similar size region is considered, we obtain a flux density of 1.4±0.1 Jy which is consistent with a spectral index of 0.78 as seen in Figure 3.4. NGC 5055 is highly inclined, with inclination angle $i = 59°$, and the extended low frequency radio emission can result due to escape of low energy ($<$ 2 GeV) CRes from the disc which travel larger distances ($\sim$ 4.5 kpc) into the galactic halo.

The mean thermal fraction $\langle f_{\rm th} \rangle$ at 1.7 GHz (λ18cm) and 0.33 GHz is 12 and 1.3 percent respectively. The $\alpha_{\rm nt}$ in the central region is $\sim$ 1 which steepens to 1.7 towards the outer parts of the galaxy[1] (see Figure 4.4). This result supports the conclusion drawn by Hummel & Bosma (1982) that the spectral index steepening is mainly due to energy losses of CRes and decrease in number of higher energy relativistic electrons at higher radio frequencies with increasing galactic radius.

NGC 5236 (M83): The 0.33 GHz observation (see Figure 3.3) has an angular resolution of 16×12 arcsec^2, which correspond to a linear scale of about 0.4 kpc at a distance of 4.2 Mpc. An early study of this galaxy by Sukumar, Klein & Graeve (1987) at 0.327 GHz using the Ooty Synthesis Radio Telescope (OSRT) quotes integrated flux density of 6.86±0.62 Jy at a resolution of 53×33 arcsec^2, while our GMRT observations has a slightly higher integrated flux density of 7.4±0.4 Jy.

Ondrechen (1985) has reported several point sources in this galaxy. To verify the presence of these sources at 0.33 GHz, we made a high resolution image of 13×10 arcsec^2 using Briggs' robust weighting of -1 and is shown in Figure 4.11. Comparing this with Ondrechen (1985) we detect the central bar (shown in red lines) and the HII regions named as A, F, H and I, and nonthermal polarized point sources D, G and X. Note that source G is identified as a background galaxy by Maddox et al. (2006). The region E

[1]Note that Hummel & Bosma (1982) using observations at 0.61 and 1.417 GHz quote a spectral index variation of 0.6 to 1 between the central and outer parts of the galaxy, while we find much steeper values. The WSRT 1.7 GHz map has a flux density of 284 mJy within the same region of 6.7×3.2 arcmin^2, which when extrapolated using a spectral index of 0.78, has a much lower value (see Figure 3.4). This may be due to missing flux density issues as discussed in Section 3.2.1. Thus the true spectral index should be flatter than what is observed by us.

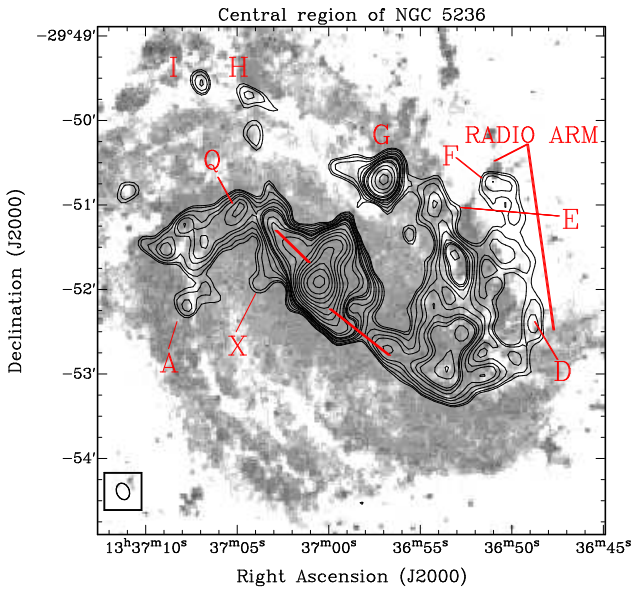

Figure 4.11: The central region in NGC 5236. Grayscale is the DSS image at a resolution of 1″, overlaid are the 0.33 GHz contours at resolution 13×10 arcsec^2. The marked regions are as per Ondrechen (1985). The flux densities of the sources are as follows; A : 12.3 ± 0.7 mJy, D : 11.5 ± 0.7 mJy, F : 13.5 ± 0.8 mJy, G : 55 ± 3 mJy, H : 10.2 ± 0.6 mJy, I : 9.2 ± 0.5, X : 20.0 ± 1.2 mJy

was identified as a shocked region in the arm, and has a flux density of 33 ± 2 mJy, while the point source Q is a HII region and has flux density of 5 mJy beam^{-1}. However, we were unable to detect point sources B and C. The flux densities of the point sources are given in Figure 4.11. In addition to this we see an extended radio arm, which runs along the faint narrow dust lane visible in the infrared $\lambda 70 \mu$m map.

The galaxy has a low mean thermal fraction of about 3 percent at 0.33 GHz and about 7 percent at 1.452 GHz, and hence $\alpha_{\rm nt} \sim \alpha$ as seen in the radial spectral index profile of the galaxy in Figure 4.4. In the arms, at 0.33 GHz, the thermal fraction is estimated to be $8 - 10$ percent, where α ranges from 0.3 ± 0.04 to 0.5 ± 0.05 which gets modified to $\alpha_{\rm nt}$ as 0.4 ± 0.05 to 0.65 ± 0.05. $\alpha_{\rm nt}$ along the arms is seen to change significantly from 0.4 within the central 3 kpc to 0.65 beyond 3 kpc. Thermal fraction at 0.33 GHz in the interarm regions is $1 - 4\%$ and beyond the central 4.5 kpc is less than 1 percent, indicating purely nonthermal emission. In the interarm regions, $\alpha_{\rm nt}$ values lie in the range 0.7 ± 0.06 to 1.2 ± 0.09.

NGC 6946: The 0.33 GHz observation (see Figure 3.3) has an angular resolution of 12×11 arcsec^2 which corresponds to a spatial resolution of 0.4 kpc at a galaxy distance of 6.8 Mpc. The integrated flux density at 0.33 GHz is 4.5 ± 0.24 Jy. Using our 0.33

GHz and archival 1.465 GHz VLA maps, we estimate the mean thermal fraction to be about 4.3 and 11 percent respectively.

Spectral index study by Klein et al. (1982) between 0.61 and 10.7 GHz showed variation from about 0.55 near the center to about 0.9 towards the edge. The spectral index between GMRT 0.33 GHz map and VLA 1.465 GHz map shows a similar trend, with spectral index of 0.45 at the center and 1 towards the edge. Recently, Beck (2007) studied the spectral index between 4.86 GHz and 1.465 GHz which showed flatter spectral index in the arm than the interarm due to higher thermal fraction. In our studies, thermal fraction is higher in the arm (5–10 percent) than in the interarm (1–5 percent). In the arm, α lies in the range 0.55 to 0.65, while the $\alpha_{\rm nt}$ is steeper 0.7 to 0.85. In the interarm regions the average spectral index is steeper with $\langle\alpha\rangle = 0.9 \pm 0.06$, while the $\alpha_{\rm nt}$ does not change significantly, $\langle\alpha_{\rm nt}\rangle = 0.95 \pm 0.11$.

The 0.33 GHz map prominently shows the giant HII regions identified by van der Kruit, Allen & Rots (1977). The HII region at RA = 20h35m06s, dec = +60d10′56″ (J2000) (region C in van der Kruit, Allen & Rots (1977)), is about 35 arcsec (1.2 kpc) in size, and can be seen in the 40 arcsec low resolution nonthermal maps. This region is a suitable candidate to investigate the CRe injection near high star forming sites. We find the thermal fraction to be 10 ± 3 percent at 0.33 GHz and 15 ± 4 percent at 1.465 GHz. The $\alpha_{\rm nt}$ in this region is 0.6 ± 0.08, whereas before the separation the spectral index was 0.4 ± 0.05.

The central 35 arcsec region [at RA = 20h34m52s, dec = +60d09′14″ (J2000)] has a flux density of 226±13 mJy at 0.33 GHz while at 1.465 GHz the same region has a flux density of 117±6 mJy. This corresponds to an α of 0.44 ± 0.05 at a resolution of 15×15 arcsec^2. However, after the separation, similar region has a $\alpha_{\rm nt}$ of 0.54 ± 0.1 (see Figure 4.3). In the nuclear region about 15 percent of the total emission is due to thermal emission at 0.33 GHz, higher than the rest of the galaxy, where the thermal emission lies within 10 percent.

4.5 Discussion

We have determined robust estimates of spatially resolved $\alpha_{\rm nt}$ (see Section 4.3) for six galaxies in our sample, with a resolution of 40 arcsec, corresponding to a linear scale of 1–3 kpc, which also corresponds to the diffusion scale of the CRes. We have also determined $\alpha_{\rm nt}$ using a new method by combining Hα and λ24 μm as the tracer

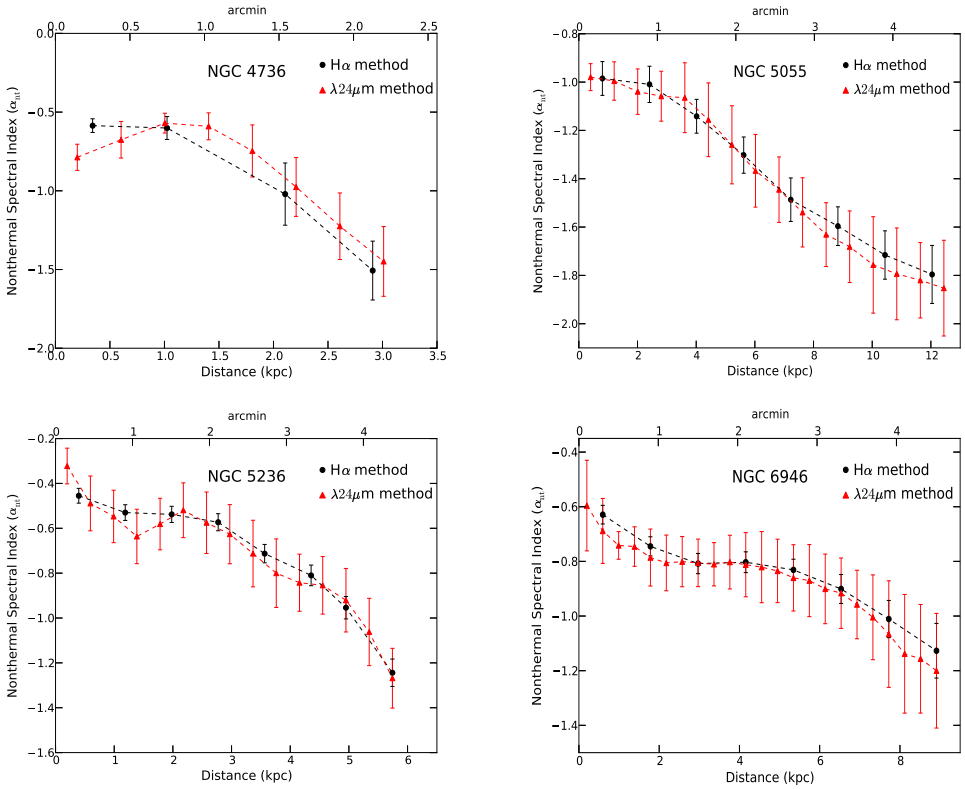

Figure 4.12: Azimuthally averaged nonthermal spectral index ($\alpha_{\rm nt}$) determined within annuli of one beam width. The black circles are $\alpha_{\rm nt}$ determined using Hα as tracer of thermal emission and the red triangles are $\alpha_{\rm nt}$ determined using the corrected λ24-μm method. The top x-axis shows the angular distance from the center in arcmin.

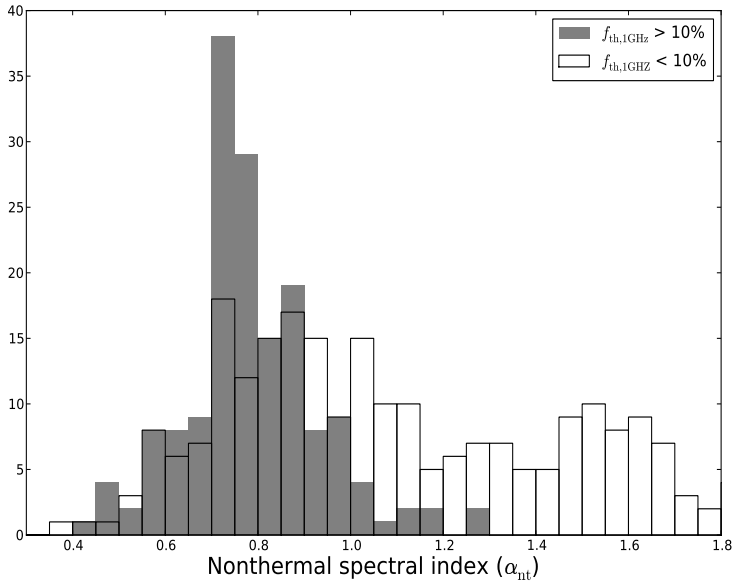

Figure 4.13: Histogram of nonthermal spectral index for five galaxies for two range of thermal fractions. The filled grey histogram corresponds to thermal fraction $f_{\rm th,1GHz} >$ 10 percent and the unfilled histogram is for $f_{\rm th,1GHz} < 10$ percent.

of thermal component of the emission at sub-kpc scales (Section 4.2). Figure 4.12 shows the radial profile of the nonthermal spectral index ($\alpha_{\rm nt}$) averaged within annuli of one beam width for the two methods. The black circles and red triangles are for Hα and λ24-μm as the tracer of thermal emission. Due to poorer resolution of the nonthermal maps obtained using Hα-method, the annuli are 40 arcsec wide while for $\lambda 24\mu$m-method the annuli are $\sim 15 - 20$ arcsec wide. $\alpha_{\rm nt}$ obtained using the two methods agree well within the errorbars. The observed $\alpha_{\rm nt}$ ranges from 0.3 to 1.8 in various regions of the galaxies. Generally CRes are thought to be accelerated at SNR where both the theoretical prediction (Bell, 1978) and observation based on Galactic SNR suggest mean $\alpha_{\rm nt} \sim 0.5$ (Green, 2009; Kothes et al., 2006). The SNR are short lived ($\sim 10^5$ yrs), while the CRes diffuse away from their acceleration sites losing their energy through several physical mechanisms for typically 10^8 yrs, and hence their initial energy spectrum gets distorted leading to a change in $\alpha_{\rm nt}$. If the energy losses are due to ionization, $\alpha_{\rm nt}$ flattens (Longair, 2011). Synchrotron radiation and inverse Compton scattering loss leads to a steepening of the spectra, while adiabatic cooling and bremsstrahlung keep the spectra unchanged. Here we discuss the variation of $\alpha_{\rm nt}$ at 40 arcsec resolution determined using Hα method of separating the thermal component of the radio emission. To assess the behaviour of $\alpha_{\rm nt}$ in spatially resolved parts of

the galaxy we plot $\alpha_{\rm nt}$ distribution (as shown in Figure 4.13) for two regimes of thermal fraction: $f_{\rm th,1GHz} > 10$ percent (filled grey histogram) and $f_{\rm th,1GHz} < 10$ percent (unfilled histogram), using data from five galaxies[1]. To do this, we have computed $\alpha_{\rm nt}$ by dividing the galaxy in rectangular grids of 40 arcsec. The histograms are binned with step size 0.05 in $\alpha_{\rm nt}$. The high thermal fraction corresponds to bright regions in Hα which traces gas ionized by massive OB stars in star forming regions. The distribution of $\alpha_{\rm nt}$ for such high thermal fraction regions has a Gaussian shape, with mean $\alpha_{\rm nt} \sim 0.79$ and narrow spread of 0.15. It is interesting that this narrow distribution arises from multiple spatially resolved regions from an assorted set of galaxies with very different star formation histories. This is clearly indicative of a generic process of energy loss of CRes by synchrotron radiation and inverse Compton scattering as they propagate from their acceleration sites. The flatter part of $\alpha_{\rm nt}$ (< 0.55) primarily arises from NGC 5236, indicating that ionization losses are dominant (Longair, 2011). Niklas, Klein & Wielebinski (1997), based on integrated flux density of 74 galaxies found the average $\alpha_{\rm nt} \sim 0.83$ which is comparable to the $\alpha_{\rm nt}$ value that we have obtained. The galaxy integrated spectral index is an average over tens of kpc where the flux density is highly dominated by bright regions which are mostly spiral arms or HII regions. Our analysis shows that the contribution to the average spectral index primarily arises at least on kpc scales.

The unfilled histogram, corresponding to low thermal fraction ($f_{\rm th,1GHz} < 10$ percent) regions have a much larger spread with $\alpha_{\rm nt}$ lying in the range 0.4 – 1.8. The steepening in the range 1 – 1.3 arises from the interarm regions, and indicates energy losses through synchrotron emission and inverse Compton scattering. $\alpha_{\rm nt} > 1.3$, is mostly from low flux density regions, primarily in the outer parts of the galaxies, and may be affected due to missing flux density in the higher radio frequency maps. Note that we have averaged in a region 40 arcsec, which for all these galaxies corresponds to $\sim$ 1 kpc to 3 kpc, and hence the flatter part of $\alpha_{\rm nt}$ distribution may be affected due to bright regions. Note that, as pointed out in Section 4.1, the uncertainty in the thermal fraction at 0.33 GHz and near 1 GHz is $\sim$ 10 and $\sim$ 15 per cent respectively, which would give rise to a few per cent error in the values of the estimated $\alpha_{\rm nt}$. This would not change the distribution of $\alpha_{\rm nt}$ significantly.

In Figure 4.14 we study the distribution of the nonthermal spectral index at a higher spatial resolution of 0.4–1.5 kpc determined using the new method of separation

[1]We did not use NGC 5055, since we think that there is a missing flux density problem at 1.7 GHz and hence the derived α and $\alpha_{\rm nt}$ might be steeper than the actual value.

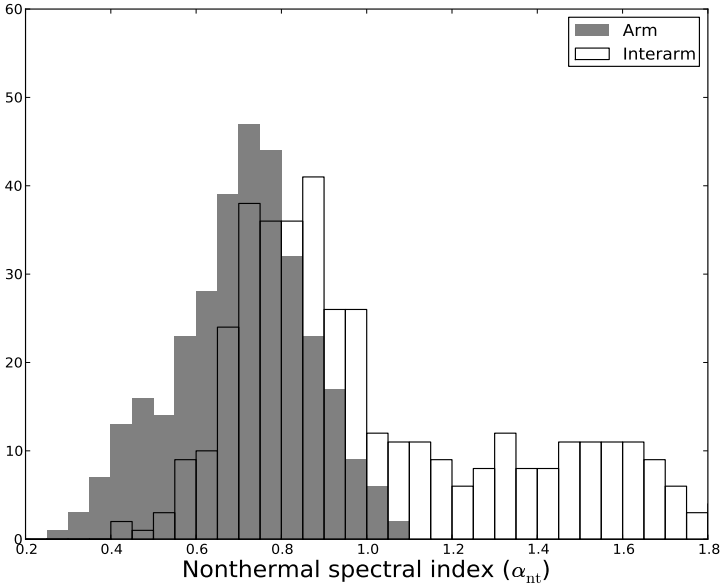

Figure 4.14: Distribution of nonthermal spectral index at sub-kpc spatial resolution determined using the new method of separation of thermal emission (see Section 4.2). The filled and unfilled histograms shows the distribution in the arm and the interarm regions respectively.

of the thermal component (Section 4.2) for five galaxies (except NGC 5055). The filled and unfilled histrograms shows the distribution of $\alpha_{\rm nt}$ for arm and interarm regions respectively. In the arm regions, i.e., regions of higher thermal fraction, the distribution of $\alpha_{\rm nt}$ peaks at 0.75 with dispersion of 0.2. The peak is slightly flatter than that observed at spatial scales $\gtrsim 1$ kpc, however, the distribution is significantly wider and has a tail towards the flatter part of $\alpha_{\rm nt}$. The peak at ~ 0.5 mainly originate from the galaxy NGC 5236. In the interarm regions, i.e., regions of low thermal fraction, $\alpha_{\rm nt}$ has a wider distribution in the range 0.6–1.8. Note that, due to higher resolution the brigher parts of the galaxies perhaps do not affect the nonthermal spectral index significantly unlike in the previous case. The distribution of $\alpha_{\rm nt}$ at sub-kpc scales is similar to what is seen at larger spatial scales of 1–3 kpc. This demonstrates that the two methods of separating the thermal emission gives similar results.

As mentioned earlier, the absolute value of $\alpha_{\rm nt}$ can change by $\sim$10 percent due to uncertainty in flux scale at 0.33 GHz. A recent study by Paladino, Murgia & Orrú (2009) for NGC 0628, NGC 3627 and NGC 7331, using infrared emission ($\lambda 70\mu$m) as a tracer of star forming regions, found that α obtained using VLA observations at 0.325 GHz and near 1.4 GHz, is flatter for infrared bright regions. This is similar to what

we observe in our set of galaxies. The high angular resolution 0.33 GHz observations presented in this paper can be used to study in detail the spatially resolved radio–FIR correlation, which is presented in Chapter 5.

Chapter 5

Low frequency radio–FIR correlation at ~ 1 kpc scales

The radio–far infrared (FIR) correlation in normal galaxies was first observed by van der Kruit (1971, 1973) and later extended to a larger sample by the IRAS mission. Subsequently it was established that the correlation holds good (within a factor of 2) on global scales over five orders of magnitude in radio and FIR luminosity (Condon, 1992; Yun, Reddy & Condon, 2001) for a wide morphological class of galaxies like, spirals, irregulars and dwarfs (Dressel, 1988; Price & Duric, 1992; Wunderlich, Wielebinski & Klein, 1987). Based on spatially resolved studies of normal and irregular galaxies it is seen that the correlation holds even at scales of few tens to hundreds of parsecs (see e.g Beck & Golla, 1988; Dumas et al., 2011; Hoernes, Berkhuijsen & Xu, 1998; Hughes et al., 2006; Murgia et al., 2005; Murphy et al., 2006; Paladino et al., 2006; Paladino, Murgia & Orrú, 2009; Tabatabaei et al., 2007a; Xu et al., 1992).

The basic mechanism that connects these two regimes of emission is via star formation (Harwit & Pacini, 1975). The radio continuum emission arises due to synchrotron emission from relativistic electrons, produced in supernova remnants, a good fraction of which results from massive ($\gtrsim 10$ M$_\odot$) short lived ($\lesssim 10^6$ yr) stars. The FIR emission arises from re-radiation by dust heated due to ultra violet photons emitted by the above population of stars. Though the cause of the correlation is well understood, the tightness over several orders of magnitude is still a mystery. Many models explaining the correlation require close coupling between the magnetic field (B) and the gas density ($\rho_{\rm gas}$) of the form, $B \propto \rho_{\rm gas}^{\kappa}$ (discussed in Section 2.3.2; also see e.g., Helou & Bicay, 1993; Niklas & Beck, 1997; Thompson et al., 2006). Such a coupling can be established

by magnetohydrodynamic (MHD) turbulence of the ISM (see Chandrasekhar & Fermi, 1953; Cho, Lazarian & Vishniac, 2003; Cho & Vishniac, 2000; Groves et al., 2003, discussed in Chapter 1). Numerical simulations by Cho & Vishniac (2000) revealed that $\kappa = 0.5$ is a manifestation of the equipartition condition, i.e, in steady MHD turbulence the magnetic field energy density and the energy density of the gas are similar. Similar values of κ have been derived from observations of magnetic field by Zeeman splitting in molecular clouds by Crutcher (1999), using equipartition magnetic field and molecular gas density observations in external galaxies (Niklas & Beck, 1997) and in the Milky Way and M31 (Berkhuijsen & et al., 1997). Alternatively, the slope of the radio–FIR correlation has been used to estimate κ, where $\kappa \sim 0.4$–0.6 (Dumas et al., 2011; Hoernes, Berkhuijsen & Xu, 1998; Niklas & Beck, 1997).

The spatially resolved and global studies of the radio–FIR correlation have been carried out primarily using radio emission at 1.4 GHz and higher frequencies. The only low frequency study at 150 MHz (Cox et al., 1988) confirms that on global scales the radio–FIR correlation holds good and is similar to what is seen at 1.4 GHz. As per our understanding, no low frequency (< 1.4 GHz, such as 0.33 GHz) spatially resolved study of the radio–FIR correlation exists in the literature. The motivation for such a studies arise from the fact that at lower frequencies the emission is largely nonthermal which is better at exhibiting the relation between magnetic field and star formation. Additionally, since the cosmic ray electrons (CRe) propagate larger distances in the galaxies at lower frequencies, it is important to assess how that affects the form of the radio–FIR correlation.

In this chapter, we present spatially resolved study of the radio–FIR correlation for six normal galaxies, NGC 1097, NGC 4254, NGC 4736, NGC 5055, NGC 5236 and NGC 6946 at spatial resolution of $\sim$1–2.8 kpc with radio observations at 0.33 GHz (λ90 cm) and 1.4 GHz (λ20 cm). We also estimate the value of κ and verify the assumptions of equipartition of energy. In Section 5.1 we discuss the various sources of maps used in this work and also define the parameter 'q' which is used to quantify the correlation. In Section 5.2 we present our results on spatially resolved radio–FIR correlation using far infrared emission at λ70 μm and radio emission at λ20 cm and λ90 cm. We discuss our results in Section 5.3.

5.1 Data analysis

The six galaxies used for our studies are selected from the observations presented in Chapter 3. The large angular sizes of the galaxies ensured enough independent regions to carry out this spatially resolved study. Our sample comprises of the galaxies NGC 1097, NGC 4254, NGC 4736, NGC 5055, NGC 5236 and NGC 6946. Table 3.1 summarizes the salient features of our sample and the various sources of archival data.

To study the radio–FIR correlation using nonthermal radio emission a thorough separation of thermal component of radio emission is needed. We derived nonthermal radio continuum maps at λ90 cm and λ20 cm after subtracting the thermal free–free component mainly originating from HII regions in recent star formation sites. The thermal emission was estimated using the prescription of Tabatabaei et al. (2007b), wherein, the dust extinction-corrected Hα map is used as a template for the thermal free-free emission. This is then extrapolated to the desired radio frequency and subtracted from the total emission map. Details of observation and data analysis are discussed in Chapter 3 and 4. The λ90 cm maps were obtained using the Giant Meterwave Radio Telescope (GMRT) while the λ20 cm maps were obtained using data from various archives (see Table 3.1). The nonthermal maps have 40 arcsec resolution with 9 arcsec pixel size. We scaled the flux of each galaxy to a common reference frequency of 1.4 GHz using the spectral index map obtained from the 0.33 GHz and near 1 GHz images for each pixel.

The galaxies were observed in the far-infrared by the *Spitzer space telescope* at λ70 μm as a part of the *Spitzer* Infrared Nearby Galaxy Survey (SINGS; Kennicutt et al. 2003) using the Multiband Imaging Photometer for *Spitzer* (MIPS; Rieke et al. 2004). The images were obtained from the publicly available database of SINGS Data Release 5[1]. These images had a pixel size of 4.5 arcsec and a point spread function (PSF) of about 16 arcsec. They were convolved to the resolution of nonthermal radio maps (40 arcsec) and re-gridded to a pixel size of 9 arcsec and the maps were aligned to the same coordinate system.

For the present study, the flux density per beam for the radio and FIR maps were determined within $\sim$ 40 arcsec diameter, with the adjacent region being about one beam away to ensure independence. Pixels with brightness above 2σ (σ is the *rms* noise in the map) were considered for the analysis. We estimated the slope of the radio–FIR correlation and the quantity 'q' introduced by Helou, Soifer & Rowan-Robinson (1985).

[1]http://data.spitzer.caltech.edu/popular/sings/

Figure 5.1: Overlay of ∼40 arcsec beams (marked in circles) on the Hα images[a] smoothed to 40 arcsec. The top and lower panels shows the arm and the interarm regions respectively (see Section 3 for details). [a]The images were downloaded from the NED for the galaxies NGC 4736 (1-m Jacobus Kapteyn Telescope (JKT) at La Palma with filter Ha6570; Knapen et al., 2004), NGC 5055 (2.3-m telescope at KPNO, filter: 6580) and NGC 5236 (0.9-m telescope at CTIO, filter: 6563). For NGC 6946 the image was downloaded from the SINGS website.

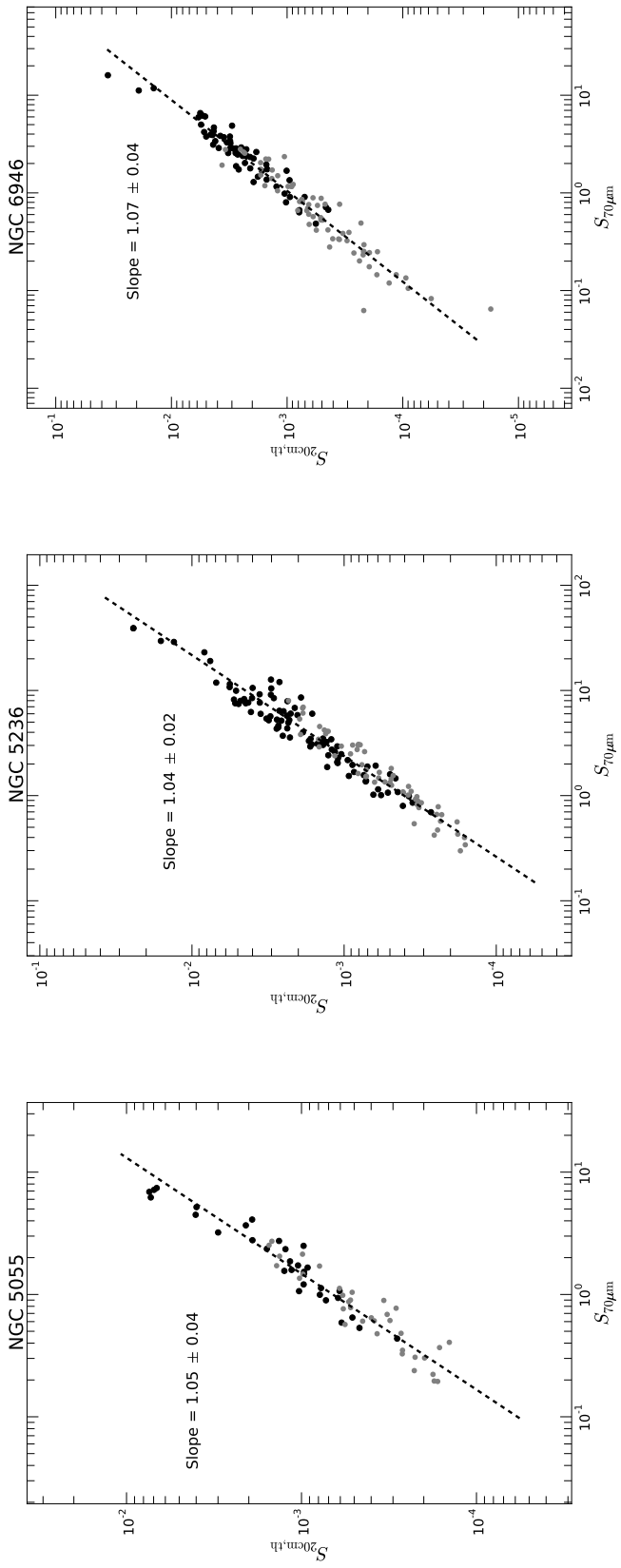

Figure 5.2: Thermal radio intensity at λ20 cm vs. λ70 μm intensity (in Jy beam^{-1}). The black points shows the arm regions and the grey points shows the interarm regions.

Table 5.1: Integrated flux densities of the galaxies at λ90 cm (0.33 GHz; Chapter 3), λ20 cm (1.4 GHz; spectral index scaled from data given in column 9 of Table 3.1) and λ70 μm (taken from the NED). The map noise (σ)for the 40 arcsec resolution images are also given.

Name	S_{90cm} Jy	σ_{90cm} mJy beam^{-1}	S_{20cm} Jy	σ_{20cm} mJy beam^{-1}	$S_{70\mu m}$ Jy	$\sigma_{70\mu m}$ mJy beam^{-1}
NGC 1097	2.10±0.14	2	0.40±0.02	0.15	59.84±4.66	15
NGC 4254	1.7±0.3	4	0.51±0.02	0.2	50.29±3.60	20
NGC 4736	0.9±0.06	2	0.31± 0.03	0.35	93.93± 7.34	15
NGC 5055	2.3±0.13	3	0.41± 0.05	0.4	72.57± 5.16	15
NGC 5236	6.86±0.62	2.5	2.36± 0.18	0.3	312.0± 15.6	30
NGC 6946	4.3±0.24	1	1.5± 0.1	0.2	207.2± 16.1	25

The parameter q is used as a measure of the radio–FIR correlation, where its dispersion indicates the tightness of the correlation. Conventionally it is defined as the logarithm of the ratio between total FIR flux between λ40 μm and λ120 μm and the radio flux measured at 1.4 GHz (see Section 2.2). However, we define q following Appleton et al. (2004), using FIR flux density at λ70 μm,

$$q_\lambda = \log_{10}\left(S_{70\mu m}/S_\lambda\right)$$

where, λ is the radio wavelength (here, λ = 20 cm or 90 cm) and $S_{70\mu m}$ and S_λ are the flux densities at λ70 μm and radio wavelength respectively. The FIR emission between λ40 μm and λ120 μm is dominated by emission from cool dust with dust temperature, $T_{\rm dust}$ $\sim$20 K (see e.g, Basu et al., 2012; Hoernes, Berkhuijsen & Xu, 1998; Tabatabaei et al., 2007b; Xu et al., 1992). The peak of this emission occurs around λ100 μm. Note that a black body at $\sim$20 K peaks around λ145 μm, but a grey body ($\lambda^{-\beta}B_\lambda(T)$, where $\beta = 2$ is the dust emissivity index and $B_\lambda(T)$ is the Planck function) has a peak at $\sim$ λ100 μm. The maps at λ70 μm, nearest available around λ100 μm, essentially traces this component of the dust. The use of monochromatic λ70 μm emission to study the radio–FIR correlation do not affect the conclusions significantly except for a slight increase in the dispersion (Murphy et al., 2006).

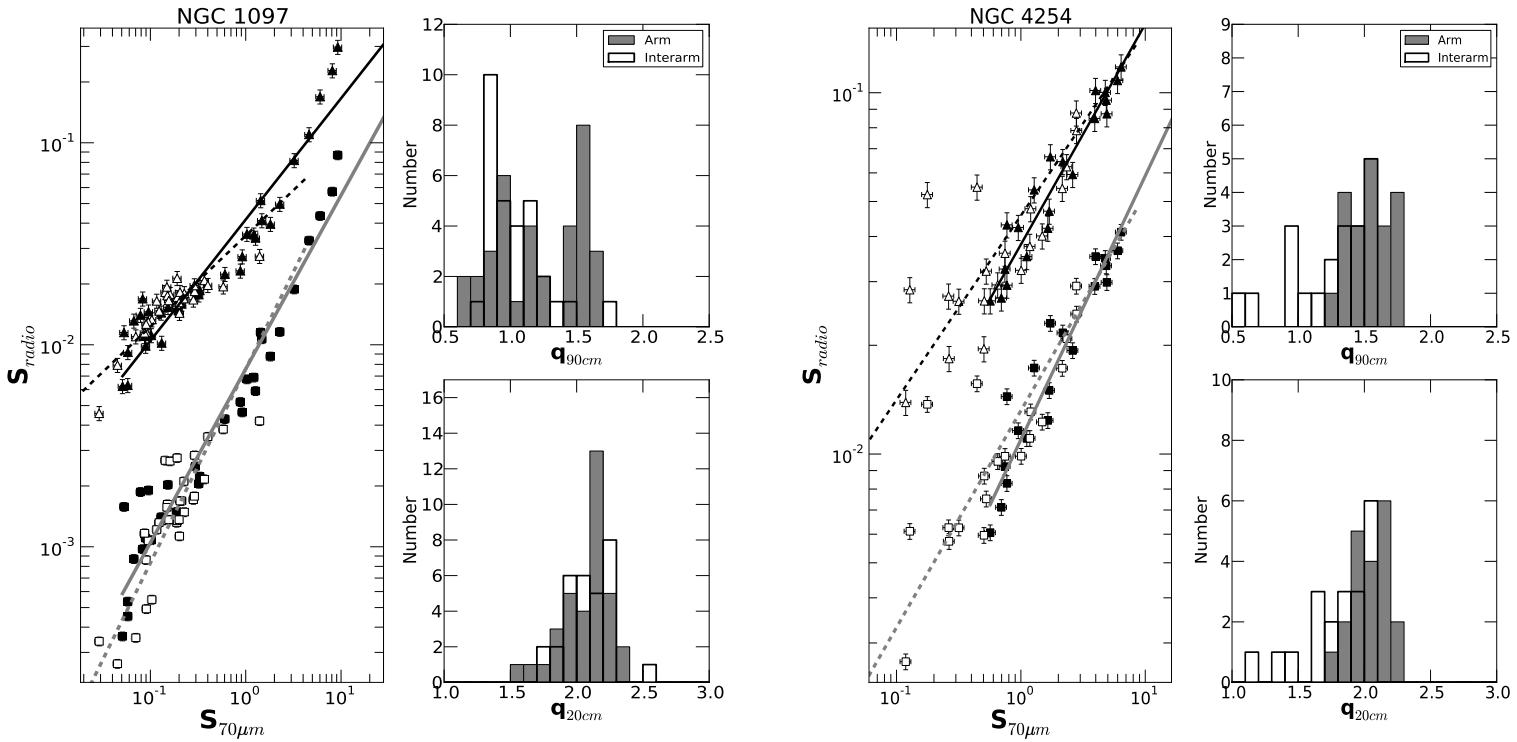

Figure 5.3: The figure shows the radio intensity vs. λ70 μm FIR intensity (in Jy beam^{-1}). The triangles are for λ90 cm and squares are for λ20 cm. The filled symbols are for arms and unfilled symbols are for interarms. The histograms are the distribution of $q_{90\mathrm{cm}}$ and $q_{20\mathrm{cm}}$, where arms are shown with filled grey and interarms with unfilled histograms. The lines are the fit to the data of the form $S_{\mathrm{radio}} = a \times S^{b}_{70\mu\mathrm{m}}$ (See Table 3). The solid and dashed lines are fit to the arm and interarm regions. Black lines are for λ90 cm, while grey lines are for λ20 cm.

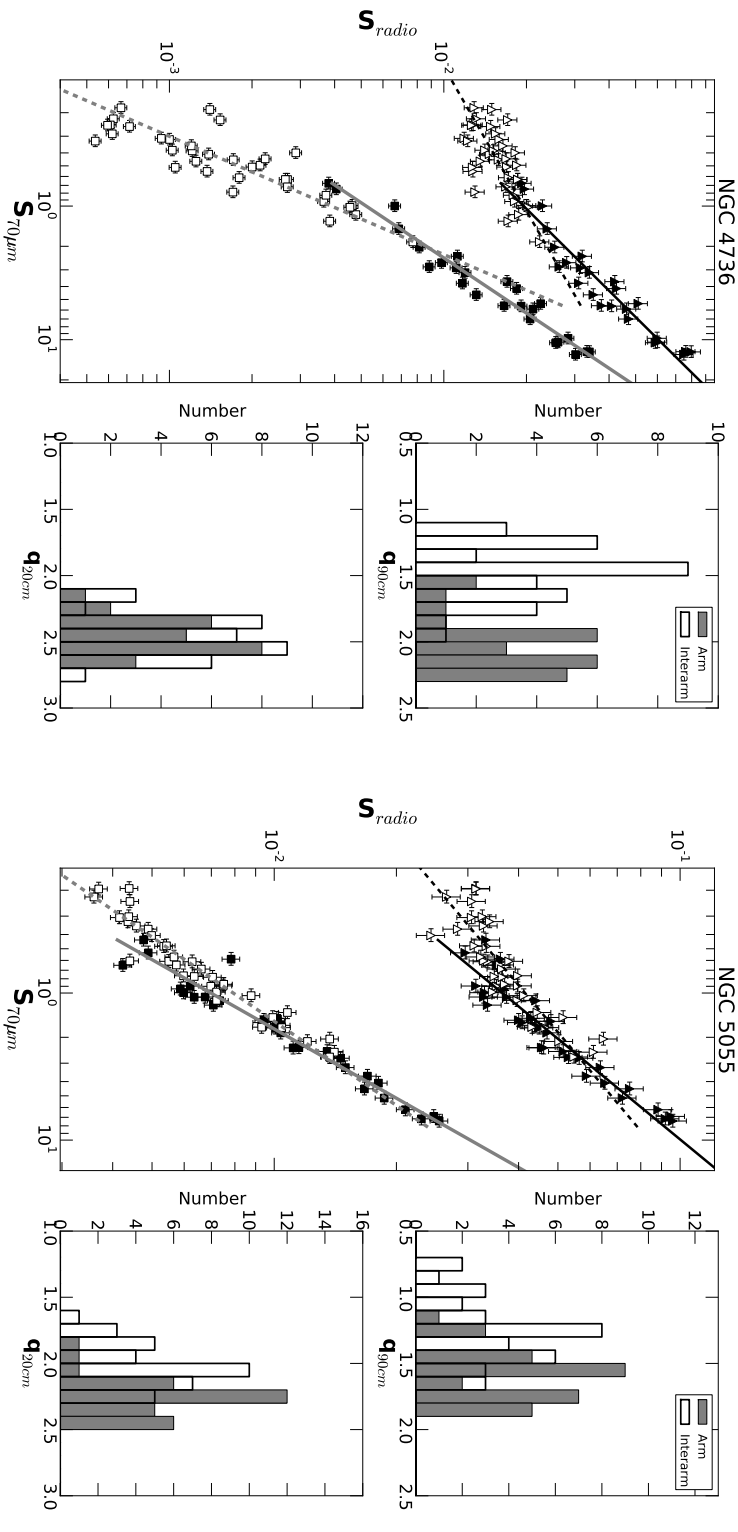

Figure 5.3: The figure shows the radio intensity vs. $\lambda 70$ μm FIR intensity (in Jy beam^{-1}). The triangles are for $\lambda 90$ cm and squares are for $\lambda 20$ cm. The filled symbols are for arms and unfilled symbols are for interarms. The histograms are the distribution of $q_{90\mathrm{cm}}$ and $q_{20\mathrm{cm}}$, where arms are shown with filled grey and interarms with unfilled histograms. The lines are the fit to the data of the form $S_{\mathrm{radio}} = a \times S^{b}_{70\mu\mathrm{m}}$ (See Table 3). The solid and dashed lines are fit to the arm and interarm regions. Black lines are for $\lambda 90$ cm, while grey lines are for $\lambda 20$ cm.

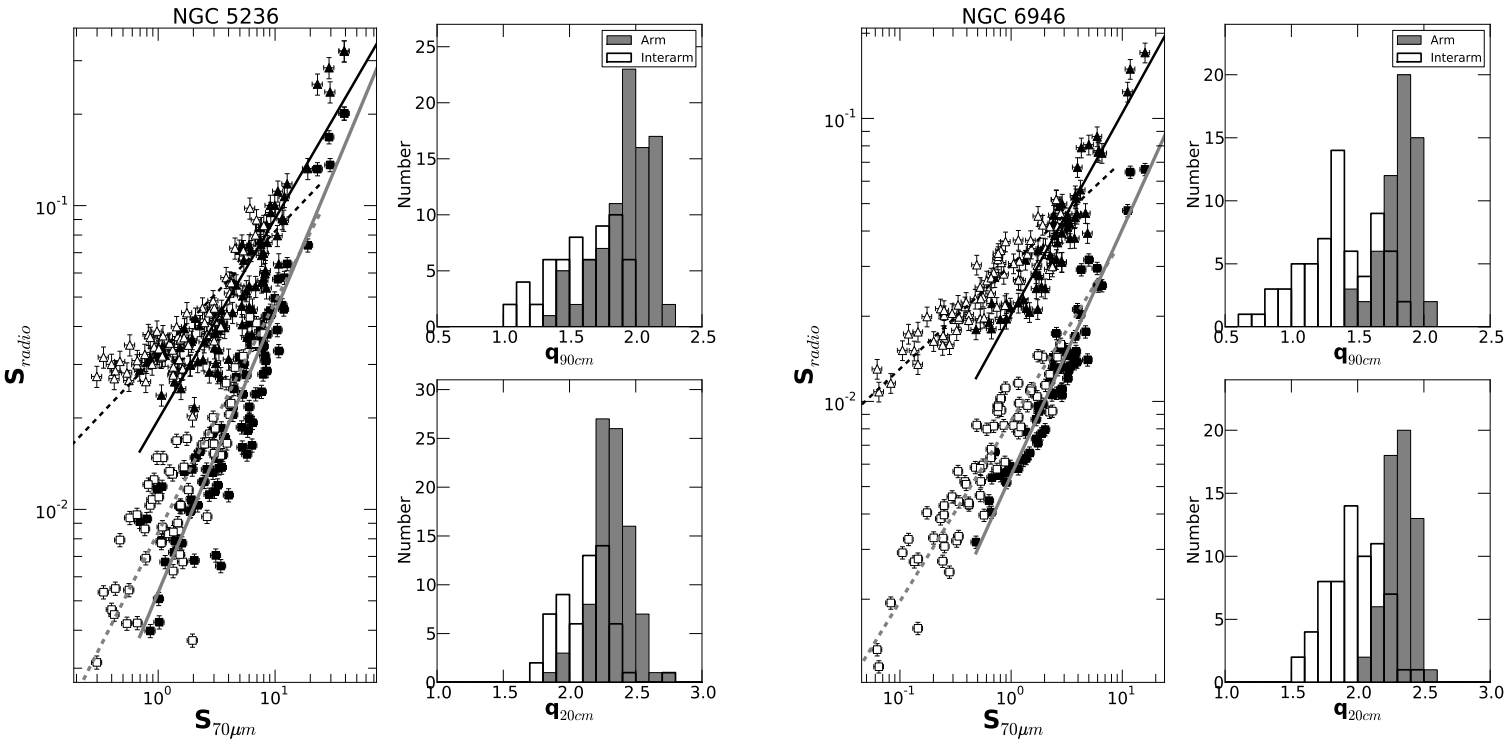

Figure 5.3: The figure shows the radio intensity vs. λ70 μm FIR intensity (in Jy beam^{-1}). The triangles are for λ90 cm and squares are for λ20 cm. The filled symbols are for arms and unfilled symbols are for interarms. The histograms are the distribution of $q_{90\mathrm{cm}}$ and $q_{20\mathrm{cm}}$, where arms are shown with filled grey and interarms with unfilled histograms. The lines are the fit to the data of the form $S_{\mathrm{radio}} = a \times S^{b}_{70\mu\mathrm{m}}$ (See Table 3). The solid and dashed lines are fit to the arm and interarm regions. Black lines are for λ90 cm, while grey lines are for λ20 cm.

5.2 Results

The spatially resolved study of the radio–FIR correlation was conducted by broadly classifying the emission from arm (including the central region) and interarm regions of these galaxies. The arms were identified from the Hα images of each galaxy. For the ringed galaxy NGC 4736, which has no prominent arms, the star forming ring was taken as the arm. The arm and the interarm regions used in our analysis are plotted as circles overlaid on the 40 arcsec Hα images in Figure 5.1. The quantity q_λ was computed within each such region. Note that the calibration uncertainty at $\lambda 70$ μm could be as high as 20 percent (Murphy et al., 2006) leading to a systematic error of about 10 percent in the values of q_λ. Here, we present separately the correlation between thermal and nonthermal component of radio emission with FIR emission.

5.2.1 Thermal radio–FIR correlation

It is expected that the thermal free–free emission in radio, and the FIR emission should be correlated. Star formation activity directly gives rise to both the emissions and therefore they are expected to be linearly correlated with each other. In Figure 5.2 we plot the brightness of the thermal radio emission at $\lambda 20$ cm ($S_{\rm 20cm,th}$) and the FIR emission at $\lambda 70$ μm ($S_{70\mu\rm m}$) for the galaxies NGC 5055, NGC 5236 and NGC 6946. The black and gray points represents the arm and interarm regions respectively. A tight correlation is observed between thermal component of radio emission and the FIR emission (Pearson's correlation coefficient, $r > 0.95$). The slope of the correlation is close to unity, with mean slope of 1.05±0.03, i.e, $S_{\rm 20cm,nt} \propto S_{70\mu\rm m}^{1.05\pm0.03}$.

This brings to light the importance of studying the radio–FIR correlation after separating the thermal emission. The slope of the radio–FIR correlation between non-thermal radio emission and far infrared emission is important in understanding the connection between magnetic field and gas density (discussed in Chapter 1 and Section 2.3). The tight correlation between thermal component of radio emission and FIR emission would influence the slope of the radio–FIR correlation.

5.2.2 Nonthermal radio–FIR correlation

Table 5.1 gives the total flux density (in Jy) and map rms noise of the 40 arcsec images (in mJy beam^{-1}) of the galaxies. The galaxy integrated mean values of $q_{\rm 20cm}$ are 2.18 ± 0.06, 2.03 ± 0.05, 2.48 ± 0.1, 2.25 ± 0.07, 2.12 ± 0.06 and 2.14 ± 0.07, for the

galaxies NGC 1097, NGC 4254, NGC 4736, NGC 5055, NGC 5236 and NGC 6946 respectively. The $q_{90\mathrm{cm}}$ values are 1.46 ± 0.08, 1.48 ± 0.07, 2.02 ± 0.07, 1.5 ± 0.1, 1.66 ± 0.09 and 1.68 ± 0.08 respectively. However, the spatially resolved estimates of $q_{20\mathrm{cm}}$ and $q_{90\mathrm{cm}}$ suggests that their values vary between arm and interarm regions. Figure 5.3 shows the brightness of the nonthermal radio emission with the far infrared emission at $\lambda 70$ μm, in units of Jy beam^{-1}, for all the four galaxies. The figure also shows the distribution of q_λ at $\lambda 20$ cm and $\lambda 90$ cm. It was seen that the high star forming gas rich spiral arms of the galaxies showed higher values for q_λ when compared to the adjacent low star forming interarm regions. Table 5.2 summarizes the mean values of the quantity q_λ and its dispersion for arm and interarm regions.

The mean value in the arms for all the galaxies were found to be $\langle q_{20\mathrm{cm}} \rangle_{\mathrm{arm}} = 2.32$ with a narrow dispersion of $\sigma_{q_{20\mathrm{cm}},\mathrm{arm}} = 0.14$, while for the interarms $\langle q_{20\mathrm{cm}} \rangle_{\mathrm{interarm}} = 2.15$ with $\sigma_{q_{20\mathrm{cm}},\mathrm{interarm}} = 0.3$. At $\lambda 90$cm we find $\langle q_{90\mathrm{cm}} \rangle_{\mathrm{arm}} = 1.85$ with $\sigma_{q_{90\mathrm{cm}},\mathrm{arm}} = 0.22$ and $\langle q_{90\mathrm{cm}} \rangle_{\mathrm{interarm}} = 1.43$ with $\sigma_{q_{90\mathrm{cm}},\mathrm{interarm}} = 0.3$. Figure 5.4 shows the percentage change in the value of q_λ between arms and interarms of each of the galaxy, where $\Delta q = \langle q_\lambda \rangle_{\mathrm{arm}} - \langle q_\lambda \rangle_{\mathrm{interarm}}$. The blue squares represent $\lambda 20$ cm and red triangles $\lambda 90$ cm. The mean of the $q_{20\mathrm{cm}}$ changes slightly, around 9 percent, between the arms and interarms with a significance of > 99.9 percent confidence using Kolmogorov-Smirnov test. At $\lambda 90$ cm the change in the value of $\langle q_\lambda \rangle$ between arm and interarm regions are much pronounced with $\Delta q \sim 30$ percent.

5.2.2.1 Fit to the radio and IR flux densities

The data were fitted using the form $S_{\mathrm{radio}} = a \times S_{\mathrm{IR}}^b$, where S_{radio} is the flux density of the radio emission at $\lambda 20$cm and $\lambda 90$cm, and S_{IR} is the flux density of the $\lambda 70 \mu$m infrared emission. We define a quantity $\bar{q}_\lambda = -\log_{10} a$ for $S_{IR} = 1$, such that the value of $\bar{q}_\lambda$ correspond to the intercept of the straight line fit of $\log_{10} S_\lambda = -\bar{q}_\lambda + b \times \log_{10} S_{IR}$. The slope of the radio-infrared correlation is given by the parameter 'b'. Separate fits were sought in the log-log domain for the arm and interarm regions using ordinary least-square 'bisector method' (Isobe et al., 1990). The parameters obtained from the fits are summarized in Table 5.2 (last four columns for $\lambda 20$ cm and $\lambda 90$ cm). The fitted values of $\bar{q}_{90\mathrm{cm}}$ and $\bar{q}_{20\mathrm{cm}}$ are in good agreement with $\langle q_\lambda \rangle$. The fitted parameters are plotted in Figure 5.3. The black lines are for fits at $\lambda 90$cm and the gray lines for $\lambda 20$cm. The solid lines are fits to the arm regions while the dashed lines are for the interarms. All the correlations are highly significant with Pearson's correlation coefficient $r > 0.8$

Table 5.2: Summary of the values of q_λ and the fitted parameters for each of the galaxies. Columns 3, 4 and 5, 6 are the mean values of q_λ and their dispersion at λ20cm and λ90cm respectively as shown in Figure 5.3. The value of q_λ was computed using the flux density within one beam of FWHM $\sim$ 40 arcsec. Columns 7 and 9 gives the fitted values for $\bar{q}_\lambda = -\log_{10} a$ and Columns 8 and 10 gives the slopes of the radio–FIR correlation. Here, $a_{20\mathrm{cm}}$, $b_{20\mathrm{cm}}$ and $a_{90\mathrm{cm}}$, $b_{90\mathrm{cm}}$ are the parameters a and b in the fitted equation, $S_{\mathrm{radio}} = aS^b_{\mathrm{IR}}$, at wavelengths 20 cm and 90 cm respectively.

Name		$\langle q_{20\mathrm{cm}} \rangle$	$\sigma_{q_{20\mathrm{cm}}}$	$\langle q_{90\mathrm{cm}} \rangle$	$\sigma_{q_{90\mathrm{cm}}}$	$S_{\mathrm{radio}} = aS^b_{\mathrm{IR}}$			
						$-\log(a_{20\mathrm{cm}})$	$b_{20\mathrm{cm}}$	$-\log(a_{90\mathrm{cm}})$	$b_{90\mathrm{cm}}$
(1)	(2)	(3)	(4)	(5)	(6)	(7)	(8)	(9)	(10)
NGC 1097	arm:	2.11	0.19	1.21	0.32	2.12±0.03	0.86±0.04	1.38±0.04	0.60±0.04
	interarm:	2.10	0.17	1.04	0.21	2.12±0.13	0.96±0.15	1.46±0.08	0.45±0.10
NGC 4254	arm:	2.03	0.13	1.53	0.15	1.96±0.03	0.73±0.05	1.42±0.02	0.61±0.03
	interarm:	1.86	0.26	1.25	0.31	1.88±0.03	0.60±0.07	1.34±0.04	0.51±0.05
NGC 4736	arm:	2.45	0.12	2.01	0.20	2.28±0.02	0.73±0.04	1.71±0.03	0.49±0.04
	interarm:	2.46	0.15	1.46	0.23	2.41±0.04	1.13±0.12	1.71±0.03	0.28±0.04
NGC 5055	arm:	2.26	0.14	1.59	0.20	2.14±0.02	0.64±0.03	1.44±0.02	0.44±0.03
	interarm:	2.03	0.16	1.27	0.24	2.10±0.01	0.53±0.03	1.38±0.01	0.30±0.04
NGC 5236	arm:	2.32	0.14	1.92	0.20	2.27±0.04	0.92±0.04	1.71±0.03	0.66±0.04
	interarm:	2.13	0.20	1.60	0.26	2.08±0.03	0.76±0.05	1.50±0.02	0.40±0.04
NGC 6946	arm:	2.31	0.10	1.81	0.14	2.26±0.02	0.87±0.04	1.69±0.02	0.71±0.04
	interarm:	1.97	0.19	1.32	0.32	2.07±0.01	0.64±0.03	1.52±0.01	0.34±0.02

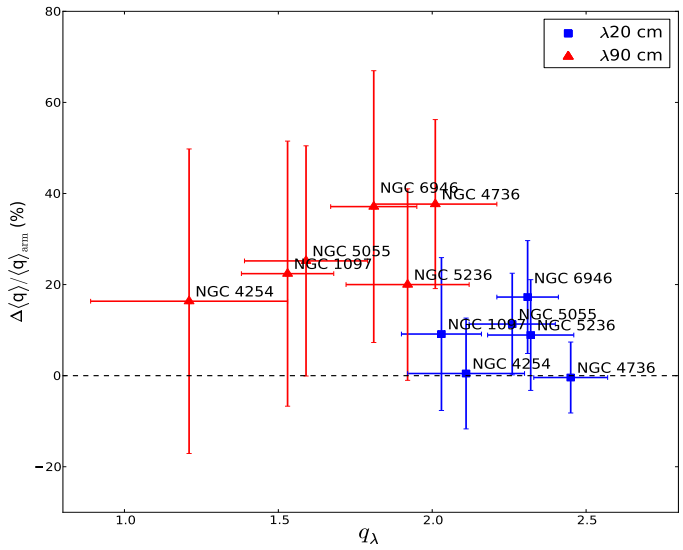

Figure 5.4: The percentage change in the value of $\langle q_\lambda \rangle$ between arms and interarms. Here, $\Delta\langle q \rangle = \langle q_\lambda \rangle_{\rm arm} - \langle q_\lambda \rangle_{\rm interarm}$ for each of the sample galaxies. The red triangles are for λ90cm and blue squares are for λ20cm. The mean change in the value of $q_{\rm 20cm}$ between arms and interarms is ~ 10 percent, while $q_{\rm 90cm}$ changes by ~ 30 percent.

(and $r > 0.9$ in most of the cases), except for interarm regions of NGC 4736 at λ90 cm where $r = 0.68$.

The slope of the λ20 cm and λ70 μm flux density of the arm regions for all the galaxies lie between 0.65 – 0.9. However, for the interarm regions the slope is slightly shallower lying in the range 0.55 – 1. The mean value of the parameters for the arm and interarm regions after the fit is expressed as,

$$\log_{10} S_{\rm 20cm} = \begin{cases} -(2.17 \pm 0.02) + (0.80 \pm 0.05) \log_{10} S_{70\mu{\rm m}}, & \text{arm} \quad (5.1) \\ -(2.11 \pm 0.03) + (0.77 \pm 0.10) \log_{10} S_{70\mu{\rm m}}, & \text{interarm} \quad (5.2) \end{cases}$$

The fitted value of $\bar{q}_{\rm 20cm}$ and the slope differs slightly from the arms to the interarms.

At λ90cm we find that slope lying in the range 0.45 – 0.7 for the arms, whereas in the interarm regions the slope lie between 0.3 – 0.4, the slopes being much flatter compared to λ20cm. The mean value of the fitted parameters are found to be,

$$\log_{10} S_{\rm 90cm} = \begin{cases} -(1.56 \pm 0.02) + (0.60 \pm 0.06) \log_{10} S_{70\mu{\rm m}}, & \text{arm} \quad (5.3) \\ -(1.48 \pm 0.03) + (0.38 \pm 0.14) \log_{10} S_{70\mu{\rm m}}, & \text{interarm} \quad (5.4) \end{cases}$$

There is a significant change in the value of $\bar{q}_{90\mathrm{cm}}$ and the slope between the arm and the interarm regions.

We note that 'q_λ' is related to the slope of the radio–FIR correlation, b and the parameter a as, $q_\lambda = (1-b)\log S_{\mathrm{IR}} - \log a$. Thus, for non-linear slope of the correlation, i.e., $b \neq 1$, q_λ depends on the far–infrared flux density S_{IR}. This is true for our case and hence q_λ cannot be used as a good measure of the tightness of the radio–FIR correlation (Rainer Beck, private communication).

5.2.2.2 q vs. α_{nt}

The quantity 'q_λ' can be expressed in terms of CRe escape timescale (τ_{esc}) and synchrotron timescale (τ_{syn}) as $q_\lambda \propto \log(\tau_{\mathrm{syn}}/\tau_{\mathrm{esc}})$ (Murgia et al., 2005; Paladino et al., 2006). CRes emitting for these timescales also determine the variations in nonthermal spectral index (α_{nt}) from sites of injection to regions of dominant energy loss. In Figure 5.5 we represent the variation of $q_{20\mathrm{cm}}$ (left) and $q_{90\mathrm{cm}}$ (right) with the α_{nt} determined at linear scales of $\sim 1-2.8$ kpc from Figure 4.3 for all these galaxies. The distribution of α_{nt} with steps of 0.05 are shown in the top panels. The right panels in Figure 5.5 show the distribution of q_λ for the two frequencies. The shaded histograms represent the arms and the unfilled histograms are for the interarms. At λ20 cm there is no apparent variation in the value of $q_{20\mathrm{cm}}$ with α_{nt} (Pearson's correlation coefficient, $r = 0.27$), while at λ90 cm the $q_{90\mathrm{cm}}$ decreases with steepening of the α_{nt} ($r = 0.7$).

In the arm regions where α_{nt} is seen to have a narrow distribution with mean 0.8 and dispersion of 0.14, the q_λ values are higher suggesting $\tau_{\mathrm{syn}} \gg \tau_{\mathrm{esc}}$. However, in the interarm regions α_{nt} and q_λ have a wide distribution with more than 50 percent dispersion. The values of 'q_λ' also systematically decreases as one moves from arms to interarms indicating $\tau_{\mathrm{esc}} \gg \tau_{\mathrm{syn}}$, thereby implying that the CRes loose energy before escaping the disk giving rise to steeper α_{nt}. Similar results were found for IC 342 and NGC 5194 (M51) in Murgia et al. (2005) and Paladino et al. (2006).

5.3 Discussion

We have studied the radio–FIR correlation at $\sim$1 kpc scales for six normal galaxies using nonthermal radio maps at λ90 cm and λ20 cm and the far infrared maps at λ70 μm. From the basic synchrotron theory (e.g., Moffet 1975) and considering the radio emission from CRe emitting at critical frequencies, the energy of CRes at λ90

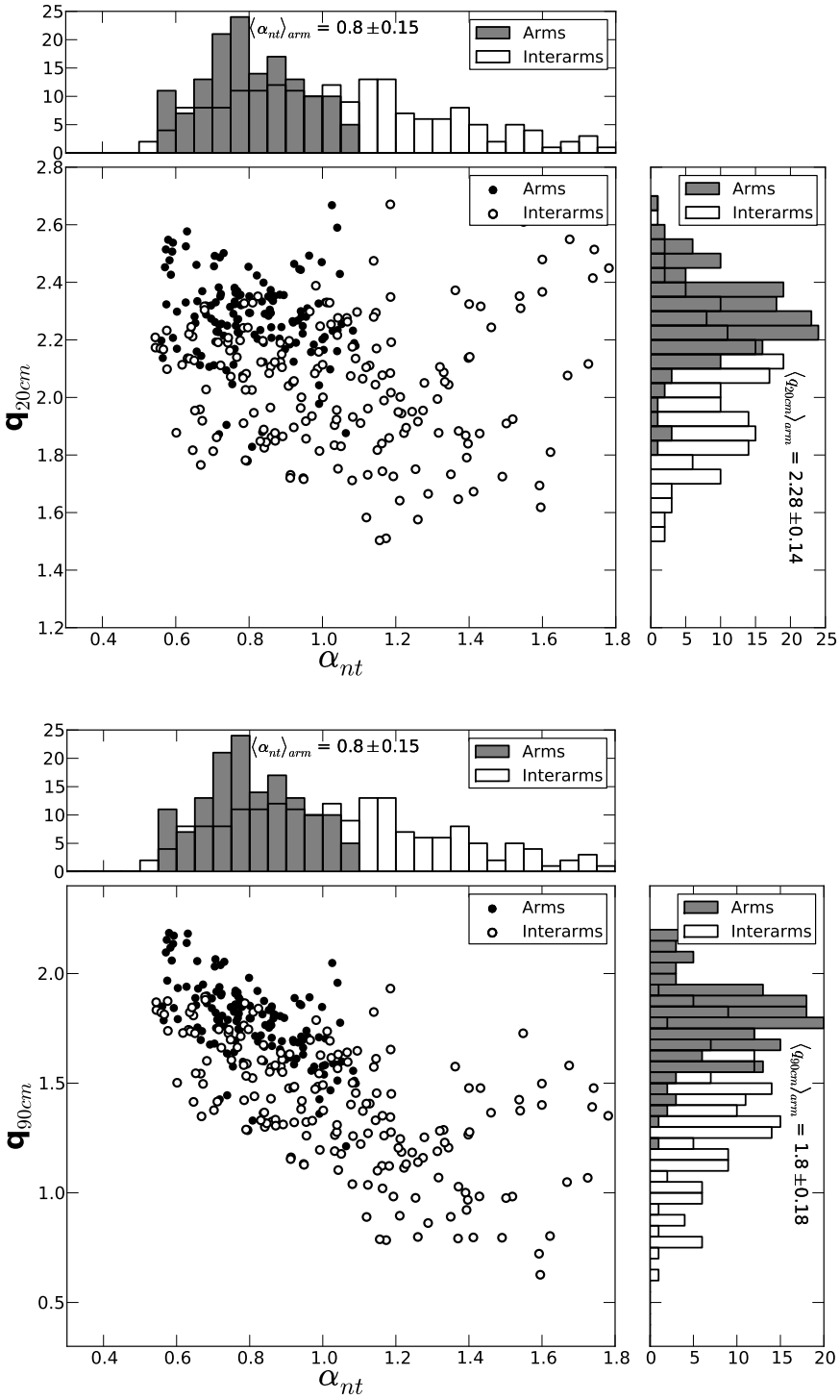

Figure 5.5: The figure shows the distribution of $\alpha_{\rm nt}$ with $q_{\rm 20cm}$ (left) and $q_{\rm 90cm}$ (right). The top panel shows the distribution of $\alpha_{\rm nt}$ estimated from λ90cm and λ20cm non-thermal emission radio maps within an area of 40×40 arcsec^2 and a step size of 0.05, while the right side horizontal panel shows the distribution of q_λ within the same area and bin size of 0.05. The filled circles and histograms are for the arms and unfilled circles and histograms are for interarm regions for all the galaxies combined.

cm is ∼1.5 GeV and at λ20 cm is ∼3 GeV when they are gyrating in typical magnetic fields of $\sim$ 10 μG. The FIR emission at λ70 μm originates from cool dust at ∼20 K heated by the interstellar radiation field (ISRF) due to $\sim 5 - 20$ $M_\odot$ stars (Basu et al., 2012; Devereux & Eales, 1989; Dumas et al., 2011; Xu, 1990; Xu & Helou, 1996). We have separately examined these correlations for the arm and the interarm regions, that is regions of high and low thermal fractions respectively. The fits to the various parameters discussed in Section 5.2 are given in Table 5.2, for individual galaxies, and here we discuss their average properties. The dispersion of the parameter q_λ is a measure of the tightness of the radio–FIR correlation which in the arm region is found to be less than 10 percent, around $\langle q_\lambda \rangle$, at both λ20 cm and λ90 cm. In the interarm region the dispersion increases to around 20 percent at both frequencies. Further we find the slope of the radio–FIR correlation in the arm regions (also the high thermal fraction regions) remains similar at both radio frequencies (see Table 5.2). It should be noted that a large number of studies showing global scale radio–FIR correlation exist where the observed slope is steeper and closer to unity (see e.g., Price & Duric, 1992; Yun, Reddy & Condon, 2001, and the references therein). However, the spatially resolved studies relating FIR cool dust emission to λ20 cm radio emission yields a value of the slope 0.6 – 0.9 for LMC (Hughes et al., 2006) and 0.80 ± 0.09 for M31 (Hoernes, Berkhuijsen & Xu, 1998). For a sample of seven galaxies, Paladino et al. (2006) found a mean slope of 0.7±0.1 between radio continuum emission at λ20 cm and FIR emission at λ24 μm. The flux in global studies are averaged over both the arm and the interarm regions with uncertainty about the contribution from each, making comparison with spatially resolved case difficult. More multifrequency spatially resolved studies are required to understand the relation between global and spatially resolved studies. In our present studies, the slope is slightly flatter in the interarm regions (regions of low thermal fraction) as compared to the arms at λ20 cm (see Equations 5.1 and 5.2). However, at λ90 cm in the interarms the slopes become distinctly flatter than the arm regions (see Figure 5.3 and Equations 5.3 and 5.4).

Our results can be used to determine the coupling between the magnetic field (B) and the gas density ($\rho_{\rm gas}$) as discussed in the Section 2.3.2 and thereby validate the 'equipartition' assumptions in these galaxies at 1 kpc scales. Dumas et al. (2011)

showed the relation between the slope of the radio–FIR correlation and κ as,

$$\kappa = \begin{cases} \dfrac{n\ b}{3+\alpha_{\rm nt}}, & \text{optically thick dust} \quad (5.5) \\ \dfrac{(n+1)\ b}{3+\alpha_{\rm nt}}, & \text{optically thin dust} \quad (5.6) \end{cases}$$

where, $n = 1.4\pm0.15$ is the index from Kennicutt-Schmidt law (see e.g., Kennicutt, 1998), b is the slope of the radio–FIR correlation and $\alpha_{\rm nt}$ is the nonthermal spectral index. For these face-on galaxies we use the assumption of optically thin dust to UV photons to estimate κ as 0.51 ± 0.1 at λ20 cm and 0.4 ± 0.1 at λ90 cm in the arm regions. Similarly, for the interarm regions due to a large range of $\alpha_{\rm nt}$ we find κ in the range 0.41 – 0.5 at λ20 cm and between 0.18 – 0.22 at λ90 cm. Our estimated values of κ using the correlation between λ20 cm and λ70 μm are consistent with the predictions of numerical MHD simulations using different ISM turbulence models, where the typical range of κ is 0.4 – 0.6 (see e.g., Fiedler & Mouschovias, 1993; Groves et al., 2003; Kim, Balsara & Mac Low, 2001; Thompson et al., 2006).

In the arm regions the slope and thus κ remain similar at both λ20 cm and λ90 cm, within errors. Note that the above prescription to determine κ is valid provided the radio and the FIR emission arises from the same emitting volume, a diameter of about 1 kpc for most of the observations reported here. In the arm regions the UV photons have a mean free path of ∼100 pc within which most of the FIR emission arise. On the other hand, the CRes which give rise to the radio emission propagate farther away to $\sim$ 1 kpc at λ20 cm and $\sim$ 2 kpc at λ90 cm in galactic magnetic fields of $\sim$ 10 μG. A similar slope with frequency requires the energy spectrum of the CRes, giving rise to the radio emission, to be independent of the volume element. This can happen only if the timescale of CRe diffusion/propagation ($\tau_{\rm diff}$) is significantly higher than the CRe generation timescale ($\tau_{\rm gen}$). It turns out that the $\tau_{\rm diff}$ is about 8×10^7 yr at λ90 cm and 4×10^7 years at λ20 cm which is significantly longer than the $\tau_{\rm gen}$ as evident from the supernova rates of one every $10^4 - 10^5$ yr kpc^{-2} in Milky Way. In our assumption of same rate for these galaxies, we presage in the circumstance of energy equipartition in galaxies, index for Kennicutt-Schmidt is 1.4 and $\alpha_{\rm nt}$ is constrained in arms ($\sim$ 0.8; see Figure 4.13); the slope of radio–FIR correlation should be independent of the radio frequency lying in the range 0.6 – 0.9. In Figure 5.6, we show the radio–FIR correlation at angular resolution of 15 arcsec corresponding to ∼0.5 kpc between radio emission at λ90, 20 and 6 cm and FIR emission at λ70μm for the galaxy NGC 6946. The red

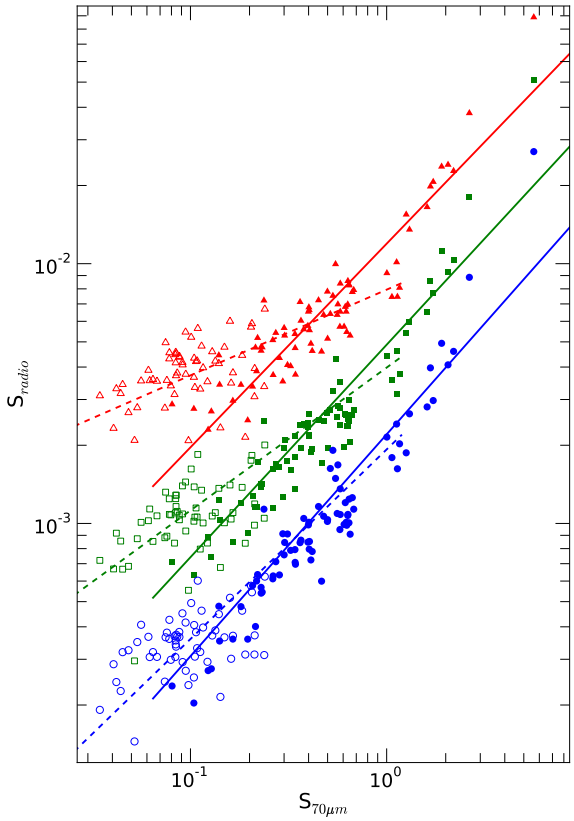

Figure 5.6: Multi waveband radio–FIR correlation for NGC 6946. The red triangles, green squares and blue circles points are at λ90, λ20 and λ6 cm respectively. The filled and open symbols are for arm and interarm regions respectively.

triangles represent λ90 cm, the green squares are for λ20 cm and blue circles are for λ6 cm. The filled and open symbols shows the arm and interarm regions, respectively. In the arms, the slope of the correlation is 0.78 ± 0.06 at λ90 cm, at λ20 cm it is found to be 0.82 ± 0.06 and at λ6 cm the slope is 0.85 ± 0.07. The slopes are similar within errors confirming the equipartition assumptions being applicable in galaxies. However, more studies of the correlation with multi frequency radio images are necessary to affirm this conjecture.

The slope of the radio–FIR correlation in the interarm (low thermal fraction) region is similar to that of the arm at λ20 cm, however, it becomes distinctly flatter at λ90 cm. The flattening primarily occurs due to the relative increase in radio flux at λ90 cm as compared to λ20 cm, which has the effect that $\alpha_{\rm nt}$ gradually becoming steeper in the interarms. This relative increase in λ90 cm flux can be explained by continuous

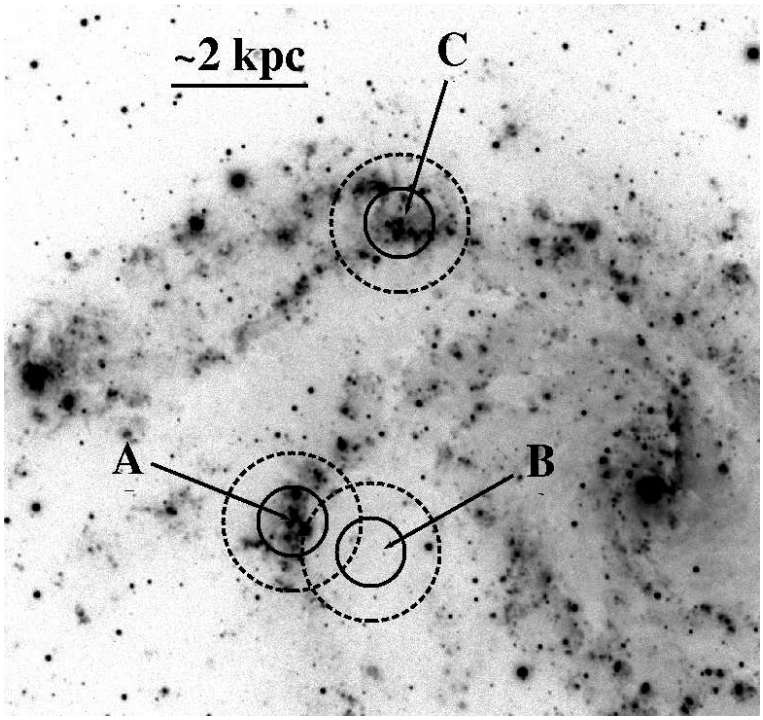

Figure 5.7: The Hα image of the galaxy NGC 6946 (KPNO 2-m telescope, filter: KP1563) obtained from the ancillary data at SINGS website. The solid circles represents the diffusion scale of $\sim$1 kpc for $\sim$ 3 GeV CRe at λ20 cm, while the dashed circles represents the diffusion scales of $\sim$2 kpc for $\sim$1.5 GeV CRe at λ90 cm. See text for the details.

generation of CRe in the arm which subsequently propagates into the interarm (e.g., from A to B or from farther regions in arms like C to B in Fig. 5.7). Assuming Alfvén velocity of 100 km s^{-1} and typical arm to interarm distance of 1–2 kpc, the CRes would propagate for few times 10^7 years. As a result, using Equation 6 of (Kardashev, 1962), in typical galactic magnetic fields of $\sim$ 10 μG, there would be a break in the electron energy spectrum above $\sim$2 GeV. The frequency corresponding to the break lies above 0.33 GHz. Such breaks have been seen at $\sim$ 0.9 GHz and $\sim$1 GHz for similar normal galaxies, NGC 3627 and NGC 7331 respectively (Paladino, Murgia & Orrú, 2009). The CRes emitting at λ90 cm, lying above the break do not loose significant amount of energy as compared to their higher energy counterparts, thereby increasing the relative flux at λ90 cm.

For the slope to remain similar between the arms and the interarm regions at λ20 cm (below the break), the ratio of the radio to FIR flux densities should also remain

similar. Observed radio flux between arm and interarm changes by a factor of ∼2–2.5 at λ20 cm. Similar ratio of flux density between arm and interarm regions at λ20 cm can be caused due to steeping of the spectral index to $\gtrsim$ 1.1 as compared to 0.6 – 0.8 in the arms. This implies the FIR flux should change by a factor of ∼2.5–3 between arm and interarm regions for radio–FIR slope to remain ∼0.8. The FIR flux density (F_λ) depends on the dust temperature ($T_{\rm dust}$) and density ($\rho_{\rm dust}$) as $F_\lambda \propto \rho_{\rm dust} Q_{\rm abs}(a,\lambda) B_\lambda(T_{\rm dust})$, where $Q_{\rm abs}(a,\lambda)$ is the FIR wavelength (λ) dependent absorption coefficient for gain radius a (Alton et al., 2004; Draine & Lee, 1984). The temperature do not change significantly between arm and interarm for these galaxies (Figure 4.1). For a constant gas-to-dust ratio, i.e, $\rho_{\rm dust} \propto \rho_{\rm gas}$, a factor of 2–4 drop in average gas density between arm and interarm regions (found using the $\rm CO_{J:2\rightarrow1}$ maps from Heracles; Leroy et al., 2009) would therefore cause the factor of 2–3 drop in FIR emission.

The slope of 0.8±0.1 of the radio–FIR correlation indicate that the energy equipartition assumption between cosmic ray particles and magnetic field may be valid in the gas rich arms of the galaxies at our spatial resolution of ∼1 kpc. For the interarm regions the slope is similar to what is seen in arms at λ20 cm, and thereby satisfying the equipartition conditions. The flattening of the slope, however at λ90 cm do not imply any break down of equipartition condition but results due to overlapping emissions from adjacent regions.

Chapter 6

Magnetic fields in galaxies: energy equipartition

Magnetic field strength plays an important role in determining the dynamics and energetics in a galaxy. It is believed that the magnetic pressure plays a role in determining the scale height of the galactic interstellar medium (ISM). Also, the magnetic field plays an important role in collapse of a gas cloud to help the star formation activity (Crutcher, 1999; Elmegreen, 1981). The density and distribution of cosmic rays depend on magnetic fields.

It is thought that the seed field, before formation of galaxies, was amplified by compression during collapse and shearing by a differentially rotating disk (Beck, 2006). Dynamo action within the galaxy amplifies and maintains field strength over galactic life-times of $\sim 10^9$ year (see e.g, Moffatt, 1978; Moss & Shukurov, 1996; Parker, 1979; Shukurov et al., 2006). Though the dynamo effect can amplify the large scale mean magnetic field, magnetohydrodynamic (MHD) turbulence can amplify the local magnetic field through field line stretching (Batchelor, 1950; Groves et al., 2003) up to energy equipartition levels. In steady state, the energy density of magnetic field is close to energy density of the gas. Gas density is known to fall as a function of galactocentric distance (see e.g., Leroy et al., 2008). Therefore, it is expected that the field strength will fall as a function of galactocentric distance.

Observationally, the magnetic field (B) can be traced by polarization studies at various wavebands, e.g., Faraday rotation and synchrotron radiation polarization in radio, polarization of starlight in optical and polarized dust emission in infrared. Zeeman splitting of spectral lines can be used to estimate the local magnetic field. Intensity

of the synchrotron emission at radio wavelengths can provide estimates of B though assumptions of 'equipartition' of energy between cosmic ray particles and magnetic field.

Faraday rotation can probe the line-of-sight averaged magnetic field ($B_{\parallel}$). However, this method uses polarized radio emission that may not be seen from a large fraction of a galaxy due to Faraday and/or beam depolarization (Sokoloff et al., 1998). Zeeman splitting can directly measure $B_{\parallel}$, but it is highly susceptible to high localized magnetic field. Moreover, its detection is difficult in external galaxies. Estimation of B in the sky-plane using polarization of starlight or dust emission depends highly on several geometrical and physical parameters (Zweibel & Heiles, 1997). Synchrotron emission is seen from large fraction of a galaxy and under the condition of 'equipartition', it provides a measure of total magnetic field. At low frequencies (0.33 GHz), more than 95 percent of the emission is synchrotron in origin (Basu et al., 2012) therefore low radio frequency total intensity images can be used to determine B in galaxies.

This method has been used to determine B in some of the nearby star forming galaxies. In M51, Fletcher et al. (2011) found generally stronger fields of $\sim 20-25$ μG in the spiral arms and $\sim 15-20$ μG in the interarm regions. In this case, B was determined using total intensity map at $\lambda 6$ cm assuming a constant spectral index for thermal and synchrotron emission. This might introduce errors in the results as the nonthermal spectral index steepens from center to edge (Basu et al., 2012). In NGC 253, the field was found to be ~ 20 μG towards the center and fell to ~ 8 μG towards the edge (Heesen et al., 2009). In M82, the total field was found to be ~ 80 μG in the center and $\sim 20-30$ μG in the synchrotron emitting halo (Adebahr et al., 2012). However, these galaxies are known starbursts, the magnetic field in the disk could be significantly affected by mixing of magnetic field from other parts of the galaxy through galactic fountain (Bregman, 1980; Heald, 2012; Norman & Ikeuchi, 1989; Shapiro & Field, 1976).

To measure magnetic field and to compare its energy density with that in gas at high spatial resolution of $\lesssim 1$ kpc we have observed five nearly face-on normal galaxies, namely, NGC 1097, NGC 4254, NGC 4736, NGC 5055, NGC 5236 and NGC 6946. In Section 6.1, magnetic field strengths in these galaxies are determined using total intensity synchrotron emission at 0.33 GHz. In Section 6.2, we present the magnetic field maps and results. We discuss our results and compare the magnetic field energy with kinetic energies in turbulent gas in various phases of the ISM in Section 6.3. Our results are summarized in Section 6.4.

6.1 Data analysis

The galaxies studied here selected from Basu et al. (2012) (presented in Chapter 3). A thorough separation of thermal emission from the total emission was done at 0.33 GHz (λ90 cm) and near 1.4 GHz (λ20 cm) using Hα corrected λ24 μm as the tracer (see Chapter 3). Our sample comprises of NGC 1097, NGC 4254, NGC 4736, NGC 5055, NGC 5236 and NGC 6946. The nonthermal spectral index ($\alpha_{\rm nt}$) used to compute the equipartition magnetic field, was estimated between the above mentioned frequencies. The data sources for the sample galaxies are listed in Table 3.1. We broadly classified our studies for arm and interarm regions identified using the λ24 μm images of each galaxy, i.e., regions of high and low gas density respectively.

For the spatially resolved study of the energy densities in the ISM, we used data from THINGS (Walter et al., 2008) to trace HI surface mass density, and from HERACLES (Leroy et al., 2009) and NRAO 12-m telescope (Crosthwaite et al., 2002) to trace H_2 surface mass density (see Appendix A for details). All the maps for a galaxy was convolved to a common resolution of the nonthermal maps (see Table 4.1) and re-gridded to common pixel size of 3 arcsec. They were then aligned to the same coordinate system for further analysis.

6.1.1 Total magnetic field

From basic synchrotron theory, and assuming energy equipartition between cosmic ray particles and the magnetic field, the total field strength could be estimated (see e.g., Longair, 2011; Miley, 1980; Pacholczyk, 1970). However, the limits of integration ($\nu_{\rm min}$ to $\nu_{\rm max}$) over the synchrotron spectrum to estimate the total energy in cosmic ray electrons (CRe) depends on the magnetic field (Beck et al., 2005). This was ignored while minimizing the total energy in magnetic field and cosmic ray particles to derive the 'classical' equipartition formula (Equation 2 of Miley, 1980). This gives rise to overestimation of the field in regions of steep nonthermal spectral index ($\alpha_{\rm nt} > 0.7$, defined as $S_\nu \propto \nu^{-\alpha_{\rm nt}}$).

We used the 'revised' equipartition formula given in Equation 3 of Beck & Krause (2005) to produce total magnetic field maps, where the equipartition field strength ($B_{\rm eq}$) is given as,

$$B_{\rm eq} = \left\{ 4\pi(K_0+1)E_p^{1-2\alpha_{\rm nt}} \frac{f(\alpha_{\rm nt})}{c_4(i)} \frac{I_\nu \nu^{\alpha_{\rm nt}}}{l} \right\}^{1/(\alpha_{\rm nt}+3)} . \tag{6.1}$$

Here, E_p is the rest mass energy of protons, I_ν is the nonthermal intensity at frequency ν, l is the path-length through the synchrotron emitting region. K_0 is the ratio of number density of relativistic protons and electrons, $c_4(i)$ is a constant depending on the inclination angle of the magnetic field. $f(\alpha_{\rm nt})$ is a function of $\alpha_{\rm nt}$ such that, $f(\alpha_{\rm nt}) = (2\alpha_{\rm nt}+1)/\left[2(2\alpha_{\rm nt}-1)c_2(\alpha_{\rm nt})c_1^{\alpha_{\rm nt}}\right]$, and c_1, c_2 are constants defined in Appendix of Beck et al. (2005).

We assume K_0, the ratio of number densities of relativistic protons ($n_{\rm CRp}$) and electrons ($n_{\rm CRe}$), such that $K_0 = n_{\rm CRp}/n_{\rm CRe} \simeq 100$. The path-length travelled through the source (l) is taken to be 2 kpc and corrected for the inclination. This could in principle be a function of galactocentric distance (r, i.e, $l \equiv l(r)$) depending on the shape of synchrotron emitting halo perpendicular to plane of galaxy disk. The scale height of the synchrotron emitting halo depends on the synchrotron lifetime ($\tau_{\rm syn}$), and is expected to be uniform along the extent of the disk except perhaps near the central parts of the galaxies ($\sim$ 1 kpc) or in high density regions. Also, $B(r) \propto l(r)^{-1/(\alpha_{\rm nt}+3)}$ (see Equation 2.17) shows weak dependence of magnetic field on $l(r)$. Therefore, we assume that the path-length through the source to be constant [$l \equiv l(r) = l_0 \simeq 2$ kpc]. The magnetic field thus estimated by us can be scaled by $[2 \times 10^{-2}(K_0+1)/l]^{1/(\alpha_{\rm nt}+3)}$ due to the assumption of $K_0 = 100$ and $l_0 = 2$ kpc.

The 'revised' equipartition formula in Eq. 1 diverges for $\alpha_{\rm nt} \leq 0.5$. Thus for regions where $\alpha_{\rm nt}$ was found to be less than 0.55, mostly in the center and inner arms of NGC 5236 and some parts in the ring of NGC 4736, we used a spectral index of 0.55 to avoid sudden rise in the total field strength. Such regions have high gas densities and perhaps dominated by ionization or bremsstrahlung losses giving rise to flatter $\alpha_{\rm nt}$ (see Longair, 2011). As a result, the magnetic field strength is overestimated in such regions (Lacki & Beck, 2013). The regions of steep spectral index ($\alpha_{\rm nt} > 1$) towards the outer parts of the galaxies arises due to dominant energy losses of CRe. Thus, the energy spectral index between CRe and cosmic ray protons changes, which is assumed to be constant and the same between protons and electron in the equipartition formula. We have therefore set $\alpha_{\rm nt}$ as 1 for such regions. This gives $\sim$6–10 percent lower field strength as compared to steeper $\alpha_{\rm nt}$.

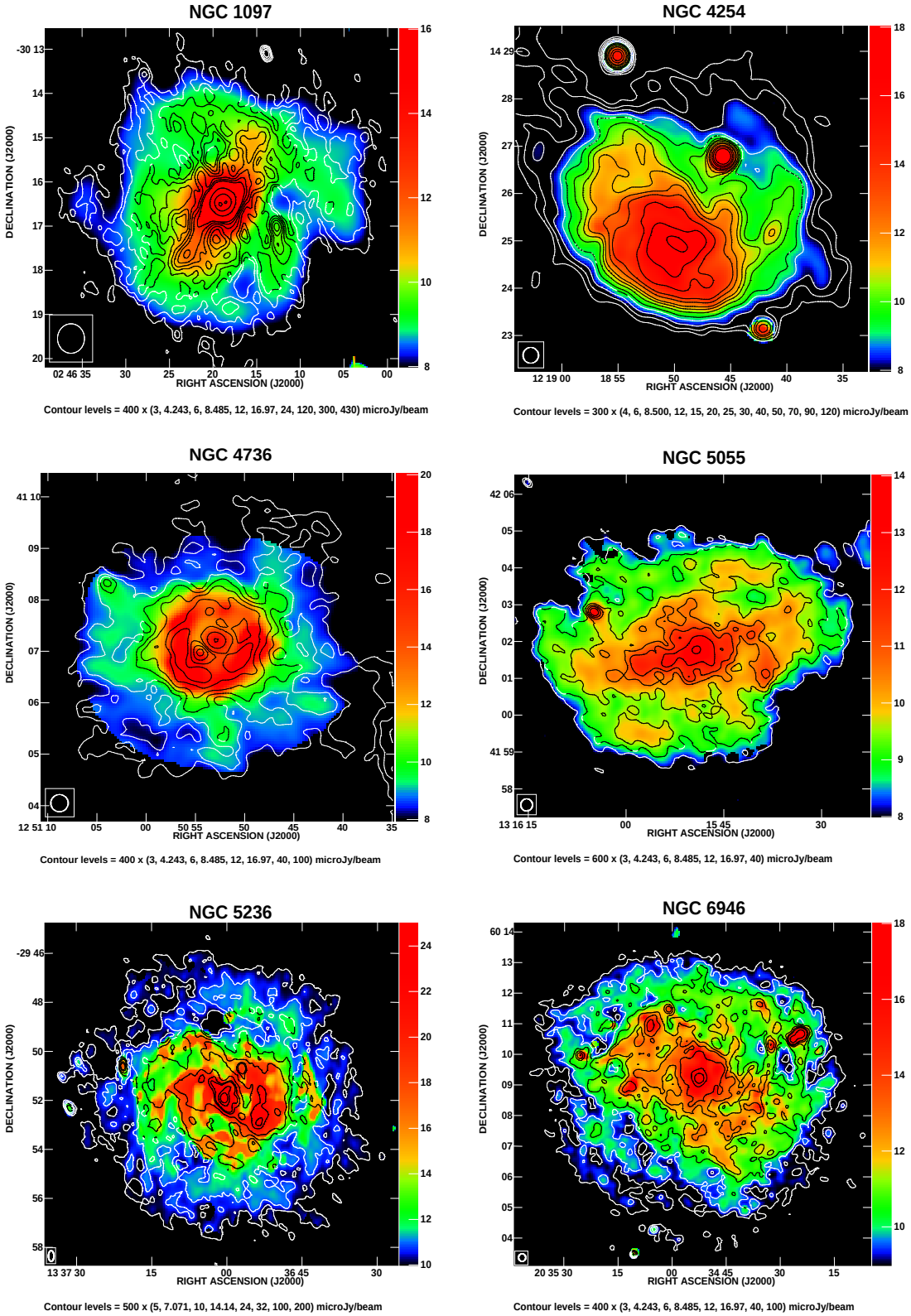

Figure 6.1: The total equipartition magnetic field maps (in μG) for the galaxies NGC 1097, NGC 4254, NGC 4736, NGC 5055, NGC 5236 and NGC 6946. The maps have angular resolution of 40×40, 20×20, 20×20, 20×20, 26×14 and 15×15 arcsec^2 respectively (shown in the bottom left corner). The errors in the central (red) regions was found to be $\sim$ 2 percent, in the disk (green regions) $\sim 5-10$ percent and in the outer parts (blue regions) $\sim 15-20$ percent. Overlaid are the 0.33 GHz contours from Chapter 3 (Basu et al., 2012).

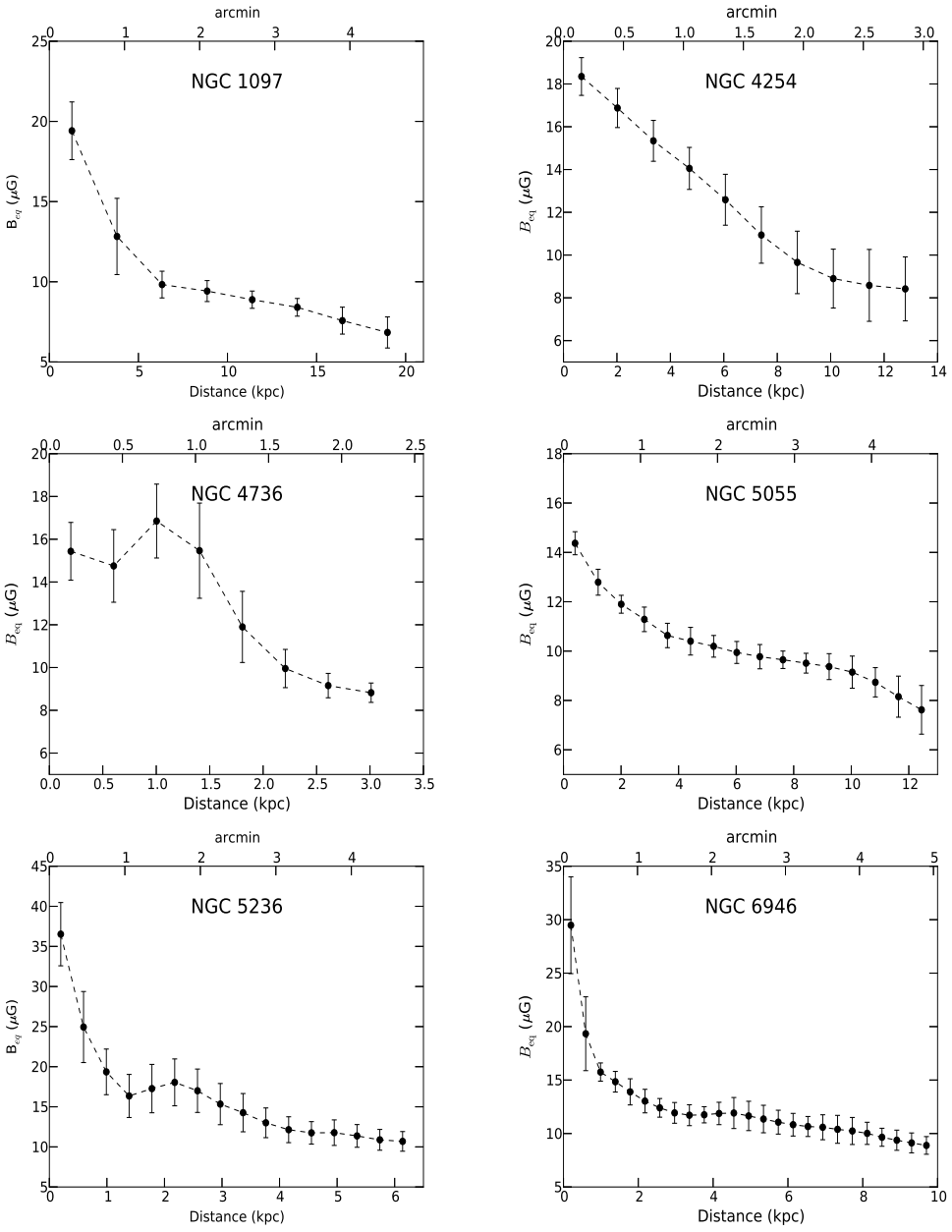

Figure 6.2: Variation of the total equipartition magnetic field strength as a function of galactocentric distance.

Table 6.1: Mean equipartition magnetic fields.

Name	$\langle B_{\rm eq}\rangle$ (μG)	$\langle B_{\rm eq}\rangle_{\rm arm}$ (μG)	$\langle B_{\rm eq}\rangle_{\rm interarm}$ (μG)
NGC 1097	9.0±2.0	9.6±2.2	8.9±2.3
NGC 4254	11.0±2.5	13.4±2.0	11.0±2.4
NGC 4736	9.3±2.1	16.6±2.4	9.5±0.7
NGC 5055	9.5±1.1	10.2±0.6	9.9±0.6
NGC 5236	12.2±2.5	14.6±3.0	12.0±2.4
NGC 6946	10.7±1.8	12.3±1.8	11.2±1.2

Note: The mean magnetic field strength for the galaxies were computed including the low surface brightness diffuse emission and is therefore less than the mean values in arm and interarm regions.

6.2 Results

The estimated 'equipartition' magnetic field strength for the five galaxies, using Eq. 1, are shown in Figure 6.1. The resolution of the maps for each galaxy are tabulated in Table 4.1 and is shown in the lower left corner of each image. Overlaid are the 0.33 GHz contour maps of the galaxies from Basu et al. (2012). The galaxy integrated mean values of magnetic field, $\langle B_{\rm eq}\rangle$, are found to be 9.0 ± 2.0, 11.0 ± 2.5 9.3 ± 2.1, 9.5 ± 1.1, 12.2 ± 3.0 and 10.7 ± 1.8 μG for NGC 1097, NGC 4254, NGC 4736, NGC 5055, NGC 5236 and NGC 6946, respectively (see Table 6.1).

Figure 6.2 shows $B_{\rm eq}$ as a function of galactocentric distance (r) estimated by azimuthal averaging over annuli of one beam width. The field strength are found to be strongest near the central regions with $\langle B_{\rm eq}\rangle \sim 20 - 25$ μG. In the disk, $\langle B_{\rm eq}\rangle$ falls to ~ 15 μG and ~ 10 μG in the outer parts of the galaxy. That is, in most of the cases it is seen that the magnetic field fall by ∼40–50 percent from the center to the edge, similar to what is seen for the Milky Way (Beck et al., 1996).

The errors in the magnetic field strength was estimated using Monte-Carlo method, wherein $\sim 10^4$ random flux density samples were generated assuming Gaussian distribution of error in source flux densities at each frequency. These were used to determine the distribution of $B_{\rm eq}$. Figure 6.3 (top panel) shows the distribution of flux densities at λ90 cm (unfilled histograms) and λ20 cm (gray histograms). The middle panel shows the distribution of $\alpha_{\rm nt}$ determined from the flux density distributions at the two radio frequencies. The bottom panel shows the distribution of the estimated $B_{\rm eq}$. For high signal-to-noise regions ($\gtrsim 10\sigma$, i.e towards the inner parts of the galaxies; left-hand side of Figure 6.3) the distribution of $B_{\rm eq}$ can be modelled as Gaussian. However, for

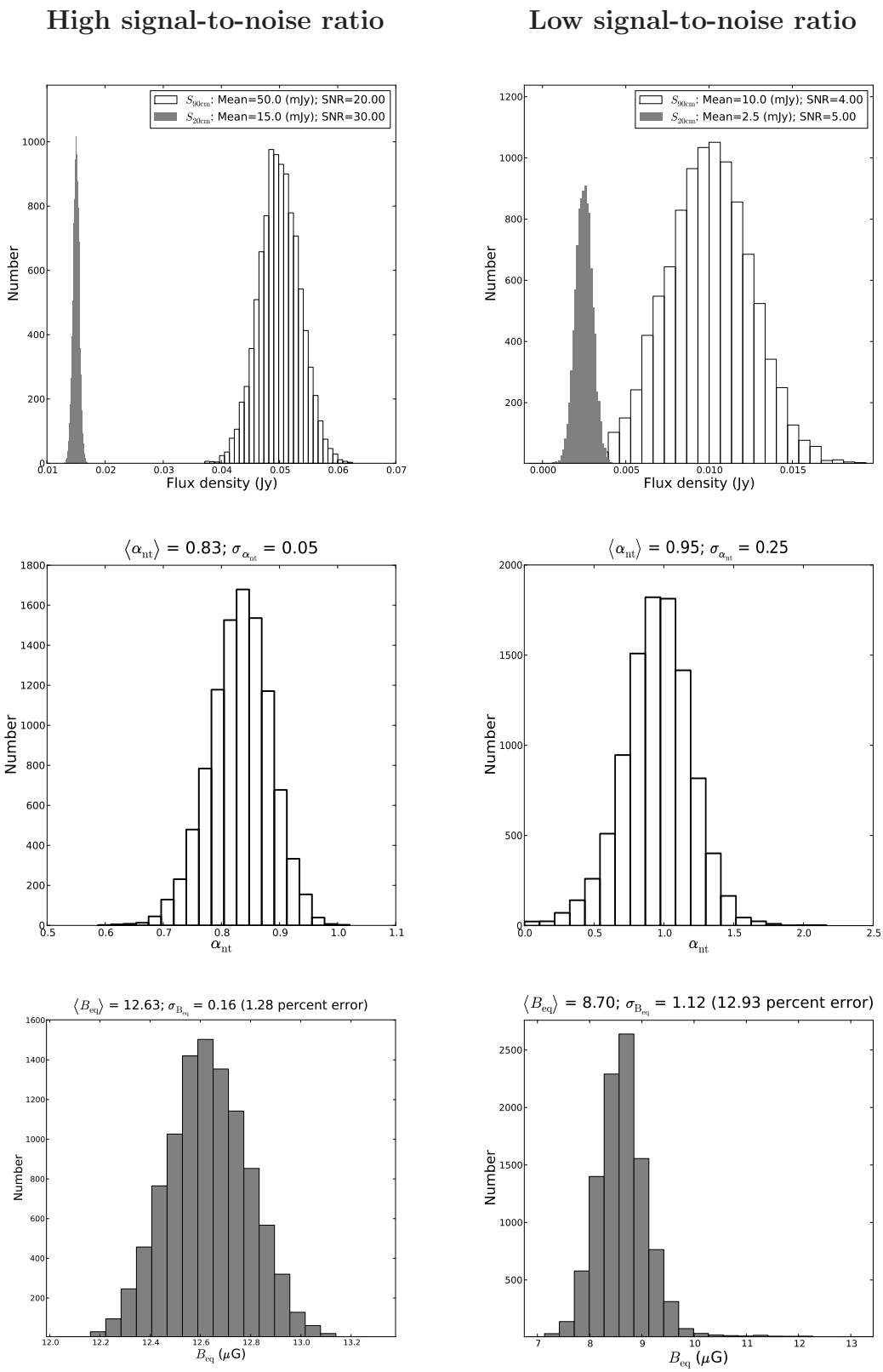

Figure 6.3: Monte-carlo simulation to estimate the error in the estimated $B_{\rm eq}$ for high signal-to-noise ratio (left-hand side) and low signal-to-noise ratio (right-hand side) regions. The top panel shows the 10^4 random flux density sample at λ90 cm (unfilled histogram) and λ20 cm (gray histogram). The middle panel shows the distribution of the $\alpha_{\rm nt}$. Bottom panel shows the distribution of the estimated $B_{\rm eq}$.

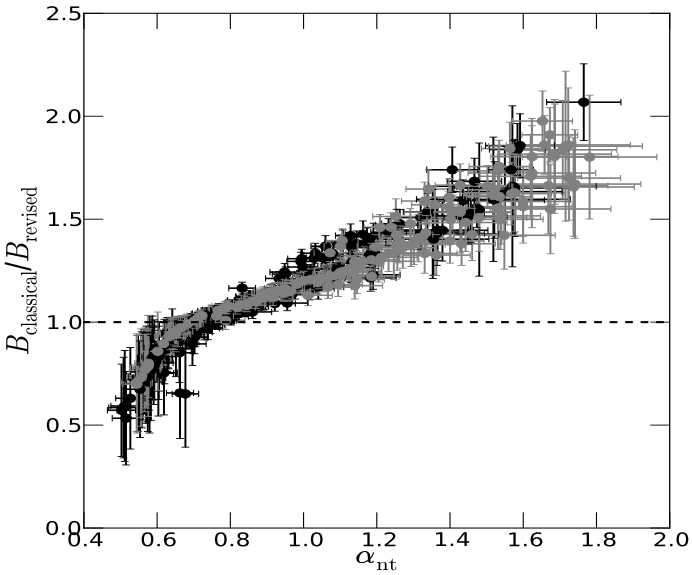

Figure 6.4: Variation of the ratio $B_{\rm classical}/B_{\rm revised}$ with the nonthermal spectral index ($\alpha_{\rm nt}$) determined within regions of $\sim$ 1 kpc for the sample galaxies combined. The black and gray points shows the arms and interarm regions, respectively.

regions with lower signal-to-noise ($\lesssim 5\sigma$, i.e, in the outer parts of the galaxies; right-hand side of Figure 6.3) the distribution has a tail. The error in the total field strength was found to be $\sim$ 2 percent towards the central regions (corresponding to red regions in Figure 6.1), $\sim 5-10$ percent in the disk (green regions in Figure 6.1) and $\sim 15-20$ percent in the outer parts (blue regions in Figure 6.1).

We compared the magnetic field determined using the revised and the classical formula. Figure 6.4 shows the variation of the ratio of magnetic field estimated using classical formula ($B_{\rm classical}$) and revised formula ($B_{\rm revised}$) with nonthermal spectral index, $\alpha_{\rm nt}$, for the six galaxies determined within regions of $\sim$ 1 kpc. The black points are for arms and gray points are for interarms. In the central regions and inner disk where the $\alpha_{\rm nt}$ lies in the range 0.6 to 1, the fields match within $\sim$10 percent. However, in the outer parts of these galaxies where $\alpha_{\rm nt}$ is steeper (> 1.2), the classical equipartition values are overestimated by > 20 percent and increases with steepening of the spectral index to up to 50–60 percent towards the edge. Such a deviation between magnetic fields estimated by the two methods was shown by Beck & Krause (2005), also shown in Figure 2.2. Thus, the magnetic field determined using the classical formula is found

to be constant or increasing as a function of galactocentric distance.

6.2.1 Comparison with existing studies

NGC 1097 was studied in polarization at high resolution that revealed magnetic field in the bar to be aligned with the gas streamlines and thus a good tracer of gas flow (Beck et al., 1999). Strong radio emission is detected from the bar at λ90 cm (Basu et al., 2012), however, due to poor resolution of λ20 cm maps ($\sim$ 40 arcsec), the enhancement of magnetic field in the bar is only about 10–15 percent higher than the disk. In this study, the field at the center is found to be $\sim$ 18 μG and decreases to $\sim$ 10 μG towards the edge. The field in the northern bar is found to be lower than that in the southern bar with $\langle B_{\rm eq} \rangle \sim 9.8$ μG and ~ 12.2 μG respectively. Our estimated field is lower than what was estimated by Beck et al. (2005) perhaps due to their assumption of 500 pc of synchrotron emitting region.

NGC 4254 is located about 1.2 Mpc away in the north-west direction from the center of the Virgo cluster. This galaxy is highly asymmetric with significant diffuse emission originating in the northern region and is more than 1.5 times in extension when compared to the southern side (see Figure 3.3) due to Virgo infall. The magnetic field strength map is also seen to be asymmetric (see Figure 6.1). The field is seen to be highest towards the center $\sim$ 18 μG and falls off to $\sim$ 8 μG towards the edge. Assuming a constant nonthermal spectral index of 1, Chyży (2008) found similar variation of the magnetic field across the galaxy. However, the total magnetic field is significantly higher in the southern than in northern regions. In the southern region, the field strength is $\sim 10 - 15$ μG with mean magnetic field strength of $\sim$ 12 μG. Such strong fields are seen all the way up to the southern edge. In the northern region, the field strengths are generally weak $\sim 6 - 10$ μG with mean field strength of $\sim$ 9 μG. The polarization properties of this galaxy has been studied in detail by Chyży, Ehle & Beck (2007) at 4.86 and 8.46 GHz. They reported high degree of polarization (up to 40 percent and a mean of $\sim$ 24 percent) in the southern ridge. Such enhancement in polarization could be induced by ram pressure effects.

NGC 4736 is a ringed galaxy with no prominent spiral structure from radio through infrared to optical. Polarized radio emission revealed ordered magnetic field in spiral shape possibly amplified by large-scale MHD dynamo (Chyży & Buta, 2008). They report mean total magnetic field of 17 μG, slightly higher than our estimate of 14 μG within a region of $\sim$ 3.5 arcmin (corresponds to inner 2.3 kpc radius). From our

map (see Figure 6.1), the total magnetic field in the center is found to be $\sim$ 18 μG while in the ring, the field strength is 15–25 μG with an average total field strength of $\sim$ 16.5 μG close to Chyży & Buta (2008) . Beyond the ring the magnetic field falls off to about 8–10 μG at a distance of $\sim$ 3 kpc.

NGC 5055 is a flocculent spiral galaxy and lacks organized spiral structure when seen in optical. Polarization observations revealed regular spiral magnetic fields believed to have been generated from turbulent dynamo action (Knapik et al., 2000). They estimated a mean equipartition magnetic field of 9.2 μG close to our value of 9.5 μG. Of all the galaxies in the sample, NGC 5055 has the weakest total magnetic field of $\sim$ 14.5 μG in the center and falls off to about 10 μG in the disk and $\sim$ 8 μG towards the edge. No distinct spiral structure has been seen in the map of total magnetic field.

NGC 5236 (M83) is a starburst galaxy with uniform magnetic field seen in the outer parts of the galaxy and lower degree of uniformity towards the inner regions hosting star formation (Neininger et al., 1993, 1991; Sukumar & Allen, 1989). Towards the center and inner spiral arms which harbors the starburst (Calzetti et al., 1999), the $\alpha_{\rm nt}$ was found to be flatter and lies in the range 0.4–0.55. For those regions we have assumed the value of $\alpha_{\rm nt}$ as 0.55 to avoid any sudden discontinuities. The magnetic field strengths are overestimated in such regions. We found a mean total field strength of 24 μG in the central 1 kpc regions. The magnetic field is found to be strong in the arms with strength $\sim$15–20 μG and falls to $\sim$ 10 μG in the interarms and towards the edge. The mean total field in the galaxy is found to be 12.2$\pm$2.5 μG, close to what was estimated by Neininger et al. (1991) within measurement errors.

Magnetic field in NGC 6946 was studied in detail by Beck (2007). The total magnetic field strength was found to be $\sim$ 20 μG in the spiral gas arms, close to what is estimated by us. In the arms turbulent fields dominate, while in the interarms large scale regular field was seen with high degree of polarization (30–60 percent) referred as the 'magnetic arms' by Beck (2007). From our maps (see Figure 6.1), in the northern (roughly centered at RA = $20^{\rm h}34^{\rm m}52^{\rm s}$, DEC = $+60^\circ11'59''$ J2000) and southern (roughly centered at RA = $20^{\rm h}34^{\rm m}33^{\rm s}$, DEC = $+60^\circ06'46.75''$ J2000) magnetic arms, the average field is found to be $\sim$ 11 μG, which is just 10–15 percent stronger than other interarm regions, and this result is at $\gtrsim 3\sigma$ significance. The 'circular hole' of $\sim$ 1 kpc diameter seen in the galaxy with low radio emission at RA = $20^{\rm h}34^{\rm m}20^{\rm s}$ and Dec. = $+60^\circ09'40''$ (J2000) is seen to have low magnetic field ($\sim$ 8.5 μG) as compared to other parts and is $\sim$ 30 percent lower than the surrounding regions.

6.2.2 Magnetic fields in arms and interarms

We studied the variation of magnetic field along arm and interarm regions for the galaxies NGC 1097, NGC 4254, NGC 5055, NGC 5236 and NGC 6946 after correcting for the radial variations. This was not possible for the ringed galaxy NGC 4736, which do not have any prominent arm. Arms and interarm regions were chosen using the Spitzer $\lambda 24$ μm images after smoothing to the resolution of nonthermal maps. For each of the galaxies, the beginning of arm or interarm were chosen leaving the central ~ 1 kpc region. We determined magnetic field within an area of one synthesized beam ensuring no overlap between adjacent beams. Each beam corresponds to $\sim$0.4 to 2 kpc at the distance of the galaxies (see Table 4.1). The galaxy NGC 5055, where the arm and interarm are not clearly distinguishable, the mean field in arm was only about 5 percent stronger than that in the interarm. For the other galaxies the mean magnetic field in the arms are stronger by 10–15 percent (see Table 6.1). Overall, the mean magnetic field strength in the arm is higher than that in the interarm by 12 ± 3 percent, however, in certain regions it could be higher by up to 40 percent. We note that, when magnetic fields are higher in the arms, the limited telescope resolution suppresses the observed field strength in the arms and increases that in the interarm regions. The same effect is caused by larger CRe diffusion length at $\lambda 90$ cm, so that more radio emission is observed in the interarm regions. Thus, the differences seen in the magnetic field strength between arm and interarm regions are lower limits.

In Figure 6.5, we study the variation of the relative magnetic field strength $B_{\rm eq}(r,d)/B_{\rm eq}(r)$, where, r is the galactocentric distance and d is the linear distance measured from the center along the corresponding arm or interarm. We consider only those pixels that are above 4σ map rms noise in total intensity. In the figure, the black circles and the gray squares represent arms and interarms respectively. After correcting for the radial variation, the magnetic field do not change significantly along arm or interarm. The mean value of $B_{\rm eq}(r,d)/B_{\rm eq}(r)$ in the arm is found to be 1.03 ± 0.04 and 0.97 ± 0.04 in the interarms for all the galaxies combined. Due to our selection of high signal to noise regions, the contrast between arm and interarm that is seen in the total magnetic field maps disappears.

6.2.3 Radial scale lengths

It is believed that CRe originates from supernova explosions of OB stars found in HII complexes, i.e., regions of star formation. These CRe then propagate away to larger

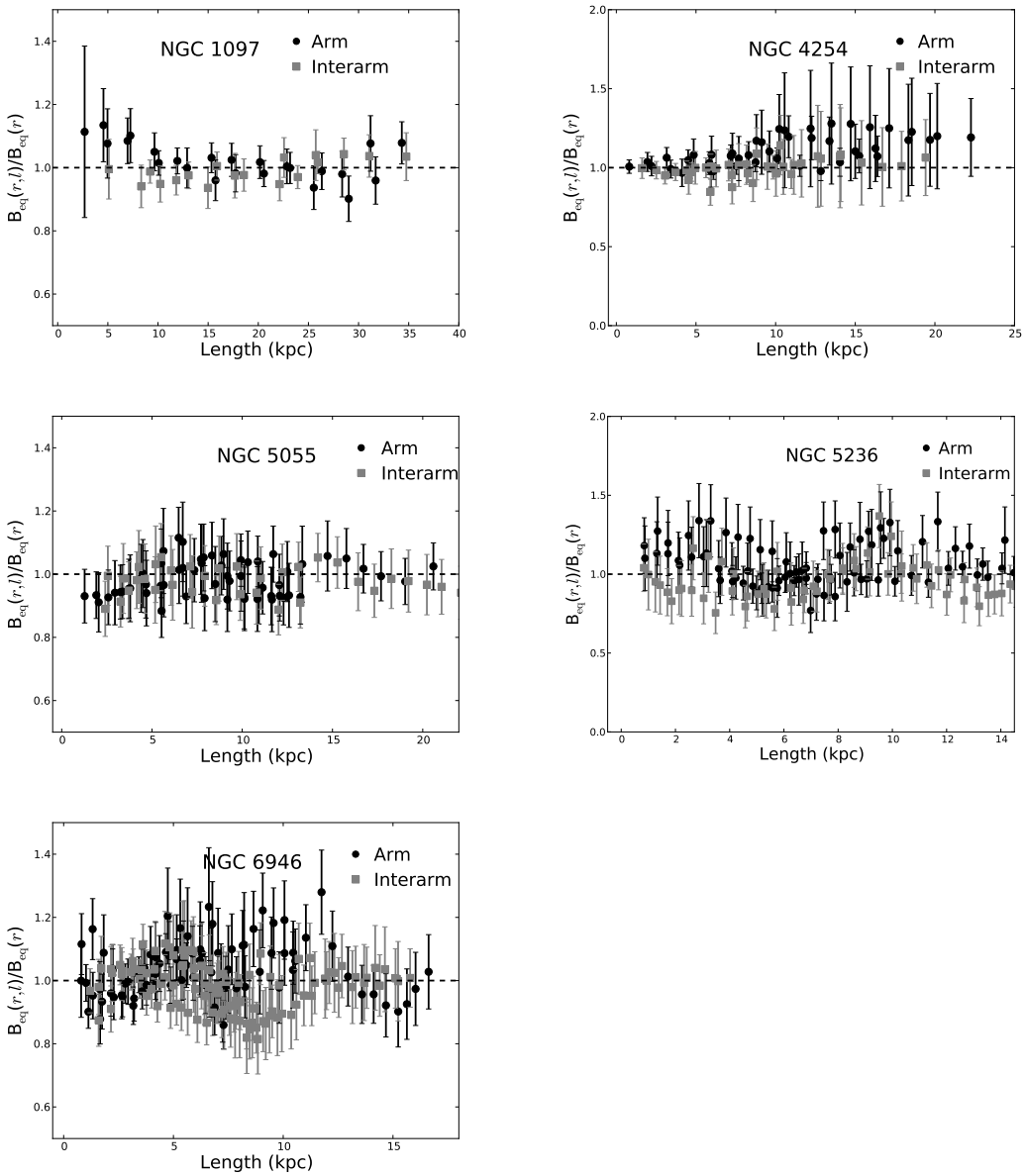

Figure 6.5: Variation of total magnetic field strength along arm and interarm after correcting for the galactocentric variation as in Figure 6.2.

Table 6.2: Exponential scale lengths (l_0) of ISM components.

Component	NGC 1097 (kpc)	NGC 4254 (kpc)	NGC 4736 (kpc)	NGC 5055 (kpc)	NGC 5236 (kpc)	NGC 6946 (kpc)
$I_{\rm nt,20cm}$	2.7±0.3	3.5±0.2	0.95±0.10	3.2±0.1	2.5±0.3	4.0±0.3
$I_{\rm nt,90cm}$	4.8±0.9	4.3±0.2	1.3±0.3	6.2±0.5	4.1±0.4	5.3±0.4
$B_{\rm eq}$	13.0±2.9	13.6±0.7	5.0±0.3	12.4±0.5	>7.7	17.7±1.0
$\Sigma_{\rm gas}$	–	3.6±0.3	0.95±0.04	4.25±0.26	2.2±0.1	3.6±0.2

distances in galaxies giving rise to larger radial distribution of synchrotron emission than that of CRe sources and gas (see Beck, 2007; Tabatabaei et al., 2007b). The total intensity radio maps at λ90 cm appears to be significantly smoother than that at λ20 cm (see Basu et al., 2012). The former mainly originates from older ($\sim 10^8$ yr) population of CRe that diffuses farther away from their formation sites than that at λ20 cm. We estimate the exponential scale length of nonthermal emission at λ20 cm ($I_{\rm nt,20cm}$) and λ90 cm ($I_{\rm nt,90cm}$), total equipartition magnetic fields and surface mass density of total gas ($\Sigma_{\rm gas}$) to explore the effect of diffusion of CRe. $\Sigma_{\rm gas}$ is computed from atomic and molecular hydrogen surface mass density (see Appendix A). The scale lengths (l_0) were obtained by fitting a function $f(r) = f_0 \exp(-r/l_0)$ to the radial profiles shown in Figure 6.7 leaving aside the central bulge. For the ringed galaxy NGC 4736, the scale lengths were computed leaving aside the ring. The scale lengths obtained are summarized in Table 6.2.

The scale length of the nonthermal emission ($l_{\rm nt}$) at λ90 cm was found to be higher than that at λ20 cm. This is caused due to higher diffusion scale lengths of low energy ($\sim$ 1.5 GeV) CRe at λ90 cm as compared to higher energy ($\sim$ 3 GeV) CRe at λ20 cm (Basu, Roy & Mitra, 2012) in a typical galactic magnetic field of ~ 10 μG. In the simple case of energy dependent diffusion of CRe, the diffusion length ($l_{\rm diff}$) after time τ is given by, $l_{\rm diff} \sim (D\ \tau)^{0.5}$. Here, D is the diffusion coefficient assumed to be constant, and is $\sim 10^{28}$ cm^{2}s^{-1}. We assume the diffusion time to be same as the synchrotron cooling timescales ($t_{\rm syn}$) given by, $t_{\rm syn} = 8.35 \times 10^9\ (E_{\rm CRe}/{\rm GeV})^{-1}\,(B_{\rm eq}/\mu G)^{-2}$ yr, where, $E_{\rm CRe}$ is the energy of the electrons. The expected diffusion length for the galaxies at λ90 cm and λ20 cm are $\sim$ 1.4 kpc and $\sim$ 1 kpc respectively, i.e, $l_{\rm diff,90cm}/l_{\rm diff,20cm} = (E_{\rm CRe,90cm}/E_{\rm CRe,20cm})^{-0.5} \sim 1.4$. CRe can also propagate by the streaming instability at the velocity of Alfvén wave in the ionized galactic medium and the propagation distance is given by, $l_{\rm A} = v_{\rm A} t_{\rm syn}$. Here, $v_{\rm A}$ is the Alfvén velocity assumed to be $\sim$ 50 km s^{-1}. In this scenario, the propagation distance at λ90 cm and λ20 cm are $\sim$1

kpc and ∼2 kpc respectively, i.e., $l_{\rm A,90cm}/l_{\rm A,20cm} = (E_{\rm CRe,90cm}/E_{\rm CRe,20cm})^{-1} \sim 2$. From our data, the ratio of scale length of nonthermal emission at λ90 cm and λ20 cm, i.e, $l_{\rm nt,90cm}/l_{\rm nt,20cm}$ are 1.77 ± 0.38, 1.24 ± 0.08, 1.37 ± 0.29, 1.92 ± 0.17, 1.64 ± 0.25 and 1.31 ± 0.15 for NGC 1097, NGC 4254, NGC 4736, NGC 5055, NGC 5236 and NGC 6946 respectively. For 3 of the galaxies the increase in the estimated $l_{\rm nt}$ between λ90 and λ20 cm is larger than that expected from simple diffusion estimates and is consistent with streaming with Alfvénic velocity. However, the mean value of the ratio of scale lengths at the two frequencies is 1.54 ± 0.35 which is closer to 1.4. More data are required to significantly claim any evidence of Alfvén streaming.

The scale length of nonthermal emission at λ20 cm for NGC 6946 is similar to what was found by Walsh et al. (2002) and Beck (2007). The nonthermal scale length is related to scale length of magnetic field (l_B) as $l_B = l_{\rm nt}(3 + \alpha_{\rm nt})$ under the assumption of equipartition of energy between magnetic field and cosmic ray particles. For the galaxy NGC 5236, l_B is found to be comparatively smaller than other galaxies and is only ∼ 3 times than that of $l_{\rm nt}$ at λ20 cm and ∼1.9 times at λ90 cm. This is perhaps the effect of magnetic field strength being overestimated towards the inner parts of the galaxy, where $\alpha_{\rm nt} \leq 0.5$ (see Section 6.1.1). Thus, the estimated l_B for NGC 5236 is lower than the actual value. The scale length of the magnetic field for NGC 6946 is found to be slightly higher than what was estimated by Beck (2007). This is likely to be caused due to their assumption of a constant $\alpha_{\rm nt}$ throughout the galaxy and use of nonthermal emission at λ20 cm which has a smaller $l_{\rm nt}$ as compared to our λ90 cm maps. Dynamo theory predicts field amplification up to energy equipartition between magnetic field and turbulent gas such that, $l_{\rm B}/2 \approx l_{\rm gas}$. Surprisingly, for all the galaxies, the scale length of the magnetic field is much larger than that of the gas surface density, i.e., the magnetic field energy density systematically dominates over turbulent gas energy density towards outer parts of the galaxies where star formation activity and thus turbulence driven by supernove explosions are low. The field in such regions is perhaps amplified by dynamo driven by magneto-rotational instability (Rüdiger & Hollerbach, 2004; Sellwood & Balbus, 1999) which can amplify magnetic field beyond equipartition levels.

The scale length of total gas surface density ($l_{\rm gas}$) is found to be smaller than that of the nonthermal emission. However, $l_{\rm gas}$ is close to $l_{\rm nt}$ at λ20 cm and much smaller than $l_{\rm nt}$ at λ90 cm, suggesting the λ20 cm nonthermal emission is a better tracer of star forming activity than at λ90 cm, wherein the later mostly traces the older population of CRe which are well mixed.

6.3 Discussions

6.3.1 Is synchrotron intensity an indicator of magnetic field?

6.3.1.1 Slope of the radio–FIR correlation

Simulations of MHD turbulence in the ISM revealed, under conditions of equipartition, the magnetic field (B) and the gas density ($\rho_{\rm gas}$) are coupled as $B \propto \rho_{\rm gas}^{\kappa}$, where $\kappa \sim 0.4 - 0.6$ (see e.g., Fiedler & Mouschovias, 1993; Groves et al., 2003). The slope of the well known radio–far infrared (FIR) correlation was used to determine κ for four of the galaxies at scales of ~ 1 kpc (Basu, Roy & Mitra, 2012) using synchrotron emission at λ90 cm and λ20 cm and FIR emission at λ70 μm. The estimated value of κ was found to be 0.51 ± 0.12, indicating energy 'equipartition' among magnetic field and kinetic energy of gas due to turbulent motions. However, in this method equipartition between magnetic field and cosmic ray particles is assumed a-priori. The validity of this assumption can be checked from the dispersion seen in the radio–FIR correlation and our estimated values of the magnetic fields.

6.3.1.2 Dispersion of the radio–FIR correlation

Dispersion of quantity 'q' defined as $\log_{10}(I_{\rm FIR}/I_{{\rm nt},\nu})$ is widely used as a measure of the tightness of the radio–FIR correlation. Where, $I_{\rm FIR}$ is the FIR flux density and $I_{{\rm nt},\nu}$ is the nonthermal radio flux density at frequency, ν. The far infrared flux density ($I_{\rm FIR}$) can be written as, $I_{\rm FIR} \propto n_{\rm UV} Q(\lambda, a) B(T_{\rm dust})$, where $n_{\rm UV}$ is the number density of the UV photons responsible for dust heating, $Q(\lambda, a)$ is a wavelength (here $\lambda = 70$ μm) dependent absorption coefficient of dust grains of radius a (Alton et al., 2004; Draine & Lee, 1984). $B(T_{\rm dust})$ is the Planck function for dust emitting at temperature $T_{\rm dust}$. The flux density at radio frequency ν, can be written as $I_{{\rm nt},\nu} \propto n_{{\rm CRe},\nu} B^{1+\alpha_{\rm nt}}$, where, $n_{{\rm CRe},\nu}$ is the number density of cosmic ray electrons (CRe) emitting at a frequency ν and B is the actual magnetic field. From the above, the ratio of FIR and radio flux density is, $I_{\rm FIR}/I_{{\rm nt},\nu} \propto (n_{\rm UV}/n_{{\rm CRe},\nu})(1/B^{1+\alpha_{\rm nt}})$, assuming same dust properties throughout the galaxy and $T_{\rm dust}$ is seen to remain constant throughout the galaxy (see e.g. Basu et al., 2012; Tabatabaei et al., 2007b). Hummel (1986) showed that the cumulative frequency distribution of $I_{\rm FIR}/I_{{\rm nt},\nu}$ and that of $B_{\rm eq}^{1+\alpha_{\rm nt}}$ follows each other indicating energy 'equipartition' between magnetic field and cosmic ray particles to hold good and thus $B_{\rm eq}$ is close to B. In our case, for each of the galaxy, we determine the quantities $I_{70\mu{\rm m}}/I_{{\rm nt},20{\rm cm}}$ and $B_{\rm eq}^{1+\alpha_{\rm nt}}$ within a region of ~ 1 kpc and normalized them

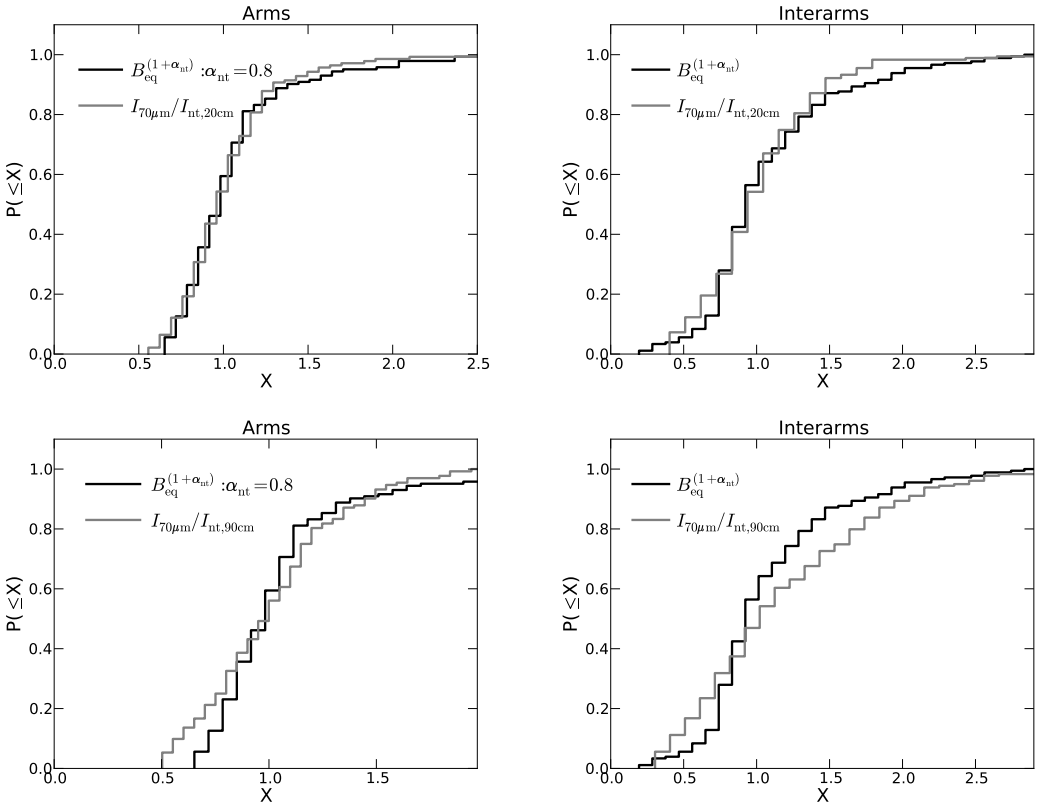

Figure 6.6: The cumulative distribution function of $X = I_{70\ \mu\rm m}/I_{\rm radio}$ (shown in gray) and $X = B_{\rm eq}^{(1+\alpha_{\rm nt})}$ (shown in black) for arm (left panel) and interarm (right panel). The top panel is at λ20 cm and bottom panel is at λ90 cm. In the arm we use $\alpha_{\rm nt} = 0.8$ while in the interarm $\alpha_{\rm nt}$ is determined for each of the corresponding region (see text for details).

with their respective median values. In Figure 6.6 we plot these median normalized cumulative distribution function of $I_{70\mu m}/I_{nt,20cm}$ (shown in gray) and $B_{eq}^{1+\alpha_{nt}}$ (shown in black) for all the galaxies together. The left and right panels show the distribution in the arm and interarm regions respectively. In the arm regions, α_{nt} do not change significantly, we assumed a constant value of 0.8. However, α_{nt} varies significantly in the interarm regions, and we have used the observed values of α_{nt} for each region from Basu et al. (2012).

At λ20 cm, the dispersion in the quantity $I_{70\mu m}/I_{nt,20cm}$ is similar to the dispersion in $B_{eq}^{1+\alpha_{nt}}$ for both arms and interarm regions determined at spatial scales of $\sim$ 1 kpc. Thus at scales of $\sim$1 kpc, the variations in $I_{70\mu m}/I_{nt,20cm}$, i.e., dispersion seen in the quantity 'q' is caused due to variations in the magnetic field, where the magnetic field is represented by B_{eq}. Thus, B_{eq} (or a constant multiple of it) is a good representative of the actual magnetic field, B.

However, at λ90 cm, the dispersion in $I_{70\mu m}/I_{nt,90cm}$ is $\sim$20 percent higher than that of $B_{eq}^{1+\alpha_{nt}}$ for the interarm regions. At λ90 cm the low energy ($\sim$ 1.5 GeV) CRe propagate to farther distances from the arms into the interarms, which has the effect of increasing the dispersion. We note that equipartition assumption is valid only at scales larger than the diffusion length, which is better fulfilled at λ20 cm than at λ90 cm.

6.3.2 Energy density in magnetic field and gas

Magnetic energy is expected to be in equipartition with ISM turbulent energy (Cho & Vishniac, 2000; Crutcher, 1999; Groves et al., 2003). In Section 3, we found that the magnetic field falls off as a function of galactocentric distance and had a larger scale length than that of the gas surface density. Here, we compare the magnetic field energy density ($U_{mag} = B_{eq}^2/8\pi$) with that of the ISM energy density from kinetic energy of gas due to turbulent motions ($U_{turb,gas}$), thermal energy density of warm ionized gas (U_{ion}) and total neutral (atomic; $U_{th,HI}$ + molecular; U_{th,H_2}) gas at spatial scales of 0.4 – 0.9 kpc, except for NGC 5236 for which the spatial resolution is $\sim$ 1.2 kpc (see Appendix A for details). $U_{turb,gas}$ is estimated from the surface mass density maps of atomic and molecular hydrogen, using $U_{turb,gas} = 1.36(U_{turb,HI} + U_{turb,H_2})$. The factor 1.36 is to account for the presence of Helium and $U_{turb,HI,H_2} = (1/2)(\Sigma_{HI,H_2}/h_{HI,H_2})v_{turb}^2$, where, Σ_{HI,H_2} are the surface mass density of atomic (HI) and molecular (H_2) gas. v_{turb} is the velocity of the turbulent gas, assumed to be $\sim$ 9 km s^{-1} for HI and $\sim$ 6 km s^{-1} for H_2

(Combes & Becquaert, 1997; Kasparova & Zasov, 2008; Sellwood & Balbus, 1999) and $h_{\rm HI,H_2}$ are the line of sight depth of atomic and molecular gas assumed to be $\sim$ 400 pc and $\sim$ 300 pc respectively. The surface mass densities were calculated using moment-0 maps of CO and HI line emission (see Appendix A for details).

The thermal energy densities of warm ionized gas and neutral gas were computed using, $U_{\rm th} = \frac{3}{2}\langle n \rangle kT$. Here, $\langle n \rangle$ is the mean number density, k is the Boltzmann constant and T is the temperature. For the warm ionized gas, the mean number density of thermal electrons $\langle n_{\rm e} \rangle$ was calculated from the emission measure (EM) maps, such that, $\langle n_{\rm e} \rangle \approx [EM\ f_{\rm d}/h_{\rm ion}]^{1/2}$. EM was determined from de-reddened Hα maps using Equation 9 in Valls-Gabaud (1998) (see Basu et al., 2012, for details). We assumed a constant filling factor ($f_{\rm d}$) of $\sim$5 percent and scale height ($h_{\rm ion}$) of the ionized medium as 1 kpc (Hoopes, Walterbos & Rand, 1999; Wang, Heckman & Lehnert, 1997). The temperature, T_e was assumed to be 10^4 K. To estimate the energy density of molecular ($U_{\rm th,H_2}$) and atomic ($U_{\rm th,HI}$) gas, the number densities were determined from the corresponding surface mass density maps assuming a constant scale height as discussed above. We assumed a constant temperature of $\sim$ 50 K for molecular gas and $\sim$ 100 K for atomic gas.

In Figure 6.7 we study the variation of energy density of magnetic field ($U_{\rm mag}$; shown in black diamonds), kinetic energy of total gas ($U_{\rm turb,gas}$; shown in blue triangles) and thermal energy density of ionized gas ($U_{\rm ion}$; shown in red triangles), molecular gas ($U_{\rm th,H_2}$; shown in gray circles) and atomic gas ($U_{\rm th,HI}$; shown in gray squares) as a function of galactocentric distance for the galaxies NGC 4736, NGC 5055, NGC 5236 and NGC 6946. The galaxy NGC 1097 is not used in this analysis due to non-availability of data tracing atomic and molecular gas. The energy density of the warm ionized gas is found to be about two orders of magnitude lower than that of magnetic field and kinetic energy of turbulent gas. For neutral gas, the thermal energies are about 3 orders of magnitude less. The energy density of magnetic field, turbulent energy of total gas, thermal energy of warm ionized gas and neutral gas matches well with Beck (2007) for the galaxy NGC 6946. However, due to simplistic assumption for $\alpha_{\rm nt} \sim 1.0$ throughout the galaxy, the total magnetic field may be underestimated in Beck (2007), specially in the inner regions where $\alpha_{\rm nt}$ is smaller than 0.7.

In Figure 6.8 we study the variation of the ratio of magnetic field energy density and total ISM gas energy density ($U_{\rm gas}$) estimated at spatial scales of $\sim$0.4–1.2 kpc depending on the distance of the galaxies. $U_{\rm gas}$ was computed as, $U_{\rm gas} = U_{\rm turb,gas} + U_{\rm ion} + 1.36(U_{\rm th,HI} + 2U_{\rm th,H2})$. The black and gray symbols denote arms and interarms

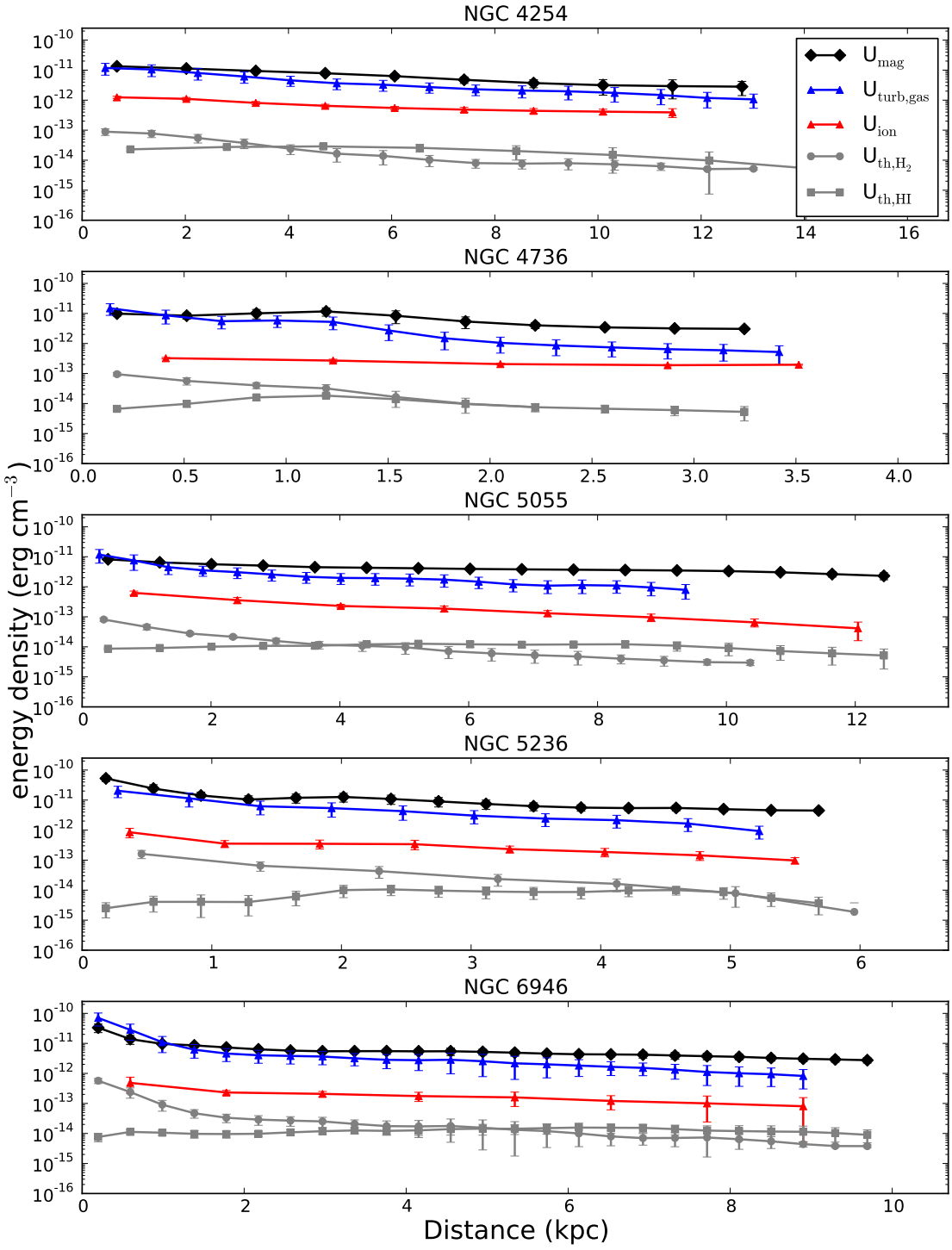

Figure 6.7: Energy densities in various ISM phases as a function of galactocentric distance. Black lines shows the magnetic field energy density ($U_{\rm mag}$), the blue lines shows the kinetic energy density of total neutral gas due to turbulent motion ($U_{\rm turb,gas}$), the red lines shows the thermal energy density of warm ionized gas ($U_{\rm ion}$), the gray lines with dots and squares shows the thermal energy density of atomic and molecular gas ($U_{\rm th,HI}$ and $U_{\rm th,H_2}$) respectively.

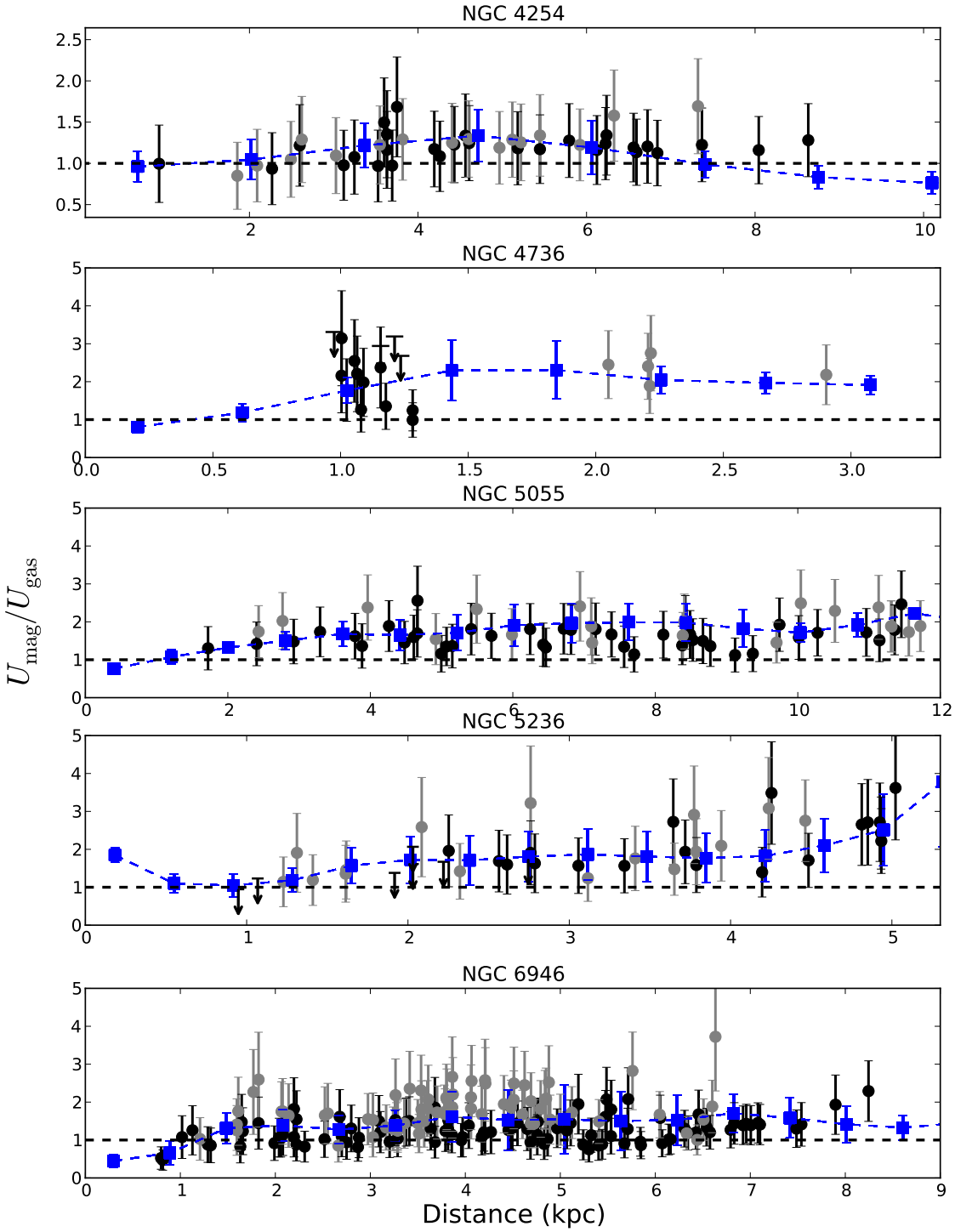

Figure 6.8: The ratio of energy density in magnetic field and total ISM gas energy density ($U_{\rm gas} = U_{\rm turb,gas} + U_{\rm ion} + U_{\rm th,neutral}$) at scales of $\lesssim$ 1 kpc as a function of galactocentric distance. The black and gray symbols are for arm and interarm regions respectively. The blue squares shows the radially averaged value of the ratio determined within annulus of one one synthesized beam width.

respectively. The blue squares show the radially averaged value of the ratio determined within annulus of one beam width. Pixels more than 4σ in gas density were considered for this analysis.

The ratio of total ISM gas energy density and magnetic field are found to be almost constant throughout the galaxies except for a systematic offset from unity due to our assumed constant values of scale heights and velocity dispersion. After dividing by the mean values of the ratio for each of the galaxies, the ratio has a dispersion less than ~ 30 percent for arms and interarms of the galaxies, indicating energy/pressure balance between magnetic field and gas. For the galaxy NGC 6946, we observe that the ratio of the interarm regions to be higher than that in the arms by a factor 1.47 ± 0.11, i.e., magnetic field energy dominates over the turbulent gas energy. Overall, this difference is not significant for other galaxies, but for an adjacent arm-interarm, the ratio in the interarm could be higher by more than 50 percent than the arm. However, interestingly for the galaxy NGC 4254, unlike other galaxies, magnetic energy is seen to dominate in the southern arm of the galaxy when compared to other arms. This region is perhaps affected by ram pressure effects where the magnetic fields may be enhanced due to compression.

From our data we found that as we move from the center to the disk to the edge of the galaxies, magnetic field energy systematically dominates over the total ISM energy density. However, this trend reduces significantly once we consider only the high signal-to-noise regions ($> 4\sigma$) as is shown by the blue points in Figure 6.8. Such a trend may be present for the galaxy NGC 5236 which has the worst angular resolution of 55 arcsec (see Appendix A) and requires higher resolution CO maps that is currently unavailable.

Magnetic fields in galaxies are amplified by two major processes, firstly the small scale fields are amplified by field line stretching and twisting due to turbulent motions of gas (small-scale dynamo) and secondly, large-scale amplification due to large-scale dynamo action. In the previous case, magnetic field and gas are closely coupled such that the magnetic field is amplified by transfer of kinetic energy from gas. The fields can be amplified up to equipartition levels (Cho & Vishniac, 2000; Groves et al., 2003). This would result in small scale turbulent fields with low degree of polarization in regions of high gas density, i.e, the spiral arms. This is indeed observed in many of the galaxies. In NGC 6946 only 1–5 percent of the emission is polarized in the inner spiral arms (Beck, 2007). In M51, turbulent magnetic field dominates in arms (Fletcher et al., 2011). In NGC 5236, low degree of uniform magnetic field is seen in the spiral arms in

inner parts of the galaxy (Neininger et al., 1993). In NGC 4736, comparatively lower degree of polarization is seen in the star forming ring than in the outer parts (Chyży & Buta, 2008). Our results show that in the gaseous arms, the magnetic field energy density and the energy density in gas to be similar and do not vary by more than 30 percent throughout the galaxies. This indicates that in the arms the magnetic field is perhaps amplified by field line stretching due to turbulent gas motions driven by star formation.

In the interarms and towards the outer parts, many galaxies show higher degree of ordered magnetic field caused by large scale dynamo action (see e.g. Beck, 2007; Beck et al., 1996; Chyży & Buta, 2008, and references therein). For NGC 6946, where ordered fields are observed in the interarm regions, it is thought that finite time dynamo relaxation causes a phase shift between magnetic and gas/star forming spiral arms, such that magnetic arms lags (Chamandy, Subramanian & Shukurov, 2013). Magnetic field energy dominating over the turbulent gas energy thus helps maintaining this field orderness in interarm regions and outer parts of the galaxies. For this galaxy, Walsh et al. (2002) found the regular magnetic field (using polarized emission at $\lambda 6$ cm) to trace regions of low star formation efficiency and coincides with the regions where the ratio was found to be significantly higher, suggesting insufficient energy in turbulent gas to amplify the turbulent magnetic field. Magneto-rotational instability may be the driving force to amplify the fields in such regions and towards outer parts of the galaxies where there is less turbulence caused by supernovae (Rüdiger & Hollerbach, 2004; Sellwood & Balbus, 1999). A detailed and sensitive study of the magnetic field properties and structure is essential to understand any role of such mechanism for magnetic field amplification towards outer parts of galaxies.

6.4 Summary

We have measured total magnetic fields in five nearby normal galaxies, NGC 1097, NGC 4736, NGC 5055, NGC 5236 and NGC 6946, assuming equipartition of energy between cosmic ray particles and magnetic fields. In this study, magnetic fields were probed at sub-kpc scales except for NGC 1097, for that it was 2.8 kpc.

- The strengths of the total magnetic field decreases by $\sim 40 - 50\%$ from center to edge of the galaxies. The field changes by at least 15% between arms and interarms and do not change significantly along them after correcting for the

radial variation.

- Our study shows synchrotron intensity to be a good tracer of the total magnetic field in galaxies. 'Equipartition' of energy between magnetic field and cosmic ray particles hold well at kpc scales for all the galaxies.

- The estimated energy densities of magnetic field and gas were seen to be within a factor $\lesssim$2 in the arms and interarms at sub-kpc scales implying magnetic field to play important role in pressure balance of the ISM. The ratio $U_{\rm mag}/U_{\rm gas}$ is found to be roughly constant along radius.

- The energy density of the magnetic field was found to be larger than that of the kinetic energy density due to turbulent motion of gas in the interarm regions, particularly for NGC 6946, and in outer parts in general. Large scale dynamo action could maintain the magnetic field in such regions.

Chapter 7

Conclusion

We have studied seven nearby normal galaxies namely NGC 1097, NGC 3034, NGC 4254, NGC 4736, NGC 5055, NGC 5236 and NGC 6946 using the Giant Meterwave Radio Telescope (GMRT) at 0.33 GHz. The galaxies are observed with angular resolution better than ~ 20 arcsec (corresponding to linear scale of about 0.4–1 kpc) making them the highest resolution observations ever done at this frequency. The rms noise of $\sim 250 - 500$ μJy beam^{-1} for these galaxies at 0.33 GHz is $\sim$10 times better than the previous studies at this frequency.

For six of these galaxies (except NGC 3034), using dust extinction-corrected Hα emission as a tracer of thermal free–free emission, we found that at 0.33 GHz, the mean thermal fraction is less than 5 percent. Using archival data near 1 GHz, we estimate the mean thermal fraction to be about 10 percent at that frequency. However, in inner regions of the galaxies and/or star forming giant HII regions, the thermal emission could be significantly high at 0.33 GHz, reaching up to 10–15 percent and could be more than 20 percent near 1 GHz. Our study suggests that the radio continuum emission at 0.33 GHz, mostly traces nonthermal emission due to low energy ($\sim$ 1.5 GeV), long lived ($\sim 10^8$ yr) CRes making the 0.33 GHz maps much smoother than those near 1 GHz. The nonthermal emission at 0.33 GHz has significantly larger radial scale lengths than at 1.4 GHz for three of the galaxies, NGC 1097, NGC 5055 and NGC 5236. The increase in the nonthermal emission scale length at 0.33 GHz is larger than those predicted by simple diffusion model, but consistent with streaming instability at the velocity of Alfv́en wave.

We obtained nonthermal spectral index maps at angular resolution of 40 arcsec corresponding to linear scale of 1–3 kpc at the distance of the galaxies. We find that the nonthermal spectral index is generally steeper ($\gtrsim 1$) in regions of low star formation

activity in the interarms and/or located in the outer parts of the galaxy, also the regions of low thermal fraction. In regions of high star formation in the arms and inner parts of the galaxies (regions of high thermal fraction) the nonthermal spectral index is flatter, and has a narrow distribution peaking at ~ 0.8 with a spread of 0.15, putting stringent constraints on the physical conditions for generation, diffusion and energy losses of cosmic ray electrons at scales of ~ 1 kpc. It is interesting that this narrow distribution arises from multiple spatially resolved regions from an assorted set of galaxies with very different star formation histories. This is clearly indicative of a generic process of energy loss of CRe by synchrotron radiation and inverse Compton scattering as they propagate from their acceleration sites. The nonthermal spectral index is seen to flatten ($\alpha_{\rm nt}$ ∼0.4–0.6) with total neutral gas surface mass density above ~ 50 $\rm M_{\odot}pc^{-2}$. In such regions, the CRes most likely lose their energy by bremsstrahlung and/or ionization losses in a typical galactic magnetic field of ~ 10 μG. For regions with surface mass density below 50 $\rm M_{\odot}pc^{-2}$, synchrotron and inverse-Compton losses are dominant and the nonthermal spectral index is seen to steepen sharply ($\alpha_{\rm nt}$ >1). This, however, requires detailed modeling of the CRe energy loss and will be considered in a future work.

We used the nonthermal emission maps to study the radio–FIR correlation between the nonthermal radio continuum emission at 0.33 and 1 GHz, and the far infrared emission due to cool (~ 20 K) dust at $\lambda 70$ μm in spatially resolved normal galaxies at scales of ∼1 kpc. The galaxies studied are NGC 1097, NGC 4254, NGC 4736, NGC 5055, NGC 5236 and NGC 6946. We determined the parameter 'q', used as a measure of tightness of the radio–FIR correlation, within regions of ~ 1 kpc for each of the galaxies. The parameter 'q' was found to be ~ 30 percent higher in the arms than in the interarm regions at 0.33 GHz, while at a higher frequency of 1 GHz, it is only ~ 10 percent higher.

We also computed the slope (b) of the radio–FIR correlation by fitting equation of the form, $S_{\rm radio} = a \times S^{b}_{70\mu m}$, using ordinary least square 'bisector method'. Separate fits were done for arm and interarm regions at both the radio frequencies. The slope of the radio–FIR correlation is found to differ significantly between the arm and interarm regions at 0.33 GHz with $b = 0.6 \pm 0.1$ in arms and $b = 0.33 \pm 0.07$ in the interarms. However, this change is not evident at a higher frequency (∼1 GHz). The slope was found to remain same at 1 GHz, with $b = 0.8 \pm 0.08$ in arms and $b = 0.76 \pm 0.14$ for interarms. The dust heating UV photons, giving rise to FIR emission, has a mean free path of few 100 pc, while the CRe giving rise to the radio emission can propagate to

$\sim$ 1 kpc at 1 GHz and $\sim$ 2 kpc at 0.33 GHz in a typical galactic magnetic field of $\sim$ 10 μG. Thus, in order to have similar slope at different radio frequencies, the energy spectrum of CRe giving rise to the radio emission, must be independent of the volume element. Further, in the arm regions, i.e., regions of high star formation activity, the energy spectrum of the CRe was found to be roughly constant at scales of $\sim$ 1 kpc. This can happen if the timescales of CRe diffusion/propagation is significantly larger than their generation timescales. Under this scenario, if energy equipartition condition is valid, and Kennicutt-Schmidt law index (n) is roughly constant, $n \sim 1.4$, then the slope of the radio–FIR correlation must be independent of the radio frequency and at scales below 1 kpc. This is indeed found to be true for the galaxy NGC 6946 at scales of $\sim$ 0.5 kpc in the arms, where the slope of the radio–FIR correlation was found to be similar within errorbars at 0.33, 1.4 and 5 GHz. This precept requires to be demonstrated on a larger sample of galaxies.

We used the slope of the radio–FIR correlation to estimate the coupling index (κ) between magnetic field (B) and gas density ($\rho_{\rm gas}$), such that $B \propto \rho_{gas}^{\kappa}$. Using our results, at 1.4 GHz, $\kappa = 0.51 \pm 0.1$ in the arms and lies in the range 0.4–0.5 in the interarm regions. However, at 0.33 GHz, we find $\kappa = 0.4 \pm 0.1$ in the arms and $\kappa \sim 0.18 - 0.22$ in the interarms. The estimated values of $\kappa \sim 0.4 - 0.5$ in the arms are in agreement with conditions of equipartition of energy between magnetic field and turbulent motions of gas which is predicted by MHD simulations in turbulent ISM, provided the same region produces both the radio and far infrared emission. At 1 kpc scales, this condition is satisfied for radio emission at 1.4 GHz but may not be satisfied at 0.33 GHz. Owing to different scale lengths of the emission at these two regimes of emission, a change in the form of the radio–FIR correlation is expected. Thus, the change in the slope and values of 'q' between arm and interarm regions at 0.33 GHz is caused due to propagation of old ($\sim 10^8$ yr) CRe from arms to the interarms.

We made maps of total magnetic field using 'equipartition' assumptions for six galaxies, NGC 1097, NGC 4254, NGC 4736, NGC 5055, NGC 5236 and NGC 6946. The magnetic field maps were made at sub-kpc resolutions from nonthermal maps estimated using the Hα corrected λ24 μm technique of separating thermal emission. The mean magnetic field is found to be $\sim$ 11 μG. The field is strongest near the central regions where mean values are $\sim 20 - 25$ μG and falls to $\sim$ 15 μG in disk and $\sim$ 10 μG in the outer parts. There is little variation in the field strength between arm and interarm regions, such that, in the interarms, the field is $\lesssim$20 percent weaker than in the arms. There is no indication of variation in magnetic field as one moves

along arm or interarm after correcting for the radial variation of magnetic field. Our estimated 'equipartition' magnetic field ($B_{\rm eq}$) can well reproduce the dispersion seen in the quantity 'q' of the radio–FIR correlation, that depends on the actual magnetic field, B. This suggests that the estimated $B_{\rm eq}$ (or a constant multiple) is close to the actual field.

The small scale fields, mostly seen in the star forming arm regions, are thought to be amplified by small scale turbulent dynamo and the large scale fields, mostly observed in the interarm and outer parts of the galaxies, are amplified by large scale mean field dynamo action. The fields are amplified by stretching and twisting of the field lines until the Alfv́en velocity is similar to the velocity dispersion of turbulent gas. In this condition, the energy density of magnetic field and kinetic energy density of turbulent gas should be close and thus the radial scale length of magnetic field and gas density must be similar. However, in contradiction to the predictions of dynamo action, the radial scale lengths of the magnetic field is found to significantly higher than that of the gas density in these galaxies.

We therefore compared the energy densities of the various competing forces in the ISM, viz., energy density of magnetic field ($B_{\rm eq}^2/8\pi$), thermal energy density of neutral and ionized gas ($\frac{3}{2}\langle n\rangle kT$) and kinetic energy density of neutral (atomic+molecular) gas ($\frac{1}{2}\rho_{\rm gas}\delta v_{\rm turb}^2$) at sub-kpc scales for five galaxies, namely, NGC 4254, NGC 4736, NGC 5055, NGC 5236 and NGC 6946. The magnetic energy density and the kinetic energy density of turbulent gas is seen to be similar towards the inner parts of the galaxies and in gas-rich arms. The thermal energy density of ionized gas is $\sim 1-2$ orders of magnitude lower than them, while for neutral gas it is $\gtrsim 2$ orders of magnitude lower. The ratio of magnetic field energy and total energy (thermal + turbulent) of gas (neutral + ionized) is seen to be roughly constant along the radius of the galaxies for high signal-to-noise ($> 4\sigma$) regions in gas density, suggesting equillibrium between magnetic energy and turbulent energy. These are the regions with high star formation activity and are dominated by small scale turbulent fields confirmed by polarization observations. The ratio varies within a factor of 2, insinuating the importance of magnetic field in maintaining the energy/pressure balance in the ISM.

Magnetic field energy is seen to dominate over the total energy of gas towards the outer parts of all the galaxies and in the interarm regions, particularly in the highly polarized 'magnetic arms' of NGC 6946. Such a trend in the interarms is seen in other galaxies as well, but with lower significance. The degree of polarization is seen to be higher in the interarms and outer parts of these galaxies as compared to the

arm. In such regions, large scale regular fields dominate which are amplified by mean field dynamo action. For NGC 6946, where ordered fields are observed in the interarm regions, it is thought that finite time dynamo relaxation causes a phase shift between magnetic and gas/star forming spiral arms, such that magnetic arms lag. Magnetic field energy dominating over the turbulent gas energy thus helps maintaining this field orderness in interarm regions and outer parts of the galaxies. The magnetic field strength being more than turbulent gas energy equipartition value suggests that the field is perhaps amplified by magneto-rotational instability that demands further investigation.

Future work

As a part of future work we would like to extend our analysis to a larger sample of galaxies. The sample of galaxies would be chosen from the HERACLES and the SINGS that would ensure the availability of complimentary datasets essential to our studies.

It is important to study the energy balance between the various competing phases of the ISM based on polarization observations. This would allow us to explore the efficiency of the two regimes of magnetic field amplification, i.e., small scale and large scale dynamo action. Further, study of polarized emission based on star formation activity would throw light into the effects of turbulence generation of fields at smaller length scales up to energy equipartition values. We plan to use the archival VLA polarization data on these galaxies to investigate these effects.

To establish the effect of CRe propagation, e.g., simple diffusion, energy dependent diffusion or Alfvénic streaming, on the form of the radio–FIR correlation with high statistical significance more galaxies from the SINGS sample and recent KINGFISH sample observed using the HERSCHEL space telescope needs to be studied. This would require new low frequency observations and we plan to propose using the GMRT a larger sample of nearby normal galaxies. We would like to extend the spatially resolved radio–FIR correlation at sub-kpc linear resolution using the Hα corrected 24 μm method of separating the thermal emission. We also plan to model the dispersion seen in the radio–FIR correlation taking into account the energy loss and escape of CRe and UV photons from the disk of the galaxies that can also change the form of the radio–FIR correlation. From observations at even lower frequencies, e.g. with LOFAR

and MWA, the results of this work could be tested and expanded.

Further study of multifrequency radio–FIR correlation is required to establish the observed constant slope with radio frequency for the galaxy NGC 6946. We intend to extend this work on other galaxies using archival data from the VLA or proposing new observations using the EVLA.

The variation of nonthermal spectral index with gas density needs to be investigated in detail to understand its narrow distribution in the regions of high gas density. This would require additional data from X-ray and gamma-ray observations to study the CRe energy loss mechanisms through inverse-Compton and ionization losses respectively. Polarization observations could reveal the structure of tangled magnetic field in such regions and help us uncover the CRe propagation. These issues will be considered in a future work.

Appendix A

Atomic and Molecular surface gas density

Four of the galaxies (NGC 4736, NGC 5055, NGC 5236 and NGC 6946) studied in this work were observed as a part of THINGS (Walter et al., 2008) to trace HI. We used natural weighted moment-0 HI maps. NGC 4254 was observed as a part of VIVA (Chung et al., 2009). The surface density of atomic gas was computed using the equation,

$$\Sigma_{\rm HI}({\rm M_\odot pc^{-2}}) = 0.02\ \cos i\ I_{\rm HI}({\rm K\ km\ s^{-1}}).$$

Here, i is the inclination angle (0° for face-on) of the galaxy and $I_{\rm HI}$ is the line integrated intensity. The above equation includes a factor 1.36 to account for the presence of Helium.

CO is commonly used as a tracer for molecular gas. We used $\rm CO_{J=2\rightarrow1}$ moment-0 maps from the HERACLES (Leroy et al., 2009) for three of the galaxies, namely NGC 4736, NGC 5055 and NGC 6946. These maps has an angular resolution of 13.4 arcsec, better than the resolution of the nonthermal maps. Assuming a constant CO-to-H_2 conversion factor, $X_{\rm CO} = 2 \times 10^{20} {\rm cm^{-2}(K\ km\ s^{-1})^{-1}}$ and a line ratio of 0.8 for converting $\rm CO_{J=2\rightarrow1}$ flux to $\rm CO_{J=1\rightarrow0}$ flux, the molecular gas surface density was calculated using,

$$\Sigma_{\rm H_2}({\rm M_\odot pc^{-2}}) = 5.5\ \cos i\ I_{\rm CO_{J=2\rightarrow1}}({\rm K\ km\ s^{-1}}).$$

Here, $I_{\rm CO_{J=2\rightarrow1}}$ is the line integrated intensity. Note that, for NGC 6946, the cos i factor was missing in Beck (2007) by mistake (Rainer Beck, private communication). However, this would not change their conclusions significantly.

For the galaxy NGC 5236 we used $\rm CO_{J=1\rightarrow0}$ moment-0 map from the NRAO 12-m

telescope (Crosthwaite et al., 2002) to calculate the molecular gas density. This map has an angular resolution of 55 arcsec corresponding to a spatial scale of ~ 1.2 kpc. The line integrated flux density ($S_{\mathrm{CO_{J=1\rightarrow 0}}}$) was converted into molecular gas mass ($M_{\mathrm{H_2}}$) using the formula

$$M_{\mathrm{H_2}}(M_\odot) = 1.1 \times 10^4 D(\mathrm{Mpc})^2 \cos i \; S_{\mathrm{CO_{J=1\rightarrow 0}}}(\mathrm{Jy\ km\ s^{-1}})$$

from Young et al. (1989). Here, D is the distance to the galaxy. The mass was then converted to surface density by diving by the linear area for each pixel.

Bibliography

Adebahr B., Krause M., Klein U., Wezgowiec M., Bomans D. J., Dettmar R.-J., 2012, ArXiv e-prints [4, 5, 72, 104]

Alton P. B., Xilouris E. M., Misiriotis A., Dasyra K. M., Dumke M., 2004, A&A, 425, 109 [102, 118]

Appleton P. N. et al., 2004, ApJS, 154, 147 [21, 88]

Arp H., 1973, ApJ, 183, 791 [42]

Baars J. W. M., Genzel R., Pauliny-Toth I. I. K., Witzel A., 1977, A&A, 61, 99 [40]

Balsara D. S., Kim J., 2005, ApJ, 634, 390 [2]

Barth A. J., Strigari L. E., Bentz M. C., Greene J. E., Ho L. C., 2009, ApJ, 690, 1031 [35]

Basu A., Mitra D., Wadadekar Y., Ishwara-Chandra C. H., 2012, MNRAS, 419, 1136 [ii, iii, iv, vii, 88, 98, 104, 105, 107, 109, 112, 116, 118, 120, 121]

Basu A., Roy S., 2013, MNRAS, 433, 1675 [iii]

Basu A., Roy S., Mitra D., 2012, ApJ, 756, 141 [ii, iii, 116, 118]

Batchelor G. K., 1950, Royal Society of London Proceedings Series A, 201, 405 [103]

Beck R., 1991, A&A, 251, 15 [48]

Beck R., 2005, in Lecture Notes in Physics, Berlin Springer Verlag, Vol. 664, Cosmic Magnetic Fields, Wielebinski R., Beck R., eds., p. 41 [6]

Beck R., 2006, Astronomische Nachrichten, 327, 512 [103]

BIBLIOGRAPHY

Beck R., 2007, A&A, 470, 539 [xi, 3, 4, 6, 7, 33, 37, 44, 48, 67, 77, 113, 116, 117, 121, 124, 125, 133]

Beck R., Brandenburg A., Moss D., Shukurov A., Sokoloff D., 1996, ARAA, 34, 155 [5, 109, 125]

Beck R., Ehle M., Shoutenkov V., Shukurov A., Sokoloff D., 1999, Nature, 397, 324 [6, 112]

Beck R., Fletcher A., Shukurov A., Snodin A., Sokoloff D. D., Ehle M., Moss D., Shoutenkov V., 2005, A&A, 444, 739 [5, 6, 35, 52, 70, 71, 105, 106, 112]

Beck R., Golla G., 1988, A&A, 191, L9 [22, 83]

Beck R., Graeve R., 1982, A&A, 105, 192 [52]

Beck R., Hoernes P., 1996, Nature, 379, 47 [6]

Beck R., Krause M., 2005, Astronomische Nachrichten, 326, 414 [iii, iv, vii, 15, 16, 17, 18, 105, 111]

Beck R., Shoutenkov V., Ehle M., Harnett J. I., Haynes R. F., Shukurov A., Sokoloff D. D., Thierbach M., 2002, A&A, 391, 83 [42]

Bell A. R., 1978, MNRAS, 182, 443 [11, 15, 52, 79]

Berkhuijsen E. M., Beck R., Hoernes P., 2003, A&A, 398, 937 [52]

Berkhuijsen E. M., et al., 1997, in The Physics of Galactic Halos, Lesch H., Dettmar R.-J., Mebold U., Schlickeiser R., eds., p. 155 [84]

Berkhuijsen E. M., Mitra D., Mueller P., 2006, Astronomische Nachrichten, 327, 82 [55]

Bhat P., Subramanian K., 2013, MNRAS, 429, 2469 [2]

Biermann P. L., Becker Tjus J., Seo E.-S., Mandelartz M., 2013, ApJ, 768, 124 [2]

Biermann P. L., Strom R. G., 1993, A&A, 275, 659 [11, 52]

Bogdan T. J., Völk H. J., 1983, A&A, 122, 129 [11, 52]

Brandenburg A., 2009, ApJ, 697, 1206 [2]

Brandenburg A., Dobler W., 2001, A&A, 369, 329 [2]

Brandenburg A., Sokoloff D., Subramanian K., 2012, SSRv, 169, 123 [2]

Braun R., Oosterloo T. A., Morganti R., Klein U., Beck R., 2007, A&A, 461, 455 [31, 32, 35, 36, 42, 47]

Bregman J. N., 1980, ApJ, 236, 577 [4, 104]

Briggs E. L., 1995, PhD thesis, NORTH CAROLINA STATE UNIVERSITY. [43]

Broadbent A., Osborne J. L., Haslam C. G. T., 1989, MNRAS, 237, 381 [62]

Brown R. H., Hazard C., 1961, MNRAS, 122, 479 [42]

Buczilowski U. R., Beck R., 1991, A&A, 241, 47 [6]

Burbidge G. R., 1956, ApJ, 124, 416 [13]

Buta R. J., Corwin H. G., Odewahn S. C., 2007, The de Vaucouleurs atlas of galaxies, Cambridge Univ. Press [35]

Calzetti D., Conselice C. J., Gallagher, III J. S., Kinney A. L., 1999, AJ, 118, 797 [113]

Calzetti D. et al., 2005, ApJ, 633, 871 [11, 59]

Carilli C. L., Holdaway M. A., Ho P. T. P., de Pree C. G., 1992, ApJL, 399, L59 [52]

Caswell J. L., Wills D., 1967, MNRAS, 135, 231 [42]

Chamandy L., Subramanian K., Shukurov A., 2013, MNRAS, 428, 3569 [2, 7, 125]

Chandrasekhar S., Fermi E., 1953, ApJ, 118, 113 [v, 2, 84]

Cho J., Lazarian A., Vishniac E. T., 2003, in Lecture Notes in Physics, Berlin Springer Verlag, Vol. 614, Turbulence and Magnetic Fields in Astrophysics, Falgarone E., Passot T., eds., pp. 56–98 [v, 2, 84]

Cho J., Vishniac E. T., 2000, ApJ, 539, 273 [v, 2, 3, 84, 120, 124]

Chung A., van Gorkom J. H., Kenney J. D. P., Crowl H., Vollmer B., 2009, AJ, 138, 1741 [32, 133]

Chyży K. T., 2008, A&A, 482, 755 [4, 112]

BIBLIOGRAPHY

Chyży K. T., Beck R., 2004, A&A, 417, 541 [5]

Chyży K. T., Buta R. J., 2008, ApJL, 677, L17 [6, 74, 112, 113, 125]

Chyży K. T., Ehle M., Beck R., 2007, A&A, 474, 415 [42, 73, 112]

Combes F., Becquaert J.-F., 1997, A&A, 326, 554 [121]

Condon J. J., 1987, ApJS, 65, 485 [46]

Condon J. J., 1992, ARAA, 30, 575 [xi, 11, 20, 21, 49, 51, 83]

Condon J. J., Anderson M. L., Helou G., 1991, ApJ, 376, 95 [22]

Condon J. J., Cotton W. D., Greisen E. W., Yin Q. F., Perley R. A., Taylor G. B., Broderick J. J., 1998, AJ, 115, 1693 [31]

Cornwell T. J., Perley R. A., 1992, A&A, 261, 353 [42]

Cox M. J., Eales S. A. E., Alexander P., Fitt A. J., 1988, MNRAS, 235, 1227 [21, 84]

Crosthwaite L. P., Turner J. L., Buchholz L., Ho P. T. P., Martin R. N., 2002, AJ, 123, 1892 [33, 105, 134]

Crutcher R. M., 1999, ApJ, 520, 706 [vii, 84, 103, 120]

Davis, Jr. L., Greenstein J. L., 1951, ApJ, 114, 206 [8]

de Bruyn A. G., 1977, A&A, 54, 491 [36, 42, 73]

de Jong M. L., 1966, ApJ, 144, 553 [42]

de Jong M. L., 1967, ApJ, 150, 1 [42]

de Vaucouleurs G., de Vaucouleurs A., Corwin, Jr. H. G., Buta R. J., Paturel G., Fouqué P., 1991, Third Reference Catalogue of Bright Galaxies. Volume I: Explanations and references. Volume II: Data for galaxies between 0^h and 12^h. Volume III: Data for galaxies between 12^h and 24^h. [32]

Devereux N. A., Eales S. A., 1989, ApJ, 340, 708 [98]

Dickinson C., Davies R. D., Davis R. J., 2003, MNRAS, 341, 369 [55]

Draine B. T., Lee H. M., 1984, ApJ, 285, 89 [55, 102, 118]

Dressel L. L., 1988, ApJL, 329, L69 [21, 83]

Dumas G., Schinnerer E., Tabatabaei F. S., Beck R., Velusamy T., Murphy E., 2011, AJ, 141, 41 [22, 26, 83, 84, 98]

Duric N., Bourneuf E., Gregory P. C., 1988, AJ, 96, 81 [53]

Duric N., Dittmar M. R., 1988, ApJL, 332, L67 [36]

Elmegreen B. G., 1981, ApJ, 243, 512 [vii, 103]

Fiedler R. A., Mouschovias T. C., 1993, ApJ, 415, 680 [2, 99, 118]

Fitt A. J., Alexander P., Cox M. J., 1988, MNRAS, 233, 907 [22]

Fletcher A., Beck R., Shukurov A., Berkhuijsen E. M., Horellou C., 2011, MNRAS, 412, 2396 [4, 5, 6, 7, 104, 124]

Frick P., Beck R., Berkhuijsen E. M., Patrickeyev I., 2001, MNRAS, 327, 1145 [22]

Gioia I. M., Gregorini L., 1980, A&AS, 41, 329 [42]

Gioia I. M., Gregorini L., Klein U., 1982, A&A, 116, 164 [62]

Green D. A., 2009, Bulletin of the Astronomical Society of India, 37, 45 [11, 79]

Groves B. A., Cho J., Dopita M., Lazarian A., 2003, PASA, 20, 252 [v, 2, 84, 99, 103, 118, 120, 124]

Han J. L., Beck R., Ehle M., Haynes R. F., Wielebinski R., 1999, A&A, 348, 405 [6]

Harwit M., Pacini F., 1975, ApJL, 200, L127 [v, 23, 83]

Heald G. H., 2012, ApJL, 754, L35 [4, 104]

Heesen V., Beck R., Krause M., Dettmar R.-J., 2009, A&A, 494, 563 [4, 48, 104]

Helou G., Bicay M. D., 1993, ApJ, 415, 93 [iv, v, 23, 25, 83]

Helou G., Khan I. R., Malek L., Boehmer L., 1988, ApJS, 68, 151 [21]

Helou G., Soifer B. T., Rowan-Robinson M., 1985, ApJL, 298, L7 [11, 21, 85]

Hoang T., Lazarian A., 2008, MNRAS, 388, 117 [8]

Hoernes P., Berkhuijsen E. M., Xu C., 1998, A&A, 334, 57 [22, 83, 84, 88, 98]

Hoopes C. G., Walterbos R. A. M., Rand R. J., 1999, ApJ, 522, 669 [121]

Hughes A., Wong T., Ekers R., Staveley-Smith L., Filipovic M., Maddison S., Fukui Y., Mizuno N., 2006, MNRAS, 370, 363 [22, 83, 98]

Hummel E., 1980, A&AS, 41, 151 [42]

Hummel E., 1986, A&A, 160, L4 [118]

Hummel E., Bosma A., 1982, AJ, 87, 242 [36, 42, 62, 74, 75]

Isobe T., Feigelson E. D., Akritas M. G., Babu G. J., 1990, ApJ, 364, 104 [93]

Israel F. P., van der Hulst J. M., 1983, AJ, 88, 1736 [42]

Kantharia N. G., Rao A. P., Sirothia S. K., 2008, MNRAS, 383, 173 [36, 42, 73]

Karachentsev I. D. et al., 2002, A&A, 385, 21 [33]

Karachentsev I. D. et al., 2003, A&A, 398, 467 [32]

Karachentsev I. D., Sharina M. E., Huchtmeier W. K., 2000, A&A, 362, 544 [33]

Kardashev N. S., 1962, SvA, 6, 317 [101]

Kasparova A. V., Zasov A. V., 2008, Astronomy Letters, 34, 152 [121]

Kellermann K. I., Pauliny-Toth I. I. K., Williams P. J. S., 1969, ApJ, 157, 1 [42]

Kennicutt, Jr. R. C., 1998, ARAA, 36, 189 [26, 99]

Kennicutt, Jr. R. C. et al., 2003, PASP, 115, 928 [vi, 29, 32, 54, 85]

Kim J., Balsara D., Mac Low M.-M., 2001, Journal of Korean Astronomical Society, 34, 333 [2, 99]

Klein U., Beck R., Buczilowski U. R., Wielebinski R., 1982, A&A, 108, 176 [37, 52, 77]

Klein U., Emerson D. T., 1981, A&A, 94, 29 [37, 42]

Klein U., Gräve R., Wielebinski R., 1983, A&A, 117, 332 [52]

Klein U., Wielebinski R., Morsi H. W., 1988, A&A, 190, 41 [42, 72]

Knapen J. H., Stedman S., Bramich D. M., Folkes S. L., Bradley T. R., 2004, A&A, 426, 1135 [32, 54, 74, 86]

Knapik J., Soida M., Dettmar R.-J., Beck R., Urbanik M., 2000, A&A, 362, 910 [6, 7, 36, 75, 113]

Kothes R., Fedotov K., Foster T. J., Uyanıker B., 2006, A&A, 457, 1081 [11, 79]

Krause M., Beck R., Hummel E., 1989, A&A, 217, 17 [6]

Krause M., Hummel E., Beck R., 1989, A&A, 217, 4 [6]

Krügel E., 2003, The physics of interstellar dust [55]

Kuril'chik V. N., Andrievskii A. E., Ivanov V. N., Spangenberg E. E., 1970, SvA, 13, 881 [42]

Kuril'Chik V. N., Onishchenko L. V., Turevskil V. M., 1967, SvA, 11, 528 [42]

Lacki B. C., Beck R., 2013, MNRAS, 430, 3171 [106]

Leroy A. K. et al., 2009, AJ, 137, 4670 [32, 102, 105, 133]

Leroy A. K., Walter F., Brinks E., Bigiel F., de Blok W. J. G., Madore B., Thornley M. D., 2008, AJ, 136, 2782 [103]

Lisenfeld U., Völk H. J., Xu C., 1996, A&A, 306, 677 [24]

Longair M. S., 2011, High energy astrophysics, 3rd ed. Cambridge: Cambridge University Press [11, 17, 79, 80, 105, 106]

Machida M., Nakamura K. E., Kudoh T., Akahori T., Sofue Y., Matsumoto R., 2013, ApJ, 764, 81 [2]

Maddox L. A., Cowan J. J., Kilgard R. E., Lacey C. K., Prestwich A. H., Stockdale C. J., Wolfing E., 2006, AJ, 132, 310 [75]

Mayya Y. D., Carrasco L., Luna A., 2005, ApJL, 628, L33 [35]

Miley G., 1980, ARAA, 18, 165 [iv, 15, 18, 105]

Moffatt H. K., 1978, Magnetic field generation in electrically conducting fluids [103]

Moffet A. T., 1975, Strong Nonthermal Radio Emission from Galaxies, Sandage A., Sandage M., Kristian J., eds., the University of Chicago Press, p. 211 [96]

Moss D., Shukurov A., 1996, MNRAS, 279, 229 [2, 103]

Murgia M., Helfer T. T., Ekers R., Blitz L., Moscadelli L., Wong T., Paladino R., 2005, A&A, 437, 389 [3, 11, 22, 24, 52, 83, 96]

Murphy E. J. et al., 2006, ApJ, 638, 157 [vi, 21, 58, 59, 83, 88, 92]

Murphy E. J. et al., 2010, ApJL, 709, L108 [37]

Murphy E. J., Helou G., Kenney J. D. P., Armus L., Braun R., 2008, ApJ, 678, 828 [vi, 58, 60]

Nagar N. M., Falcke H., Wilson A. S., 2005, A&A, 435, 521 [42]

Neininger N., 1992, A&A, 263, 30 [6]

Neininger N., Beck R., Sukumar S., Allen R. J., 1993, A&A, 274, 687 [6, 113, 125]

Neininger N., Klein U., Beck R., Wielebinski R., 1991, Nature, 352, 781 [6, 113]

Niklas S., 1995, PhD thesis, PhD Thesis, Univ. Bonn, (1995) [5]

Niklas S., Beck R., 1997, A&A, 320, 54 [iv, v, 2, 23, 25, 26, 83, 84]

Niklas S., Klein U., Wielebinski R., 1997, A&A, 322, 19 [24, 52, 53, 80]

Norman C. A., Ikeuchi S., 1989, ApJ, 345, 372 [104]

Ondrechen M. P., 1985, AJ, 90, 1474 [37, 75]

Ondrechen M. P., van der Hulst J. M., 1983, ApJL, 269, L47 [35, 70, 71]

Ondrechen M. P., van der Hulst J. M., Hummel E., 1989, ApJ, 342, 39 [70]

Osterbrock D. E., 1989, Astrophysics of gaseous nebulae and active galactic nuclei [59]

Pacholczyk A. G., 1970, Radio astrophysics. Nonthermal processes in galactic and extragalactic sources [105]

Paladino R., Murgia M., Helfer T. T., Wong T., Ekers R., Blitz L., Gregorini L., Moscadelli L., 2006, A&A, 456, 847 [22, 83, 96, 98]

Paladino R., Murgia M., Orrú E., 2009, A&A, 503, 747 [22, 35, 37, 48, 52, 81, 83, 101]

Parker E. N., 1966, ApJ, 145, 811 [2]

Parker E. N., 1979, Cosmical magnetic fields: Their origin and their activity [103]

Pérez-González P. G. et al., 2006, ApJ, 648, 987 [59]

Phookun B., Vogel S. N., Mundy L. G., 1993, ApJ, 418, 113 [36]

Price R., Duric N., 1992, ApJ, 401, 81 [21, 22, 83, 98]

Rees M., 2005, in Lecture Notes in Physics, Berlin Springer Verlag, Vol. 664, Cosmic Magnetic Fields, Wielebinski R., Beck R., eds., p. 1 [2]

Rengarajan T. N., Iyengar K. V. K., 1990, MNRAS, 242, 74 [22]

Rieke G. H. et al., 2004, ApJS, 154, 25 [85]

Roy S., Rao A. P., 2004, MNRAS, 349, L25 [44]

Rubin R. H., 1968, ApJ, 154, 391 [59]

Rüdiger G., Hollerbach R., 2004, The Magnetic Universe, Wiley Interscience [3, 117, 125]

Schommer R. A., Sullivan, III W. T., 1976, Ap. Lett., 17, 191 [36]

Schöneberg S., Becker Tjus J., Schuppan F., 2012, ArXiv e-prints [11]

Seaquist E. R., Odegard N., 1991, ApJ, 369, 320 [35, 72]

Segalovitz A., 1977a, A&A, 54, 703 [52]

Segalovitz A., 1977b, A&A, 61, 59 [52]

Sellwood J. A., Balbus S. A., 1999, ApJ, 511, 660 [3, 117, 121, 125]

Shapiro P. R., Field G. B., 1976, ApJ, 205, 762 [104]

Shukurov A., Sokoloff D., Subramanian K., Brandenburg A., 2006, A&A, 448, L33 [103]

Smith B. J., Lester D. F., Harvey P. M., Pogge R. W., 1991, ApJ, 380, 677 [74]

Soida M., Beck R., Urbanik M., Braine J., 2002, A&A, 394, 47 [6]

Soida M., Urbanik M., Beck R., 1996, A&A, 312, 409 [42]

Sokoloff D. D., Bykov A. A., Shukurov A., Berkhuijsen E. M., Beck R., Poezd A. D., 1998, MNRAS, 299, 189 [9, 104]

Steer D. G., Dewdney P. E., Ito M. R., 1984, A&A, 137, 159 [43]

Subramanian K., 2008, ArXiv e-prints: 0802.2804 [2]

Sukumar S., Allen R. J., 1989, Nature, 340, 537 [113]

Sukumar S., Klein U., Graeve R., 1987, A&A, 184, 71 [37, 42, 48, 75]

Swarup G. J., Ananthakrishnan S. A., Kapahi V. K., Rao A. P., Subrahmanya C. R., Kulkarni V. K., 1991, Current Science, 60, 95 [37]

Tabatabaei F. S. et al., 2007a, A&A, 466, 509 [22, 83]

Tabatabaei F. S., Beck R., Krügel E., Krause M., Berkhuijsen E. M., Gordon K. D., Menten K. M., 2007b, A&A, 475, 133 [v, 4, 53, 54, 55, 58, 62, 66, 85, 88, 116, 118]

Tabatabaei F. S., Krause M., Fletcher A., Beck R., 2008, A&A, 490, 1005 [3, 6]

Tabatabaei F. S. et al., 2013, A&A, 552, A19 [22]

Thompson T. A., Quataert E., Waxman E., Murray N., Martin C. L., 2006, ApJ, 645, 186 [v, 3, 83, 99]

Valls-Gabaud D., 1998, PASA, 15, 111 [53, 121]

van der Kruit P. C., 1971, A&A, 15, 110 [20, 21, 83]

van der Kruit P. C., 1973, A&A, 29, 263 [20, 21, 83]

van der Kruit P. C., Allen R. J., Rots A. H., 1977, A&A, 55, 421 [37, 42, 52, 77]

Völk H. J., 1989, A&A, 218, 67 [iv, 23, 24]

Vollmer B., Huchtmeier W., van Driel W., 2005, A&A, 439, 921 [36]

Walsh W., Beck R., Thuma G., Weiss A., Wielebinski R., Dumke M., 2002, A&A, 388, 7 [3, 117, 125]

Walter F., Brinks E., de Blok W. J. G., Bigiel F., Kennicutt, Jr. R. C., Thornley M. D., Leroy A., 2008, AJ, 136, 2563 [32, 105, 133]

Wang C.-Y., Lo Y.-Y., Ko C.-M., 2010, ArXiv e-prints [2]

Wang J., Heckman T. M., Lehnert M. D., 1997, ApJ, 491, 114 [121]

Wright A. E., Wark R. M., Troup E., Otrupcek R., Hunt A., Cooke D. J., 1990, Proceedings of the Astronomical Society of Australia, 8, 261 [42]

Wunderlich E., Wielebinski R., Klein U., 1987, A&AS, 69, 487 [21, 22, 83]

Xu C., 1990, ApJL, 365, L47 [98]

Xu C., Helou G., 1996, ApJ, 456, 163 [27, 98]

Xu C., Klein U., Meinert D., Wielebinski R., Haynes R. F., 1992, A&A, 257, 47 [22, 83, 88]

Young J. S., Xie S., Kenney J. D. P., Rice W. L., 1989, ApJS, 70, 699 [134]

Yun M. S., Reddy N. A., Condon J. J., 2001, ApJ, 554, 803 [11, 21, 83, 98]

Zweibel E. G., Heiles C., 1997, Nature, 385, 131 [104]